EPFL

Thèse n° 7179

Accelerating materials discovery for solid state electrolytes

Présentée le 19 octobre 2020

à la Faculté des sciences et techniques de l'ingénieur
Laboratoire de théorie et simulation des matériaux
Programme doctoral en science et génie des matériaux

pour l'obtention du grade de Docteur ès Sciences

par

Matthieu Gilles MOTTET

Acceptée sur proposition du jury

Prof. J. Brugger, président du jury
Prof. N. Marzari, Dr I. Tavernelli, directeurs de thèse
Prof. J. Hutter, rapporteur
Dr D. Passerone, rapporteur
Prof. M. Ceriotti, rapporteur

École
polytechnique
fédérale
de Lausanne

2020

Ever tried. Ever failed. No matter.
Try again. Fail again. Fail better.
— Samuel Beckett - *Worstward Ho* (1983)

Acknowledgements

I would like to thank the many people that have accompanied and help me during the long journey that was this thesis.

Firstly, I would like to thank IBM Research and the Foundations of Cognitive Computing group for the opportunity to work in an inspiring environment surrounded by brilliant people. Particular thanks go to Ivano Tavernelli for the supervision, trust and guidance, Kostas Bekas and Teodoro Laino for the support and patience, Aris Marcolongo and Tobias Binninger for the help and discussions and to all the colleagues that made this journey more enjoyable.

I would like to express my gratitude to Nicola Marzari, for welcoming me in his group and supporting me along the way, and to the NCCR MARVEL for the funding and manny opportunities to meet a diverse and interesting community of scientists, and in particular all the members of the Solid-State Ionics incubator project.

There are too many more people to thanks but the list would not be complete without Shiksha, who always believed in me and kept me sane when I felt all was lost, my parents Pascale and François and my family for their indefectible support.

Zurich, 28 August 2018 M. M.

Abstract

The development of new solid-state electrolytes is a key step in improving the performance and safety of battery technology. Although the use of first-principle methods has proved invaluable in better understanding the process at play in these materials, these methods remains extremely costly and limit the ability to model the diffusion phenomena as this one is often happening over large time-scales. To solve this issue and unlock larger time-scale and supercells, the use of force-fields has proven to be an effective solution. In particular, polarizable force-fields have been shown to be effective at reproducing accurate diffusion results. To this effect, a methodology is proposed here for the training of such polarizable force-fields using a Self-Adaptive Differential Evolution algorithm. The constant optimization of the shell positions is avoided by using its optimal position with respect to the error on cores. Furthermore, the generation of synthetic training sets is proposed through the use of Monte-Carlo dynamics and random thermal displacements. The potential of force-field modeling is then demonstrated by investigating the effect of tungsten doping on garnet type electrolytes. This investigation shows the importance of averaging over dopant distributions and highlights the complex interplay between the various effects resulting of the insertion of doping species. These various effects are isolated through the use of two distinct doping models, an implicit model where the extra positive charge is introduced as a background charge and an explicit one where the dopant is explicitly introduced. Finally the computation of the electrochemical stability of solid-state electrolytes is introduced. The different methods used to compute it are discussed and their results for relevant Li- and Na-based solid-state electrolytes are compared.

Résumé

Le développement de nouveau électrolytes solides est une étape clé pour l'amélioration des performances et de la sûreté des batteries. Bien que l'utilisation de méthodes *ab initio* s'est révélée inestimable afin de mieux comprendre les processus actifs dans ces matériaux, ces méthodes demeurent extrêmement couteuses et limitent la possibilité de modéliser les phénomènes de diffusion car ils se produisent souvent sur de grandes échelles de temps. Pour résoudre ce problème et donner accès à de plus grandes échelles de temps et de plus grand systèmes, l'utilisation de champ de forces s'est avérée être une solution efficace. En particulier, les champs de forces polarisables se sont révélés efficaces pour reproduire avec précision des résultats pour la diffusion. À cet effet, une méthodologie est proposée pour la paramétrisation de tel champs de force polarisables à l'aide d'un algorithme d'évolution différentielle auto-adaptif. La constante optimisation de la position des coques électroniques est évitée en utilisant une position optimale pour la minimisation de l'erreur sur les noyaux. En outre, l'utilisation de set de référence synthétique est proposée. Ces sets sont générés à l'aide de la méthode de Monte-Carlo et de l'utilisation de déplacement thermiques aléatoires. Le potentiel de la modélisation à l'aide de champ de force est ensuite démontré en explorant les effets du dopage au tungstène sur les électrolytes de type grenat. Cette étude démontre l'importance de faire une moyenne sur les distributions de dopants et souligne l'interaction complexe entre les divers effets résultant de l'insertion d'espèces dopantes. Ces différents effets sont isolés en utilisant deux modèles de dopage distincts, un modèle implicite dans lequel la charge positive supplémentaire est introduite en tant que charge de fond et un modèle explicite où le dopant est explicitement introduit. Finalement le calcul de la stabilité électrochimique des électrolytes solides est introduit. Les différentes méthodes utilisées pour son calculer sont discutées et leurs résultats pour différent électrolytes solides pertinents sont comparés.

Contents

Acknowledgements v

Abstract vii

List of Figures xiii

List of Tables xix

1 Introduction 1

2 Methods 13

3 Lithium dynamics in LLZO 29

4 Molecular Dynamics based Force-Field Parametrization 47

5 Synthetic Training Set based Force-Field Parametrization 63

6 Comparison of computational methods for the electrochemical stability window of solid-state electrolyte materials 83

7 Conclusion 105

A Supporting Information 109

Bibliography 117

List of Figures

1.1 Worldwide Lithium-ion sales for electronics, industrial and automotive applications, and others (namely power tools, e-bikes, medical devices, etc) from 2000 to 2016. [1] 1

1.2 Crystal structure of $NaZr_2(PO_4)_3$, the base structure of NaSICON-type electrolytes with the P centers represented as purple tetrahedra and the Zr ones as green octahedra. Figure generated using the VESTA software [2]. 3

1.3 Crystal structure of γ-Li_3PO_4, the base structure of LiSICON-type electrolytes with the P centers represented as purple tetrahedra. Figure generated using the VESTA software [2]. 4

1.4 Crystal structure of Li_7LaO_6. Figure generated using the VESTA software [2]. . . 5

1.5 Crystal structure of $Li_5La_3Ta_2O_{12}$. The La centers are represented in blue and the Ta ones in brown. Li sites are represented in green. Figure generated using the VESTA software [2]. 6

1.6 Crystal environment of the lithium in the garnet structure. The most stable site is the Li1, $24d$, tetrahedral site. In stuffed garnets, two degenerate Li2, $96h$, distorted octahedral sites are then occupied. The two degenerate sites are situated next to the *ideal* $48g$ octahedral Li3 site. Figure generated using the VESTA software [2]. 7

1.7 Representation of the two mechanisms proposed by Xu *et al.*. The octahedral sites and the tetrahedral one are respectively represented in red and blue [3]. . 8

2.1 Schematic representation of the core-shell model. The shell is trapped in a harmonic potential centered on the core of the atom. 24

3.1 Comparison between the DFT and force-field forces on Li, La, Zr, and O evaluated for the initial training set used for the parametrization of the force-field. . 31

3.2 Comparison between the reference DFT and force-field energies as a function of the strain applied to the system. 31

3.3 **Left** Comparison between the NVE and NVT convergence of the charge and tracer diffusion coefficient of the Li ion with respect to the time lag in the LLWZO system with $x = 0.15$. **Right** The resulting Arhenius plots corresponding to the t^{-1} fits of the diffusion coefficient show little to no effect on the activation energy by only slightly shifting the curve up or down. 32

3.4 Radial distributions of the Zr-Zr (red) and W-W (blue) pairs respectively in the undoped and Boltzmann-distributed doped structures with doping fraction $x = 0.15$ (top) and 0.25 (bottom). The shortest distance pairs are absent at low doping concentration structure due to the increased Coulomb repulsion between the hypervalent cations. Increasing the concentration saturates the structure enough that the shortest distances are forced to be occupied but longer distances remain favoured compared to the original *bcc* Zr structure. The green curve represents the integral of the W-W radial distribution function. 34

3.5 XRD pattern of the $Li_{6.7}La_3Zr_{1.85}W_{0.15}O_{12}$ computed from the 300 K trajectories averaged over the dopant distribution. The pattern replicates the use of Cu $K\alpha$ radiation with 2θ in the range of 10 – 80°. For comparison the position and amplitude of the peaks reported by Li *et al.* [96] for the same structure are displayed. 35

3.6 Lattice parameters as a function of the temperature for an undoped structure (**green** and **purple**) and doped (**blue** implicit and **red** explicit) with a doping fraction $x = 0.15$. The **brown circles** are experimental values reported by Larraz *et al.* [69]. The **brown squares** are the same experimental values shifted as to align the cubic lattice parameters. The phase transition can be observed between 800 and 900 K for the undoped structure with a small hysteresis. Both doped models succesfully stabilize the cubic structure at low temperature. 36

3.7 **a)** Radial distribution function of the Li-M pairs, M = W (**solid**) and Zr (**dotted**) for $x = 0.150$ at temperatures between 300 and 500 K. The vertical lines indicate the distances to the neighboring octahedreal, $96h$, (**dash-dotted**) and tetrahedral, $24d$, (**solid**) crystallographic sites. **b** Integral of the radial distribution functions presented in *a*. 37

3.8 Representation of the lithium distribution sampled during 8 ns of simulations around a central Zr (**left**) and W (**right**) ion. The lithiums are displayed in red when within a 3.75Å distance of the central atom and blue otherwise. The sites of the crystallographic structures are overlaid in orange. The figure illustrates the depletion in lithium density around the tetrahedral sites already observed in Fig. 3.7 ($r = 3.6$Å). 38

3.9 Relative error of $D_{\sigma,n}$, the estimator of the charge diffusion coefficient using a subset of n structures of formula $Li_{6.5}La_3Zr_{1.75}W_{0.25}O_{12}$, with respect to $D_{\sigma,50}$, used as an estimate of $D_{\sigma,\infty}$ at 300, 400 and 500 K. 39

3.10 Log-log plot of the configurational noise, $\sigma^{\mathrm{DOP}}_{t_{\mathrm{lag}}}(T)$, and of the sampling noises estimations, $\sigma^{\mathrm{SAMP}}_{t_{\mathrm{lag}}}(T)$ as a function of the simulation time T and for a lag time, t_{lag}, of 22.5 ps. A linear decay of the sampling noise can be observed, compatible with the theoretical $T^{-1/2}$ behavior. The stabilization of the estimator of the configurational noise at a much higher value shows that the simulations time T is large enough to guarantee $\sigma^{\mathrm{SAMP}}_{t_{\mathrm{lag}}}(T) \ll \sigma^{\mathrm{DOP}}_{t_{\mathrm{lag}}}$. 40

3.11 Tracer (**solid**) and charge (**dashed**) diffusion coefficients for doping concentrations $x = 0.15$ (**left**) and $x = 0.25$ (**right**). Simulations considering explicit and implicit doping are reported and compared with ones of the cubic undoped structure. Activation energies are reported in the text. 41

3.12 Global and site-type resolved autocorrelation functions of the site occupancy σ_i at 300 K, 400 K and 500 K for the undoped (**blue**), $x = 0.15$ (**orange**) and $x = 0.25$ (**green**) explicit doping, and $x = 0.15$ (**red**) implicit doping. 44

4.1 With small variations of the A parameter, the repulsive barrier of the O – O Buckingham pair used in Chap. 4 vanishes and result in a purely attractive potential. The barrier ΔU is shown for the initial parameters. 55

4.2 Atomic forces on an oxygen atom (**top**) as a function of the parameters A, ρ and C of the Li-, Ta- and O-O pairs. (**bottom**) Graphs of the numerical and analytic derivatives of the three components of the forces with respect to each of the parameters of the pair. The numerical derivatives are characterized by an important noise, in particular visible on the middle panel. 57

4.3 Normalized value of $\mathcal{C}_F$ as a function of the parameters A, ρ and C of the Li-, Ta- and O-O pairs. The bottom figures show the numerical and analytic derivative of the upper functions. The numerical are characterized by a consequent noise carried over from the derivative of the forces. 57

4.4 Progress of the SADE population throughout the optimization 58

4.5 Correlation of the reference DFT forces with the one computed using the trained force field. The latter ones are computed with the shells at positions minimizing the error on the oxygen, with a tolerance of 1 eVÅ^{-1}. For all core species, a good agreement is shown between the reference and fitted forces. The error on the forces of the shells are the only one staying relatively high. 59

4.6 Correlation of the reference DFT forces with the one computed using the trained force field. The latter ones are computed with the shells having been relaxed from their initial positions. The quality of the correlation remains high despite a tendency to underestimate the forces on the oxygen cores. The error on the forces of the shells is greatly reduced to the level of accuracy of the other forces. 59

4.7 Correlation of the reference DFT forces with the one computed using the locally optimized force field starting from the result of the global optimization. The latter ones are computed with the shells at positions minimizing the error on the oxygen, with a tolerance of 1 eVÅ^{-1}. No noticeable improvement can be seen compared to the results of the globally optimized parameters shown in Fig. 4.5. 60

4.8 Correlation of the reference DFT forces with the one computed using the trained force field. The latter ones are computed with the shells having been relaxed from their initial positions. Again, no noticeable improvement can be seen compared to the results of the globally optimized parameters shown in Fig. 4.6. 60

5.1 Diagram of the implemented fitting procedure. 65

5.2 Representation of the typical directed graph resulting of the use of the *FitterWorkChain*. WorkChains and Calculations are represented by orange boxes, structures by blue circle, input dictionaries by light orange circles and results by green circles. Supercell* represent a supercell with no partial occupancy and Supercell** one with added thermal noise. 66

5.3 DFT versus Coulombic energy for random structures of 5 classes of ionic conductors (LATP, LISICON, LGPS, LLTO and LLZO) showing high correlation between both models. 67

5.4 Schematic representation of the *PartialOccupancyWorkChain* with *Reservoir sampling*. Each Monte Carlo step correspond to numerous swap attempts within the different group of sites. After the step, the structure is selected or discarded with probability i/n, with i the current step and n the target number of selection leading to an equiprobable selection of all the visited structures. 68

5.5 Distribution of the displacement of each ionic species from their mean position in trajectories at 300, 600 and 900 K. The dashed line shows the Maxwell-Boltzmann distributions parametrized to minimize the mean square error. . . 69

5.6 DFT versus Coulombic energy of randomly selected structures for the two phases of lithium tantalate with partially occupied sites. The orange line show the slope, α of the linear fit of the data. 70

5.7 Energy along Monte-Carlo trajectories used to resolve the occupancy of partially occupied sites of structures A (**left**) and B (**right**), corresponding to the ICSD entries 74949 [137] and 413372 [37] respectively. Three temperatures, 300 K (**blue**), 600 K (**orange**) and 900 K (**green**) are shown. Next to the energy is displayed the energy distribution of the visited states after the initial equilibration. 71

5.8 Energy along Monte-Carlo trajectories of structure C, corresponding to the ICSD entry 413372 [37] with the sites correctly grouped to guarantee the occupancy of all four lithium sites at three temperature, 300 K (**blue**), 600 K (**orange**) and 900 K (**green**). Next to the energy is displayed the energy distribution of the visited states after the initial equilibration. 71

5.9 Radial distribution function, $g(r)$, of lithium tantalate structures generated using Monte-Carlo and artificial thermal noise. Three distributions of the thermal noise are compared with various standard deviations: Maxwell-Boltzmann (**left**), normal (**center**) and exponential (**right**). The radial distribution function of a first-principle trajectory is also drawn for reference. 72

5.10 Distribution of the amplitude of the atomic forces in the reference DFT trajectories (**green**) compared to the ones generated using a mean displacement of 0.1 (**blue**) and 0.2 Å (**orange**). The distributions are shown for lithium (**left**), tantalum (**center**) and oxygen (**right**) particles. 73

5.11 Pair potentials parametrized for the Li – O, Ta – O and O – O pairs with enforced barriers of 5, 10, 20 and 40 eV and parameters described in Table 5.1. The parameter for all potentials can be found in Table 5.2. 74

5.12 Correlation plot between the reference DFT energies and the one given by the force-field after relaxation of the shells. 75

5.13 Correlation plot between the reference DFT forces and the ones given by the force-field after relaxation of the shells. 76

5.14 Volumes, lattice parameters and angles averaged over NPT trajectories between 300 and 900 K using the force-field obtained with a minimum barrier ΔU of 5, 10 and 20 eV. The volume shows a linear increase without phase change. Similarly, the length of the lattice vectors and angle stay stable throughout the simulations. Each point is averaged over 750 ps of simulation and the error is estimated using bloc averages over blocs of 150 ps. 77

5.15 Mean square displacement at temperatures between 100 and 700 K for 750 ps of NPT trajectories with a maximum lag time of 200 ps. The trajectories were produced using the globally optimized force-field with minimum barriers of 5 10 and 20 eV. The MSD is presented for three phases of lithium tantalate described by their ICSD collection ids. 78

5.16 Comparison of the diffusion coefficients corresponding to the mean square displacements shown in Fig. 5.15 with their respective activation energies. . . 79

5.17 Mean square displacement at temperatures between 100 and 900 K for 750 ps of NVT and NVE trajectories. The trajectories were produced using the globally optimized force-field with minimum barriers of 10 and 20 eV. 80

5.18 Diffusion coefficients at temperatures between 100 and 900 K computed from NPT trajectories of 750 ps. The trajectories were produced using the globally optimized force-field with minimum barriers of 10 and 20 eV. 81

6.1 The same SSE instability reaction in a closed-circuit cell (a) and open-circuit cell (b). CE = counter electrode, RI = reaction interface, E = electrode, A = mobile species (Li, Na, . . .). 85

6.2 The stoichiometry deviation z in the general SSE composition $A_{n+z}M$ as a function of the electrode potential Φ as derived from two simple models for generic values of the model parameters, cf. Supporting Information. 90

6.3 Stoichiometry stability windows and phase stability windows for various Li-SSE materials (a) and NASICON (b). *For Li-SSE materials (a), published phase stability windows from Ref [141] are plotted. For NASICON (b) the phase stability window was computed with our own implementation. 96

6.4 Width $\Delta\Phi^{\mathrm{stoi}}$ of the stoichiometry stability windows in comparison with the HOMO–LUMO gap $\Delta E^{\mathrm{N}}_{\mathrm{HL}}$ for the investigated SSE materials. 99

6.5 Comparison of stability windows computed with PBE and with HSE06 DFT functionals. (a) Phase stability windows and stoichiometry stability windows. (b) Width $\Delta\Phi^{\mathrm{stoi}}$ of the stoichiometry stability windows and HOMO–LUMO gaps $\Delta E^{\mathrm{N}}_{\mathrm{HL}}$. 101

A.1 The stoichiometry deviation z in the general SSE material $A_{n+z}M$ as a function of the potential Φ as derived from the two models in the limit $|z| \ll n$: The '1 type A-site model' considers all A-sites energetically equivalent, whereas the '2 type A-site model' takes into account two energetically different types of A-sites. The values of the model parameters used for the plotted curves are given in the text. 112
A.2 Ewald (Coulomb) energies vs. DFT energies for selected SSE materials. 116

List of Tables

3.1 Summary of the polarizable Buckingham force field used to investigate the dynamics of LLZO. 30

3.2 Fitting of the autocorrelation function of the site occupancies (Fig. 3.12) according to the model in Eq. 3.11. The first three lines report results for the explicit doping scheme, while the last one refers to the implicit doping model. 43

4.1 Parameter space used for the initial global optimization of the lithium tantalate force-field. 56

5.1 Parameter ranges for the reported training. 70

5.2 Parameters of globally optimized force-field using populations of 100 individuals and starting from different random populations. The Li – O and Ta – O pair parameters converge to very similar values while the O – O pair shows the largest difference. 74

6.1 Input .cif-files, structures, and supercells for the investigated SSE materials. . . 95

6.2 Results from DFT computations with PBE functional and SSSP Efficiency pseudopotentials: Lower and upper limits $\Phi^{\mathrm{stoi}}_{\mathrm{red\,/\,ox}}$ and corresponding width $\Delta\Phi^{\mathrm{stoi}}$ of the stoichiometry stability windows for the investigated SSE materials. Potential limits are given vs. the reference potential of A-metal oxidation (A=Li for Li-SSE materials, A=Na for NASICON). Also given are the electronic HOMO–LUMO gaps $\Delta E^{\mathrm{N}}_{\mathrm{HL}}$ of the systems with stable A-stoichiometry N. 97

6.3 Results from hybrid functional DFT computations with HSE06 functional and SG15 ONCV pseudopotentials: Lower and upper limits $\Phi^{\mathrm{stoi}}_{\mathrm{red\,/\,ox}}$ and corresponding width $\Delta\Phi^{\mathrm{stoi}}$ of the stoichiometry stability windows, and the electronic HOMO–LUMO gaps $\Delta E^{\mathrm{N}}_{\mathrm{HL}}$ of the systems with stable A-stoichiometry N. 102

1 Introduction

The lithium-ion battery technology has matured over the last two decades, driven by the high requirements of the 3C market – computers, consumer electronics and cameras. The development of new markets and the drive for ever smaller batteries with larger capacities have changed the landscape. Beside consumer electronics becoming ever more smaller and powerful, requiring always higher capacities, the rise of hybrid and electric powered vehicles has pushed for batteries with higher than ever energy densities. With the current growth of these new markets and no indication that the demand will stagnate or decline, as shown with the yearly battery sales in Fig. 1.1, the motivation for new advances in the Li-ion and beyond Li-ion technologies is stronger than ever.

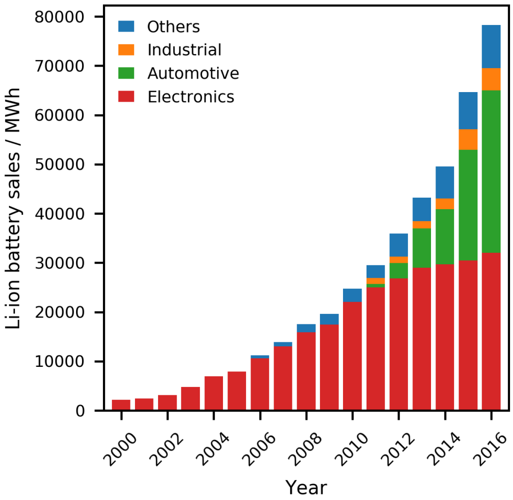

Figure 1.1 – Worldwide Lithium-ion sales for electronics, industrial and automotive applications, and others (namely power tools, e-bikes, medical devices, etc) from 2000 to 2016. [1]

Lithium-ion is widely believed to be reaching soon its limits in terms of specific energies and energy densities, casting a doubt on the technology's ability to cope with the increasing requirements [4, 5, 6]. In this context, intense efforts has been put in evaluating alternative battery technologies, including Li/O_2, Li/S systems and batteries substituting lithium for single (Na^+ and K^+) or multivalent (Mg^{2+} and Ca^{2+}) ions. These technologies are however far from mature and important research efforts are still needed to unlock the potential of the next generation of batteries.

Lithium Batteries

The research in the field of lithium batteries started with the pioneering work of Lewis [7] on lithium electrodes in 1912. 50 years later, Harris [8] noticed the stability of metallic lithium in a number of non-aqueous electrolytes, opening the door to the development of lithium batteries. In the wake of this discovery, the 1960s witnessed the fabrication and commercialization of a variety of the first non-rechargeable primary lithium batteries. In the early 70s, the discovery of reversible insertion of alkali metal ions into iron cyanide compounds by Armand [9] allowed the development of the first rechargeable secondary lithium-metal batteries. Lithium metal technology however faced major safety concerns preventing any commercial breakthrough after their first investigations [10, 11] in the 90s. Later proposed in the second half of the 70s by Armand, the concept of lithium-ions batteries, a battery using two different intercalation compound at each electrodes was demonstrated in the 80s. Both primary and secondary lithium batteries have become widely used in the modern world. Active research and development helped discover new alternative electrode materials allowing for smaller and lighter batteries with ever increasing energy density.

Today's rechargeable battery technology however still faces challenges. As the Li-ion technology slowly reaches its limit, the need for alternative technology has increased. Among the possible candidates, lithium-air and lithium-sulphur batteries have attracted a particular interest. Their reliance on metalic lithium anodes [12, 13, 14, 15, 16, 17] has however been an important drawback as the safety issues associated with the metallic lithium anodes have not disappeared. During the charging process, lithium is deposited non-homogeneously to form high surface area lithium (HSAL), often referred as "dendrites". Beside the continual consumption of the electrolytes during the re-formation of the solid electrolyte interface (SEI), this phenomenon poses safety concerns due to textiti) the high reactivity of HSAL with the electrolyte and (*ii*) the possibility of short circuits in the electrochemical cell if the dendrite grows through the electrolytes and reaches the cathode. These risks are important obstacles to the development of new technologies. Beyond the safety threats, liquid electrolytes also poses environmental concerns through the potential of leakage and containment issues during production and recycling. As the liquid organic electrolytes are central to the issues faced, substitution of the liquid electrolytes by safer and more convenient alternatives has been explored.

Ionic liquids Ionic salts are organic salt composed of ionic species. They offer a high thermal stability, good electrochemical stability, and are recyclable and non-flammable. Their organic nature allows for their physico-chemical properties to be easily tailored through substitution and functionalization [18]. All these advantages would make of ionic liquids the ideal electrolytes if it wasn't for their high viscosity resulting in extremely low ionic conductivity.

Polymer electrolytes First investigated by Fenton et al. in the early 70s, polymer electrolytes were later recognized by Armand [19] for their potential application in lithium batteries. The high conductivity achieved in recent development as well as their mechanical properties makes them interesting replacement for liquid organic electrolytes. Among them, polyvinylidene fluoride (PVdF) is the most commonly used today [20]. They however suffer from poor interfacial stability and are not stable against metallic lithium, preventing their use in the higher capacity Li-metal batteries.

Solid State Electrolytes

After early reports of the mobility of ions such as Ag$^+$, O^{2-} or F$^-$ in solids in the nineteenth century, solid states electrolytes gained traction with the rise of the transistors and electronics, promising relatively high voltage power sources with low total current. These investigation led to multiple designs proposal for primary batteries [21, 22, 23, 24]. Several inorganic compounds have been investigated since as potential solid-state electrolytes with candidates ranging from oxides to non-oxides, and from crystalline to amorphous.

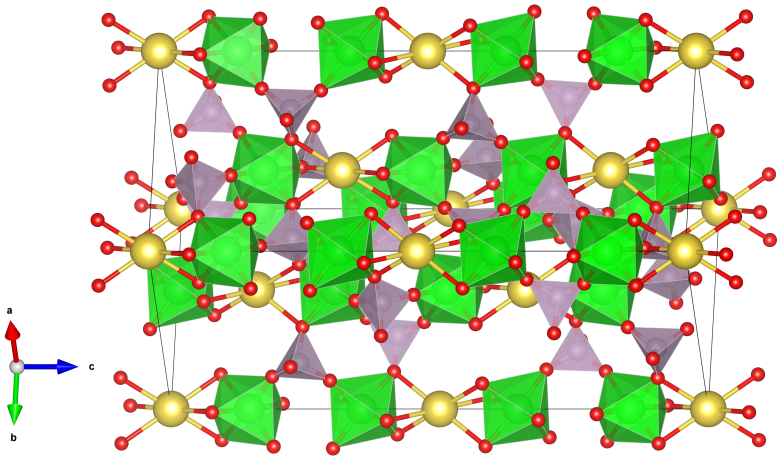

Figure 1.2 – Crystal structure of $NaZr_2(PO_4)_3$, the base structure of NaSICON-type electrolytes with the P centers represented as purple tetrahedra and the Zr ones as green octahedra. Figure generated using the VESTA software [2].

NaSICON type electrolytes **Na** **S**uper**I**onic **CON**ductors (NaSICON) were first reported in 1976 by Goodenough and Hong [25, 26]. Of the form $Na_{1+x}Zr_2Si_xP_{3-x}O_{12}$ $(0 \leq x \leq 3)$, they are derived from the $NaM_2(PO_4)_3$ structure, presented in Fig. 1.2, by partial substitution of Si for P. Substitution of the Na by Li does not affect the structure of the material and produces an isostructural lithium conductor. It's conductivity is however reduced when compared to the sodium one. The decrease in conductivity results from the too large ionic channels and the stronger bonding energy between the Li and O atoms. Aluminium doping allows the conductivity of NaSICON-type electrolytes to be tuned. $Li_{1+x}AlxTi_{2-x}(PO_4)_3$ (LATP) and $Li_{1+x}AlxGe_{2-x}(PO_4)_3$ (LAGP) exhibit room temperature conductivity of up to 10^{-3} [27] and $10^{-2}\,S\,cm^{-1}$ [28] respectively.

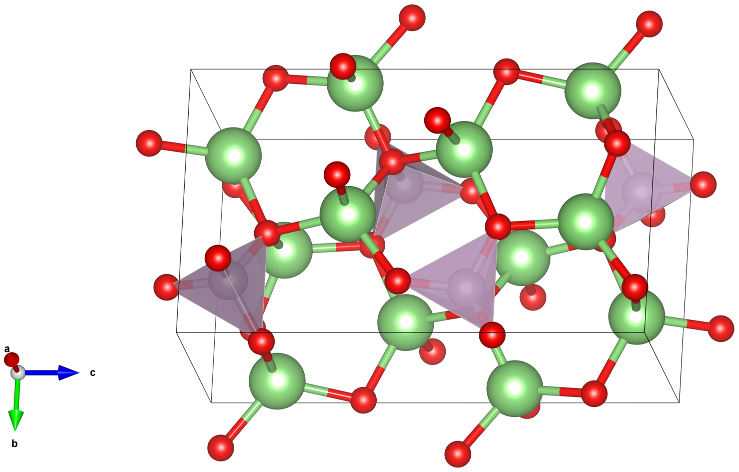

Figure 1.3 – Crystal structure of γ-Li_3PO_4, the base structure of LiSICON-type electrolytes with the P centers represented as purple tetrahedra. Figure generated using the VESTA software [2].

LiSICON type electrolytes With a structure similar to γ-Li_3PO_4, shown in Fig 1.3, the **Li** **S**uper**I**onic **CON**ductor (LiSICON) family results from the substitution of aliovalent cation for the P ones. The first reported example by Hong [29] in 1978, $Li_{14}Zn(GeO_4)_4$ had a conductivity of $0.13\,S\,cm^{-1}$ at $300°C$. Although LiSICON are well suited to operate at high temperature, their extremely low ionic conductivity has resulted in a limited number of reported compounds.

Thio-LiSICON and LGPS-type electrolytes In 2000, Kanno [30] substituted S for O and reported the thio-LiSICON family. The high polarizability of the S^{-2} anion weakens the interaction with the lithium and leads to a higher conductivity. Of particular interest among these is the LGPS family – $Li_{4-x}Ge_xP_{1-x}S_4$ – for which the highest conductivity was reported with $x = 0.75$, $2.17 \cdot 10^{-3}\,S\,cm^{-1}$ at 26°C [31]. More recently, Kanno's group reported a new thio-LiSICON compound $Li_{9.54}Si_{1.74}P_{1.44}S_{11.7}Cl_{0.3}$ [32]. It's structure is related the one of LGPS and it possesses a remarkably high ionic conductivity, $2.5 \cdot 10^{-2}\,S\,cm^{-1}$.

Perovskite electrolytes After first report of ionic conductive perovskites, ABO_3, by Takahashi and Iwahara [33] in the early 70s, Inaguma *et al.* discovered materials of general formula $Li_{3x}La_{2/3-x}TiO_3$ (LLTO), with ionic conductivity as high as $10^{-3}\,S\,cm^{-1}$ [34] at room temperature. Despite their high conductivity at room temperature, the application of LLTO remains limited by its tendency to undergo rapid Li insertion, with consequent Ti reduction from Ti^{4+} to Ti^{3+}, when in contact with metallic lithium resulting in high electronic conductivity.

Lithium Tantalate

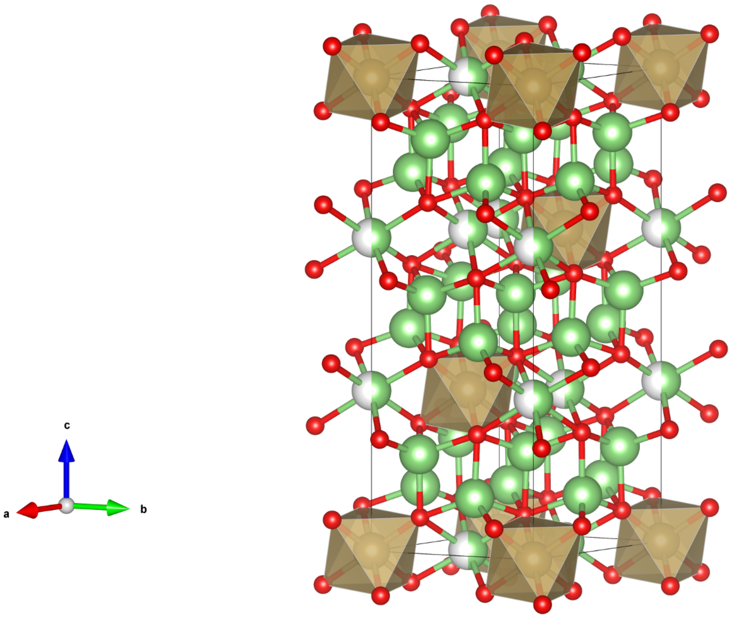

Figure 1.4 – Crystal structure of Li_7LaO_6. Figure generated using the VESTA software [2].

Hexaoxometalates have first been described by Scholder [35] in 1958, describing iso structural compounds of formula Li_8MO_6 (M = Sn, Pb, Zr, Hf) and Li_7MO_6 (M = Nb, Ta, Sb, Bi). The presence of Li vacancies in the Li_7 structures allowed for a higher conductivity and their investigation as solid states electrolytes. In 1979, Delmas *et al.* [36] reported a room temperature conductivity of $4.3 \cdot 10^{-8}\,S\,cm^{-1}$ for Li_7TaO_6, shown in Fig. 1.4, with an activation energy of 0.66 eV.

In a more recent study, Muhle *et al.* [37] reported a phase transition in the Arrhenius plots of various hexaoxometalates, including Li_7TaO_6 around 700 K with a dramatic drop in the activation energy to 0.28 eV for Li_7TaO_6. Since they couldn't observe any changes in the X-ray diffraction patterns concurrent with the transition, they assign it to a melting of the lithium sublattice allowing a greater mobility.

Garnet-type electrolytes

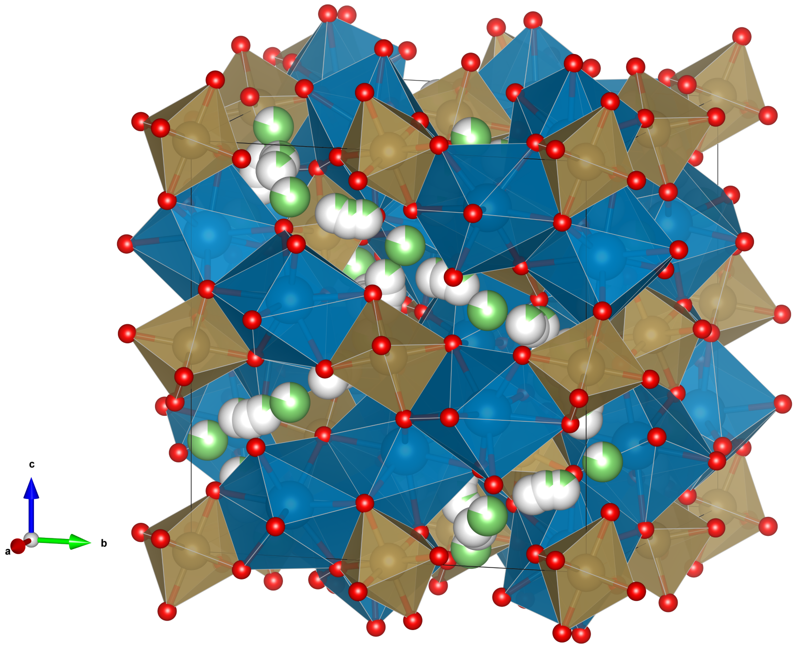

Figure 1.5 – Crystal structure of $Li_5La_3Ta_2O_{12}$. The La centers are represented in blue and the Ta ones in brown. Li sites are represented in green. Figure generated using the VESTA software [2].

After the discovery of LLTO, a strong effort was put in the search for materials with similar constituents but with a higher electrochemical stability. Attempts to substitute Zr for Ti failed due to the thermodynamically favorable formation of a non conductive pyrochlore phase. Reported in the late 80s by Abbattista [38], Hyooma [39] and Mazza [40], $Li_5La_3B_2O_{12}$, $B = Nb, Ta$ is one such structure, which forms a cubic garnet-like phase shown in Fig. 1.5. Garnets are orthosilicates of general composition $A_3B_2(SiO_4)_3$ in which A and B are eight- and six-coordinated cations. Lithium containing garnets substitute lithium for silicon and are separated in two groups: conventional lithium garnets, $A_3B_2(LiO_4)_3$, and stuffed lithium garnets, $Li_xA_3B_2(LiO_4)_3$. The lithium cations occupy the $24d$ tetrahedral sites labeled as Li1 in Fig. 1.6. In stuffed garnets, the tetrahedral sites are saturated and the lithium is force to occupy the $96h$ sites with a distorted octahedral coordination and labeled as Li2 in Fig. 1.6. In 2003, Thangadurai *et al.* [41], first investigated the structure for its ionic conductivity. The high versatility of the garnet structure, allowing various substitution of alio- and hypervalent cations for both A and B lead to numerous attempts to improve the conductivity and stability of the system. In 2007, Murugan *et al.* reported a new electrolyte of the garnet family, $Li_7La_3Zr_2O_{12}$ (LLZO) with relatively high ionic conductivity, $10^{-4}\,S\,cm^{-1}$, and excellent stability against metallic lithium [42].

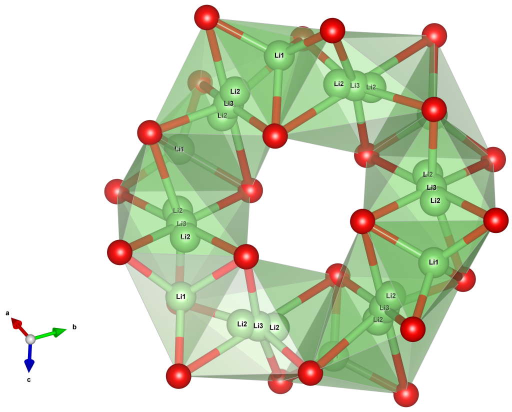

Figure 1.6 – Crystal environment of the lithium in the garnet structure. The most stable site is the Li1, $24d$, tetrahedral site. In stuffed garnets, two degenerate Li2, $96h$, distorted octahedral sites are then occupied. The two degenerate sites are situated next to the *ideal* $48g$ octahedral Li3 site. Figure generated using the VESTA software [2].

Complete ordering of the lithium content in LLZO can occur in the case of tetragonally distorted garnets[43], reducing the intra- and inter-grain conductivity by about three orders of magnitude. Later investigations by Geiger *et al.* [44] show that the tetragonal, non-conducting phase is the lower energy phase and the more stable one at room temperature. They also suggested that the stability of the cubic phase at room temperature in the seminal reports by Murugan *et al.* is the result of Al contamination from the aluminium crucible used for the synthesis.

Substantial studies have taken place since then to optimize the stability and conductivity of garnet electrolytes through doping.

Simulation of Solid-State Electrolytes

The potential of solid-state electrolytes has not only fueled intensive experimental work but also many theoretical studies. These theoretical works, starting in the mid-70s, have been focused on the understanding of the mechanism of superionic conductivity to better drive the discovery of new and better performing materials. In 1976, Rahman [45] first investigated the self-diffusion of F^- ions in CaF_2 crystals using tabulated potential reported earlier by Kim *et al.* [46]. Further studies using diverse classical force fields, molecular and Monte Carlo dynamics, followed the development in the field. They included the simulation of various halides [47, 48, 49, 50, 51, 52], Li_3N [53] and α- and $\beta''-Al_2O_3$ [54, 55, 56, 57].

It was however not before 2006 that Wood *et al.* were able to use first-principle methods, namely Car-Parinello molecular dynamics, to model the diffusive phenomenon in α-AgI [58].

Simulation of garnet-type electrolytes

First-principle based simulations

In 2012, Xu *et al.* investigated the structure and diffusion mechanism using DFT [3]. In particular they were interested in the analysis of the lithium site occupation after structure relaxation and of the diffusion mechanism using the nudged elastic band (NEB) method. They report high occupation of the tetrahedral sites for the lower lithium concentrations investigated, $Li_3La_3Te_2O_{12}$ and $Li_5La_3Nb_2O_{12}$. For the higher concentration, $Li_7La_3Zr_2O_{12}$, the tendency is reverse after relaxation, their simulation favoring the occupation of the octahedral sites. They also suggest two main diffusion mechanisms for that structure. The first one is done by the migration of a lithium ion from an octahedral site to another going through the connecting tetrahedral site. They report an activation energy of about 0.25 eV for each of the two steps of the process. The second mechanism bypasses the tetrahedral site and exhibits a higher activation energy of 0.8 eV. Both mechanisms are presented in Fig. 1.7.

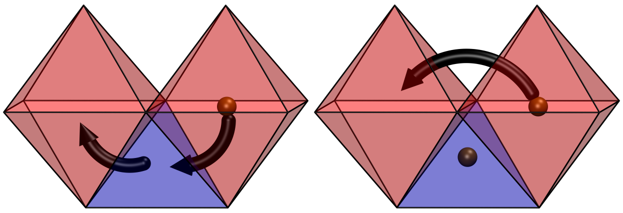

Figure 1.7 – Representation of the two mechanisms proposed by Xu *et al.*. The octahedral sites and the tetrahedral one are respectively represented in red and blue [3].

Simultaneously Bernstein *et al.* [59] used first-principles molecular dynamics (FPMD) in an isothermal-isobaric ensemble to understand the impact of the Li concentration on the structure of LLZO. In particular they demonstrate that the removal of Li from the stoichiometric structure lowers the critical temperature of the transition from the tetragonal phase to the cubic one by increasing the overall entropy of the system and reducing the gain in free energy achieved by ordering the lithium in the tetragonal phase.

Later in 2013, Jalem *et al.* [60] used FPMD to investigate the superionic phenomenon in cubic LLZO. In particular they focused the determination of the diffusion coefficient from the lithium self-diffusion and on the average occupation of the different sites. They postulate a concerted migration mechanism governed by restriction on neighboring site occupation and the unstable residence of the lithium ion in the tetragonal site. Although the value obtained for the activation energy is consistent with experimental results, the length of simulation used, 30 ps, is extremely short and it is difficult to asses the convergence of the presented diffusion coefficients.

Miara *et al.* [61] studied the impact of Rb and Ta doping on the topology and ionic conductivity of LLZO. They used dopant distribution optimized to minimize coulombic repulsion in a $1 \times 1 \times 1$ cell to model conductivity in trajectories lasting from 40 to 100 ps. They conclude that the primary effect of the doping is the change in lithium concentration rather than the size or nature of the migration path.

Meier2014 *et al.* [62] introduced the use of metadynamics to reach a better understanding of the conductivity of LLZO and more specifically to contrast the different mechanism present in the cubic and tetragonal phase. Though they observe a collective motion of the ions in the case of the tetragonal phase, there observations for the cubic phase describes a sequence of asynchronous single-ion jumps leading to the apparent collective motion of a few ions. This result contrast with the observation of Jalem *et al.* described earlier [60].

Rettenwander *et al.* investigated the the site occupation of Al^{3+} dopant using DFT calculations [63]. Their results indicate that the $24d$ site is energetically favored, although they do report shallow minima for a tetrahedral coordination on the $96h$ site and for an octahedral one on the $48g$ site. Despite previous neutron diffraction studies proposing the occupation of the $48g$ site by Al^{3+} by Li *et al.* [64], the NMR shift predicted for the site was not observed in experimental NMR spectra. In a later publication [65] they further investigated the effect of Ga^{3+} and Al^{3+} on the local potential of the neighboring lithium sites through DFT.

In a joint experimental and theoretical study, Mukhopadhyay *et al.* [66] used neutron diffraction (ND), X-ray diffraction (XRD) measurements and Raman spectroscopy in conjunction with DFT calculations to investigate the effect of Ta and Al doping on the crystal structure. They observed smaller experimental lattice constants than the one expected from their first-principles calculations. They postulated that this is the result of an higher than nominal Ta content in the structure. They further suggest that O vacancies are formed to keep the charge balance neutral. They also investigated Ta and Al doping in term of the effect the dopant has on Li channel size, *i.e.* Li1 and Li2 site sizes and size of the neck that Li must pass through to travel between them. They observed that Ta enlarges all three quantities, while Al leaves the site sizes unchanged but enlarges the neck.

In a recent work, Klenk *et al.* investigated the impact of various GGA functionals on the predicted lattice parameters and phase transition of LLZO [67]. They report errors within 10% from the experimental results for all functionals and a stabilization of the cubic phase at a temperature of 1000°C when using PBE2, SOGGA and PBESol as exchange correlation functional.

Force-field based simulations

Adams *et al.* reported in 2012 [68] a combined experimental and theoretical study, in which they used classical modeling based on a Morse-type potential to gain a better understanding of the lithium dynamics in LLZO and Ta^{5+}– and Nb^{5+}–doped structures. An initial bond-valence (BV) analysis lead the authors to conclude that no low energy interstitial site should play a role in the Li^+ transport in garnet electrolytes as proposed by Xu *et al.* [3]. They report a phase transition in good agreement with their experimental observations. Later experimental studies [69, 70] however report critical temperature for the phase transition ($650°C$) higher than the one reported here ($450°C$). Their work underlined the advantages of classical modeling for the research in the field of solid state electrolytes. The cell used for all simulations was a $2 \times 2 \times 2$ supercell, greatly improving the statistical significance of the results. Furthermore, the timescale of the simulation allows to converge conductivity for lower temperatures, *e.g.* > 1 ns at 323 K.

Wang *et al.* [71] used a polarizable Buckingham potential to investigate the lithium distribution in tetragonal and in cubic Ta-doped LLZO. They modeled both O and Ta ions using a core-shell model. They observed an increase of the Li^+ ion ordering for higher lithium composition until total ordering is reached for Li_7. Based on their simulations, they also predicted lower occupation of the tetragonal sites than what was previously reported [72, 73].

Effects of Ga^{3+}–doping on the structure and conductivity of LLZO was investigated by Jalem *et al.* [74] using a non-polarizable Buckingham potential. Their model successfully describe the stabilization of the cubic phase by the decrease in lithium content induced by the Ga dopant. It is however unable to fully reproduce the tetragonal phase. They did not observe any lattice change due to the substitution and predict Ga diffusion above 1200 K. They finally observed two regimes in the conductivity behavior with respect to the lithium content: an initial decrease for $0 \leq x \leq 0.1$ followed by a flat trend for $0.1 \leq x \leq 0.3$. This first behavior is explained by the initial increase in inaccessible sites occupied by Ga ions. At higher dopant concentration they suggested that the increase in Li vacancies allows ions to conserve momentum in the percolated pathways.

In a first paper, Klenk *et al.* [75] used a polarizable Buckingham potential to investigate the local structure and dynamics of LLZO. They analysed van Hove correlation functions and mean square displacement and concluded that the lithium dynamics in the cubic phase predominantly consists of what they call "structured diffusion", a combination of oscillation and random-walk diffusion. When looking at the phase transition their results are aligned with previous studies and hint at an entropic stabilisation of the cubic phase at higher temperature. They finally investigated the presence of local clusters of Li ions and find few regularly occuring clusters in both tetragonal and cubic phases. They believe that these mostly symmetrical clusters lead to a "center-pass" mechanism dominating the diffusion phenomena through these bottlenecks.

In a second paper, Klenk *et al.* [76] investigated, this time with a non polarizable Buckingham potential, the convergence of the structure parameter and conductive behavior of LLZO with respect to the size of the system used. Although they did not observe large variation in the cell parameters, conductivity or Haven ratio, they recommend the use of a $3 \times 3 \times 3$ supercell for an optimal trade-off between accuracy and performance.

Burbano *et al.* presented long-time simulation of both tetragonal and cubic phase LLZO using a DIPole Polarizable Ionic Mode (DIPPIM) potential [77]. They performed runs of up to 87.4 ns to effectively sample the diffusion phenomenon in the low conductive tetragonal phase. Of particular interest to them was the identification of strings, chains of ions diffusing in concert. They identified in tetragonal LLZO a strong bias towards 8 membered strings, corresponding to a cyclic excitation event. This preference for long diffusive chains is not preserved in the cubic phase where the probability of observing a long string decays exponentially with the length of the chain. These observations are consistent with the observations made by Meier *et al.* [62] in regards to the collective aspect of ionic motion in cubic and tetragonal LLZO.

More recently, Chen *et al.* [78] used a combination of classical and DFT modeling to investigate Ta doping of LLZO. They investigated the change in structure between the cubic and tetragonal phase in term of Li-Li pair distribution function and lithium density maps. They then investigated the different conduction pathways in term of temperature-dependent site occupancy and explained the site preference as a consequence of the DFT site energy difference. They finally investigated the effect of the doping on the lithium distribution. They observed an increase in the occupancy of the tetrahedral with doping that they attribute to a stabilization of the tetrahedral site by the Ta ions.

Problematic

Computational investigations targeted at solid-states electrolytes aim at creating a deeper understanding of the various phenomena that control and influence the conductivity of a crystal. Although this type of investigation is often presented as the promise of the identification of better materials, most new electrolytes are still discovered by intuition or serendipity. This stems from the numerous issues still present for the simulation of solid-states electrolytes, raising a host of interwoven choices, with the balance between accuracy and performance at its core. First-principle methods have proven their efficacy in accurately modeling such solid since the first reported modeling of ionic diffusion by Wood *et al.* [58]. However due to the high cost of the method, DFT studies have remained limited to static modeling, small simulation cells and short time scales. This is particularly problematic when studying less conductive structures such as the tetragonal phase of LLZO where the diffusive process is driven by rare events. Enhanced sampling methods such as metadynamics can be used to improve the understanding of the processes at stake, as shown by Meier *et al.* [62] but not without a trade-off with the loss of information relative to time-scale central to the idea of diffusion. Given these limitations, force-field modeling has proved its role as an essential tool in understanding and predicting the conductivity of solid state electrolytes.

In particular polarizable force fields have shown to be able to provide increased accuracy in the description of some complex systems. In the first part of the thesis, the goal is to demonstrate the use of classical polarizable force-field to improve the understanding of some of the issues related to the modeling of doped systems solid-state electrolytes. To this end, a prototypical system, W doped LLZO, of formula $\mathrm{Li}_{7-2x}\mathrm{La}_3\mathrm{Zr}_{2-x}\mathrm{W}_x\mathrm{O}_{12}$, is used. A comparison between two doping models, an *implicit* scheme and an *explicit* one, is made to identify the different impact of the doping on the stability and the Li-ion dynamics of the system.

The second part focuses on methodologies used for the development of classical polarizable force-fields, with a particular focus on methodologies applicable in the scope of material screening and identification of potential solid-state electrolytes. To make the use of force-field in such procedure, it is important to have convenient tools available for the parametrization of the force-field. A general framework for the unsupervised parametrization of polarizable force-fields is developed using the AiiDA platform [79] and tested on lithium tantalate.

2 Methods

Molecular dynamics simulation

Molecular dynamics (MD) is a technique used to compute equilibrium and transport properties of systems of classical particles. In many regards, it is very similar to real experiments, where a sample of the material that one wishes to study is first prepared and then measurements are carried out using various instruments to determine a quantity of interest during a certain time interval. In molecular dynamics, a model system composed of particles is assembled and Newton's equations of motion are integrated for the system until the properties of the system do not change with time, *i.e.* the system has reached equilibrium. In the case of equilibrium properties, the measurements of the property of interest are then taken. In both experimental and theoretical cases, the measurements are subject to statistical noise and the more data is collected, the more accurate the measurements will become. Computer simulations therefore act as a bridge between the microscopic time and length scales and the macroscopic world of lab experiments.

Integrating the equation of motion

When considering a system of N atoms described by the $3N$ coordinates $\mathbf{r} = \{r_i\}$, by the potential $U(\mathbf{r})$ and by the $3N$ momenta $\mathbf{p} = \left\{p_i\right\}$, the total energy of the system can be defined as the hamiltonian $H\left(\mathbf{r},\mathbf{p}\right) = U(\mathbf{r}) + K\left(\mathbf{p}\right)$, where $K\left(\mathbf{p}\right) = \sum_i^{3N} {|p_i|^2}/{2m_i}$. The evolution of the system then follows the classical equations of motion

$$\frac{d}{dt} r_i = \frac{p_i}{m_i} \qquad \text{and} \qquad \frac{d}{dt} p_i = -\frac{\partial}{\partial r_i} U(\mathbf{r}) = f_i \tag{2.1}$$

The most common technique used to integrate the equations of motion of a system is the Verlet algorithm. By using a Taylor series on the updated coordinates after and before a timestep Δt, the following equations can be written for the coordinate i

$$\begin{aligned}
r_i(t+\Delta t) &= r_i(t) + \frac{d}{dt}r_i(t)\Delta t + \frac{d^2}{dt^2}\frac{r_i(t)}{2}\Delta t^2 + \frac{d^3}{dt^3}\frac{r_i(t)}{6}\Delta t^3 + \mathcal{O}\left(\Delta t^4\right) \\
&= r_i(t) + \frac{p_i(t)}{m_i}\Delta t + \frac{f_i(t)}{2m_i}\Delta t^2 + \frac{d^3}{dt^3}\frac{r_i(t)}{6}\Delta t^3 + \mathcal{O}\left(\Delta t^4\right) \\
r_i(t-\Delta t) &= r_i(t) - \frac{d}{dt}r_i(t)\Delta t + \frac{d^2}{dt^2}\frac{r_i(t)}{2}\Delta t^2 - \frac{d^3}{dt^3}\frac{r_i(t)}{6}\Delta t^3 + \mathcal{O}\left(\Delta t^4\right) \\
&= r_i(t) - \frac{p_i(t)}{m_i}\Delta t + \frac{f_i(t)}{2m_i}\Delta t^2 - \frac{d^3}{dt^3}\frac{r_i(t)}{6}\Delta t^3 + \mathcal{O}\left(\Delta t^4\right)
\end{aligned} \tag{2.2}$$

When added together, the momentum and third-order derivative of the coordinates can be removed from the equation:

$$r_i(t+\Delta t) + r_i(t-\Delta t) = 2r_i(t) + \frac{f_i(t)}{m_i}\Delta t^2 + \mathcal{O}\left(\Delta t^4\right). \tag{2.3}$$

It is then easy to rewrite the equation to define the updated coordinates as a function of the previous and current coordinates and of the forces

$$r_i(t+\Delta t) \approx 2r_i(t) - r_i(t-\Delta t) + \frac{f_i(t)}{m_i}\Delta t^2. \tag{2.4}$$

As demonstrated, the Verlet algorithm doesn't need the momenta to compute the updated coordinates. The momenta are however necessary to keep track of the total energy of the system. By reusing Eq. 2.2 it is however possible to define the evolution of the momenta. This time, by subtracting the two equations, we can eliminate the the current position, forces and forth-order terms.

$$r_i(t+\Delta t) - r_i(t-\Delta t) = 2\frac{p_i(t)}{m_i}\Delta t + \mathcal{O}\left(\Delta t^3\right). \tag{2.5}$$

Rewriting the equation, leads to the expression for the updated momenta

$$p_i(t) = \frac{r_i(t+\Delta t) - r_i(t-\Delta t)}{2\Delta t} + \mathcal{O}\left(\Delta t^2\right). \tag{2.6}$$

Momenta calculated this way are however only accurate to order Δt^2 and can only be computed on $r_i(t+\Delta t)$ is known. Alternative schemes allow to obtain more accurate estimates of the velocities and remove the necessity of knowing the next updated positions. The Velocity-Verlet algorithm is one of these. Its derivation is very similar to the one of the Verlet. One starts with a Taylor series around the momentum at time t.

$$\begin{aligned}
p_i(t+\Delta t) &= p_i(t) + \frac{d}{dt}p_i(t)\Delta t + \frac{d^2}{dt^2}\frac{p_i(t)}{2}\Delta t^2 + \mathcal{O}\left(\Delta t^3\right) \\
&= p_i(t) + f_i(t)\Delta t + \frac{d^2}{dt^2}\frac{p_i(t)}{2}\Delta t^2 + \mathcal{O}\left(\Delta t^3\right).
\end{aligned} \tag{2.7}$$

Unlike in the case of the Verlet algorithm, this first expansion is not sufficient since no expression is known for the second-order derivative of the momentum. A second Taylor series describing the first derivative of the momentum around time t, is used.

$$\frac{d}{dt}p_i(t+\Delta t) = \frac{d}{dt}p_i(t) + \frac{d^2}{dt^2}p_i(t)\Delta t + \mathcal{O}\left(\Delta t^2\right). \tag{2.8}$$

By isolating the second-order derivative of the momentum in Eq. 2.8 and multiplying it by ${}^{\Delta t}/_{2}$, one obtains an expression for the second-order term of Eq. 2.7:

$$\frac{d^2}{dt^2}\frac{p_i(t)}{2}\Delta t^2 = \frac{\Delta t}{2}\left(\frac{d}{dt}p_i(t+\Delta t) - \frac{d}{dt}p_i(t)\right) + \mathcal{O}\left(\Delta t^3\right). \tag{2.9}$$

Substituting Eq. 2.9 into Eq. 2.7 gives the final expression for the updated momenta as a function of the initial momenta and of the forces at times t and $t+\Delta t$.

$$\begin{aligned} p_i(t+\Delta t) &= p_i(t) + \frac{d}{dt}p_i(t)\Delta t + \frac{\Delta t}{2}\left(\frac{d}{dt}p_i(t+\Delta t) - \frac{d}{dt}p_i(t)\right) + \mathcal{O}\left(\Delta t^3\right) \\ &= p_i(t) + \frac{\Delta t}{2}\left(f_i(t+\Delta t) + f_i(t)\right) + \mathcal{O}\left(\Delta t^3\right) \end{aligned} \tag{2.10}$$

The integration of the equation of motion using the Velocity-Verlet method is done in four steps:

1. calculate $r_i(t+\Delta t) = r_i(t) + {}^{p_i(t)}/_{m_i}\Delta t + {}^{f_i(t)}/_{2m_i}\Delta t^2$,
2. calculate $p_i\left(t+{}^{1}/_{2}\Delta t\right) = p_i(t) + {}^{1}/_{2}f_i(t)\Delta t$,
3. evaluate $f_i(t+\Delta t) = -{}^{\partial}/_{\partial r_i}U(\mathbf{r}(t+\Delta t))$,
4. calculate $p_i(t+\Delta t) = p_i\left(t+{}^{1}/_{2}\Delta t\right) + {}^{1}/_{2}f_i(t+\Delta t)\Delta t$.

Generalized Langevin Equation Thermostat

The integration of the equation of motion leads to a sampling of the microcanonical constant-energy ensemble. Real-life experiment are however done at constant temperature, not constant energy. Several approach have been proposed to achieved such simulations, a few examples are listed here. Andersen's thermostat rescales the momenta of the particles to respect a Maxwell-Boltzmann distribution at the desired temperature [80]. Nosé-Hoover's thermostat uses the momentum of a fictitious particle as a heat bath [81, 82]. Nosé-Hoover's chains improve on Nosé-Hoover's thermostat by using a chain of fictitious particles instead of a single one [83]. Velocity rescaling uses a constant α to enforce a target temperature [84], a more recent version includes a properly chose randomness to the rescaling factor [85].

In this work, constant temperature simulations are performed using a non-Markovian Langevin equation based thermostat [86]. When considering a system of particles described by the coordinates $\mathbf{r} = \{r_i\}$, momenta $\mathbf{p} = \{p_i\}$ and masses $\mathbf{m} = \{m_i\}$ and interacting via a potential $U(\mathbf{r})$, the colored Langevin equations are defined as

$$
\begin{aligned}
&\frac{d}{dt} r_i(t) = p_i(t) / m_i \\
&\frac{d}{dt} p_i(t) = -f_i(t) - \int_0^t \mathcal{K}\left(t - t'\right) p_i\left(t'\right) \mathrm{d}t' + \xi_i(t)
\end{aligned}
\tag{2.11}
$$

where $f_i = -{}^{\partial U}/_{\partial r_i}$ are the forces, $\mathcal{K}$ is a memory kernel and $\xi(t)$ is a vector of independent Gaussian noises. Of particular interest, if the noise term ξ is related to the memory kernel $\mathcal{K}$ by the fluctuation-dissipation theorem $\left\langle \xi_i(t) \xi_j\left(t'\right)\right\rangle = \delta_{ij} m_i T \mathcal{K}\left(t - t'\right)$, the temperature of the system can be set to T.

Though the non-Markovian Eq. 2.11 seem too complex for practical application, the use of memory kernel of a rather general form $\mathcal{K} = \Re \sum_k c_k e^{-t(\gamma_k + i\omega_k)}$ with $\gamma_k > 0$, allows to rewrite Eq. 2.11 into an equivalent Markovian form by introducing a set of auxiliary momenta:

$$
\begin{aligned}
&\frac{d}{dt} r_i(t) = s_{0i}(t) / m_i \\
&\frac{d}{dt} \mathbf{s}_i(t) = \begin{bmatrix} f_i(t) \\ 0 \\ \vdots \\ 0 \end{bmatrix} - \mathbf{A} \cdot \mathbf{s}(t) + \mathbf{B} \cdot \eta_i(t)
\end{aligned}
\tag{2.12}
$$

where $\mathbf{s}_i = \left(p_i, s_{i1}, \ldots, s_{iN}\right)^T$ is a $N+1$ dimensional vector, whose first component is associated with the i-th degree of freedom of the system, and η_i is a vector of Gaussian white noise satisfying $\left\langle \eta_{ik}(t) \eta_{ik'}\left(t'\right)\right\rangle = \delta_{ij} \delta\left(t - t'\right) \delta_{kk'}$. The matrices $\mathbf{A}$ and $\mathbf{B}$ are the drift and diffusion matrices. They are related to the static covariance matrix [87] $\mathbf{C} = \langle (p, \mathbf{s})^T (p, \mathbf{s}) \rangle$ by the equation

$$
\mathbf{AC} + \mathbf{CA}^T = \mathbf{BB}^T. \tag{2.13}
$$

Ref. [87] shows that the use of $\mathbf{C} = k_{\mathbf{B}} T$ is sufficient to satisfy the fluctuation-dissipation theorem. As a consequence, for a given $\mathbf{A}$, $\mathbf{B}$ can be derived.

Ab-Initio Molecular Dynamics

In the previous parts, the basics for the integration of the equations of motion needed for molecular dynamics was discussed. One aspect has however been mentioned multiple times but never discussed in details. The calculation of the forces from the system's potential is the most time-consuming part of most molecular dynamics simulations. Different level of theories can be used to compute them giving rise to trajectories of various cost and accuracy. By far the most accurate but most expensive way of computing these forces relies on the theories of quantum mechanics.

In 1926, Erwin Schrödinger introduced a new way to describe a particle of mass m in an external potential V, by what is now know as the Schrödinger equation [88].

$$\left(-\frac{\hbar^2}{2m}\nabla^2 + V\right)\Psi(\mathbf{r},t) = i\hbar\frac{\partial}{\partial t}\Psi(\mathbf{r},t) \tag{2.14}$$

where $\Psi(\mathbf{r},t)$ is a complex function of time and the particle position and whose square is a probability distribution function:

$$\int_S |\Psi(\mathbf{r},t)|^2 \,\mathrm{d}\mathbf{r} = 1 \tag{2.15}$$

where the integral is made over the whole space. If the potential V only depends on the position of the particle $\mathbf{r}$, and assuming the function Ψ can be separated into the product of a time dependent and a position dependent function

$$\Psi(\mathbf{r},t) = u(\mathbf{r})\, f(t), \tag{2.16}$$

Eq. 2.14 can be split into a time-dependent and a time-independent part:

$$\frac{1}{u(\mathbf{r})}\left(-\frac{\hbar^2}{2m}\nabla^2 + V\right)u(\mathbf{r}) = \frac{i\hbar}{f(t)}\frac{\partial}{\partial t}f(t). \tag{2.17}$$

This equality can only be valid, if both sides of the equation are equal to a constant. Calling this constant E, Eq. 2.17 can be split into the following two equations:

$$\hat{H}u(\mathbf{r}) = \left(-\frac{\hbar^2}{2m}\nabla^2 + V\right)u(\mathbf{r}) = Eu(\mathbf{r}) \tag{2.18}$$

$$i\hbar\frac{\partial}{\partial t}f(t) = Ef(t), \tag{2.19}$$

where $\hat{H}$ represents the Hamiltonian operator, the operator for the total energy of the system. The solution of Eq. 2.19, called the time-dependent Schrödinger equation, is a pure phase factor

$$f(t) = \beta e^{\frac{iEt}{\hbar}} \tag{2.20}$$

where β is a constant. The only way to obtain the total energy of the system is therefore to solve Eq. 2.18, known as the time-independent Schrödinger equation. In the case of a many-body system, the equation can be rewritten as

$$\left(-\sum_i \frac{\hbar^2}{2m_i}\nabla_i^2 + \sum_{i<j}\frac{q_i q_j}{\left|\mathbf{r}_i - \mathbf{r}_j\right|}\right)u(\mathbf{r}) = Eu(\mathbf{r}) \tag{2.21}$$

where m_i and q_i are the mass and charge of the particle i and the second summation is over all pairs i, j. The simplicity of Eq. 2.21 is deceptive and the problem needs to be simplified in order to be solved.

In 1927, Born and Oppenheimer observed that due to the extreme difference in the mass of the electrons and nuclei, one could assume the electron dynamics to happen at timescales where the nuclei are frozen in place. In mathematical terms, this means that the nuclear and electronic wavefunctions can be separated,

$$\Psi = \psi_{\text{nuclear}} \cdot \psi_{\text{electronic}}. \tag{2.22}$$

To solve for the electronic wavefunction, one includes the nuclei as a fixed external potential in the equation

$$\left(-\frac{\hbar^2}{2m} \sum_i^n \nabla_i^2 + \sum_i^n \sum_I^N \frac{q_I e^2}{|\mathbf{r}_i - \mathbf{r}_I|} + \sum_{i<j} \frac{e^2}{\left|\mathbf{r}_i - \mathbf{r}_j\right|} \right) \psi_{\text{electronic}} = E_{\text{electronic}} \psi_{\text{electronic}} \tag{2.23}$$

where the sum $\sum_i^n$ sums over all electrons, the sum $\sum_I^N$ over all nuclei and the sum $\sum_{i<j}$ over all electron pairs, m is the electron mass and q_I is the charge of the nucleus I.

The development of a self-consistent approximation for the resolution of the Schrödinger equation by Hartree and the later introduction by Slater and Fock of anti-symmetric wavefunctions provide a simplified framework to easily solve Eq. 2.23, the Hartree-Fock method (HF). Despite the HF method being accurate enough to provide satisfactory starting points to the description of many properties, its costs remains high. To go further, two quantities must be defined. The error in energy due to the use of antisymmetric wavefunctions is called the exchange energy, E_{X}, and the difference between the many-body energy and the HF energy is called the correlation energy, E_{C}.

Density Functional Theory

Systems composed of n electrons have so far been described by a $3n$ coordinates plus n spins wavefunction, $\psi\left(x_1, y_1, z_1, \sigma_1, ..., x_n, y_n, z_n, \sigma_n\right)$. A physical property, A, of the system corresponding to a one-electron operator, $\hat{A}$, can be expressed as

$$\begin{aligned} A &= \sum_i^n \int \cdots \int \psi^* \left(x_1, ..., \sigma_n\right) \hat{A}\left(x_i, y_i, z_i\right) \psi\left(x_1, ..., \sigma_n\right) \mathrm{d}\tau_1 ... \mathrm{d}\tau_n \\ &= \int\int\int \hat{A}\left(x, y, z\right) \rho\left(x, y, z\right) \mathrm{d}x\mathrm{d}y\mathrm{d}z. \end{aligned} \tag{2.24}$$

where

$$\rho\left(x, y, z\right) = n \int \cdots \int \psi^* \left(x_1, ..., \sigma_n\right) \psi\left(x_1, ..., \sigma_n\right) \mathrm{d}\tau_1 ... \mathrm{d}\tau_n \tag{2.25}$$

is the probability of finding an electron in the volume $\mathrm{d}x\mathrm{d}y\mathrm{d}z$ around the point (x, y, z) and where $\mathrm{d}\tau_i = \mathrm{d}x_i\mathrm{d}y_i\mathrm{d}z_i\mathrm{d}\sigma_i$ is used for the integration over the spatial coordinates x_i, y_i and z_i, and the summation over the spin coordinate σ_i.

This formalism is useful since it only requires the knowledge of the electron density and not of the wavefunction itself. It however wasn't thought to work in this form for the case of more-than-one-electron operators, the Hamiltonian operator being one of them. In 1964, Hohenberg and Kohn presented a solution to this issue. First they showed that the ground-state energy, as well as all other ground-state properties, could be expressed as a function of the ground state electron density:

$$E = E[\rho] \tag{2.26}$$

where the use of square brackets is the standard notation to denote the integral involving $\rho(x, y, z)$. They then showed that Eq. 2.26 is variational, *i.e.*

$$E_0 = E[\rho_0] \leq E[\rho] \tag{2.27}$$

where E_0 and ρ_0 denote the ground-state energy and electron density and ρ denotes any trial electron density.

The main issue with the first Hohenberg-Kohn theorem (Eq. 2.26 is that it is simply an *existense theorem*. Though they rigorously proved that it is possible to express the ground-state energy as a functional of the electronic density, the exact functional needed is not known. The Kohn-Sham formalism attempts to solve this issue by introducing an artificial reference system of non-interacting electrons yielding the exact same electron density as the fully interacting system. The electronic energy can then be partitioned into four contributions:

$$E_{\text{electronic}}[\rho] = T_S[\rho] + V[\rho] + J[\rho] + E_{\text{xc}}[\rho] \tag{2.28}$$

where $T[\rho]$ is the kinetic energy of the non-interacting reference system, $V[\rho]$ the interaction energy with the potential created by the nuclei, $J[\rho]$ the Coulomb interactions of the electrons and $E_{\text{xc}}[\rho]$ is the exchange-correlation effects of the system, i.e. it contains all the non-classical electron-electron interactions as well as the difference in kinetic energy between the non- and fully-interacting systems.

The Local Density Approximation

The Local Density Approximation (LDA) is historically and often practically the most important type of approximation for the exchange-correlation energy. Systems of interest such as atoms, molecules or solid are simultaneously inhomogeneous (the electric field produced by the nuclei is not spatially homogeneous) and interacting (the electrons interact with each other through Coulomb interactions). In order to simplify the problem, LDA splits it into two simpler though non trivial problems: one non-interacting inhomogeneous ($T_S[\rho]$, $V[\rho]$ and $J[\rho]$)

and the other interacting homogeneous $E_{\text{xc}}\left[\rho\right]$. The exchange-correlation term can be split into an exchange and a correlation term: $E_{\text{xc}} = E_{\text{x}} + E_{\text{c}}$. The derivation of the exchange part is straightforward. The per volume exchange energy for an homogeneous electron gas is known exactly as

$$E_{\text{x}}^{\text{hom}}\left(\rho\right) = -\frac{3q^2}{4}\left(\frac{3}{\pi}\right)^{1/3}\rho^{4/3}. \tag{2.29}$$

The total exchange energy for the system is therefore

$$E_{x}^{\text{LDA}}\left[\rho\right] = -\frac{3q^2}{4}\left(\frac{3}{\pi}\right)^{1/3}\int\int\int\rho\left(x,y,z\right)\mathrm{d}x\mathrm{d}y\mathrm{d}z. \tag{2.30}$$

The derivation of the correlation energy is however more problematic as the correlation energy for a homogeneous electron gas is not known exactly. Early approximations of $E_{\text{c}}^{\text{hom}}\left(n\right)$ derived from perturbation theory have now been replace by more modern version parametrized using data obtained using Quantum Monte Carlo methods. The final expression becomes

$$E_{\text{xc}}\left[\rho\right] \approx E_{\text{xc}}^{\text{LDA}}\left[\rho\right] = \int\int\int E_{\text{xc}}^{\text{hom}}\left(\rho\right)\mathrm{d}x\mathrm{d}y\mathrm{d}z\bigg|_{\rho\to\rho\left(x,y,z\right)} = \int\int\int E_{\text{xc}}^{\text{hom}}\left(\rho\left(x,y,z\right)\right)\mathrm{d}x\mathrm{d}y\mathrm{d}z \tag{2.31}$$

where $E_{\text{xc}}^{\text{hom}} = E_{\text{x}}^{\text{hom}} + E_{\text{c}}^{\text{hom}}$. This approximation has proven to be effective even for system quite different from the reference system that is the homogeneous electron gas. Partial explanation for the success of LDA is a systematic error cancellation between the LDA's tendency to underestimate E_{c} and overestimate E_{x}. This systematic error cancellation results in unexpectedly good E_{xc} values.

The Generalised Gradient Approximation

Within the LDA, one assumes a locally homogeneous electron density for every point in space. Real systems are however inhomogeneous. It can be easily seen that including information about the gradient of the electron density can be useful. A first attempt at it, the Gradient-Expansion Approximation (GEA) applied gradient-corrections of the form $\left|\nabla\rho\left(x,y,z\right)\right|$, $\left|\nabla\rho\left(x,y,z\right)\right|^2$, $\nabla^2\rho\left(x,y,z\right)$, etc. to LDA. However, this type of correction almost never improved on the LDA and often worsens it. Following these trials, it was realized that more general function of $\rho\left(x,y,z\right)$ and $\nabla\rho\left(x,y,z\right)$ could be used instead of the power-series-like GEA. This new approach, known as Generalised Gradient Approximation (GGA), introduces functionals of the general form

$$E_{\text{xc}}^{\text{GGA}}\left[\rho\right] = \int f\left(\rho\left(x,y,z\right),\nabla\rho\left(x,y,z\right)\right)\mathrm{d}x\mathrm{d}y\mathrm{d}z. \tag{2.32}$$

Unlike different LDA functionals where the difference resides in the way of parametrizing a similar expression $E_{\text{xc}}^{\text{hom}}\left(\rho\right)$, GGA functionals differs in the method used to construct the function $f\left(\rho, \nabla\rho\right)$. In general, GGA improves on LDA, particularly in the description of all main types of chemical bonds.

Bloch's theorem

Previous sections have introduced the basic concepts of DFT to describe systems of atoms in term of single electron wavefunctions. When considering solid phases, the number of electrons is infinite. The need for a new representation of the problem is therefore needed. In 1929, Bloch provided a solution to the issue. He stated that in a periodic potential

$$V(r) = V(r + L) \tag{2.33}$$

where L is the lattice vector, the electronic wavefunction can be expressed as the product of a cell-periodic part and a wave-like part

$$\psi_k(r) = e^{ik\cdot r} f(r). \tag{2.34}$$

Bloch's theorem transform the problem of an infinite number of electrons into expressing a single-electron wavefunction in term of an infinite number of reciprocal space vectors, k, within the first Brioullin zone of the crystal.

Since f is periodic, it can be expanded in term of a Fourier series

$$f(r) = \sum_G c_G e^{iG\cdot r} \tag{2.35}$$

where G are the reciprocal lattice vectors defined by $G \cdot L = 2\pi m$, where m is an integer, and c_G are the plane wave expansion coefficients. Though the number of plane-wave needed is infinite, truncation of the series for plane-waves with higher energies is possible since their coefficients are typically much smaller. The one-electron wavefunction can be written as

$$\psi_k(r) = \sum_G c_{k+G} e^{i(k+G)\cdot r}. \tag{2.36}$$

Despite having traded an infinity of electrons for an infinity of reciprocal lattice vectors k, the wavefunction is stable for close values of k. This means that only a finite number of k-points need to be used to sample the Brioullin zone.

The use of plane waves is also possible in the density functional theory framework. Starting from the Kohn-Sham equation

$$\left[-\frac{\hbar}{2m}\nabla^2 + V(r) + J(r) + V_{\text{xc}}(r)\right]\psi(r) = \epsilon\psi(r) \tag{2.37}$$

The Fourier transform of the potentials V, J and V_{xc}, give

$$F(G) = \int_S \frac{1}{v} e^{-iG\cdot r} F(r)\, \mathrm{d}^3 r \tag{2.38}$$

where G is the reciprocal lattice vector, v the unit cell volume and F is one of V, J and V_{xc} and the integral is done over the whole unit cell.

Substituting Eq. 2.36 and the inverse Fourier transform $F(r) = \sum_G F(G)\, e^{iG\cdot r}$ into Eq. 2.37 gives

$$\sum_{G'} c_{k+G'} \left[\left(\frac{\hbar}{2m} |k+G|^2 - \epsilon \right) e^{i(k+G')\cdot r} + \sum_{G''} \left(V(G'') + J(G'') + V_{\text{xc}}(G'') \right) e^{i(k+G'+G'')\cdot r} \right] = 0. \tag{2.39}$$

By multiplying Eq. 2.39 by $^1/_v e^{-i(k+G)\cdot r}$ and integrating over r, one obtains

$$\frac{1}{v} \sum_{G'} c_{k+G'} \int \left[\left(\frac{\hbar}{2m} |k+G|^2 - \epsilon \right) e^{i(G'-G)\cdot r} + \sum_{G''} \left(V(G'') + J(G'') + V_{\text{xc}}(G'') \right) e^{i(G'+G''-G)\cdot r} \right] \mathrm{d}^3 r = 0. \tag{2.40}$$

Eq. 2.40 can further be simplified by taking advantage of $\int e^{ik\cdot r}\, \mathrm{d}^3 r \equiv \delta_{q,0}$:

$$\begin{aligned} \sum_{G'} c_{k+G'} \left[\left(\frac{\hbar}{2m} |k+G|^2 - \epsilon \right) \delta_{G,G'} + \sum_{G''} \left(V(G'') + J(G'') + V_{\text{xc}}(G'') \right) \delta_{G'',G-G'} \right] &= 0 \\ \sum_{G'} c_{k+G'} \left[\left(\frac{\hbar}{2m} |k+G|^2 - \epsilon \right) \delta_{G,G'} + V(G-G') + J(G-G') + V_{\text{xc}}(G-G') \right] &= 0 \end{aligned} \tag{2.41}$$

Finally, from Eq. 2.41, one obtains the Kohn-Sham equation in the reciprocal space:

$$\sum_{G'} \left[\frac{\hbar}{2m} |k+G|^2 \delta_{G,G'} + V(G-G') + J(G-G') + V_{\text{xc}}(G-G') \right] c_{k+G'} = c_{k+G}\epsilon \tag{2.42}$$

Force-Field based Molecular Dynamics

Despite the progress made to speed up DFT-based MD by means of the Car-Parrinello approach [89] and the more recent wavefunction extrapolation methods [90], DFT-MD simulations of medium to large molecular systems (100-500 atoms) are still limited to the ps time scale. For this reason, DFT-MD is poorly suited for the calculation of slow thermodynamics properties such as ionic conductivity in solid-state electrolytes at lower temperatures or in larger supercells. To overcome these difficulties, *first-principle* techniques need to be complemented by more approximate but more efficient approaches based on model Hamiltonians. Among these, force-field based MD (FFMD) is certainly one of the most successful methods for the calculation of long trajectories (μs- ms time scales) and the sampling of the configuration space. As such, it is of particular interest for the purpose of this work, namely the evaluation of the ionic diffusion coefficients in solid-state electrolytes.

FFMD methods were first introduced by Alder and Wainwright [91] in 1957 for the modeling of the phase transition of hard spheres. Although the core concepts remains essentially unchanged, the force-field Hamiltonians and their parameterization have improved substantially in the last decades, turning FF-MD into the method of choice in the simulation of chemical inert molecular and solid state systems.

The FF Hamiltonian is generally composed of several two- (Coulomb and van der Waals interactions, bonds), three- (angles) and four-body terms (dihedrals) of immediate physical meaning. When considering inorganic solids, the common practice has been to consider all atoms in their fixed ionic state and to describe the energy of the system by means of purely non-bonded potentials, *i.e.* long-range Coulomb and short range van der Waals interactions. This work also considers the polarization of the anions through an extra term in the Hamiltonian.

$$H_{\mathrm{FF}} = H_{\mathrm{Coulomb}} + H_{\mathrm{VdW}} + H_{\mathrm{Pol}} \tag{2.43}$$

Short range van der Waals potentials

A first approximation of the short range van der Walls interactions was proposed by Jones in 1924 [92]:

$$\begin{aligned} V_{\mathrm{LJ}}\left(r_{ij}\right) &= 4\epsilon\left[\left(\frac{\sigma}{r_{ij}}\right)^{12} - \left(\frac{\sigma}{r_{ij}}\right)^{6}\right] \\ &= \epsilon\left[\left(\frac{r_{\mathrm{m}}}{r_{ij}}\right)^{12} - 2\left(\frac{r_{\mathrm{m}}}{r_{ij}}\right)^{6}\right], \end{aligned} \tag{2.44}$$

where r_{ij} is the distance between the considered particles i and j, ϵ is the depth of the potential, σ the finite distance at which the potential is equal to zero and r_m is the distance at which the potential reaches its minimum value. However since r_m and σ are connected through $r_m^6 = 2\sigma^6$, this potential lacks some flexibility. To account for this Buckingham proposed in 1938 an improved and more flexible version of the potential in which the r^{12} repulsive term is replaced by a decaying exponential term [93].

$$V_{\mathrm{Buck}}\left(r_{ij}\right) = \epsilon\left(\frac{6}{\alpha-6}e^{\alpha\left(1-\frac{r_{ij}}{r_{\mathrm{m}}}\right)} - \frac{\alpha}{\alpha-6}\left(\frac{r_{\mathrm{m}}}{r_{ij}}\right)^{6}\right) \tag{2.45}$$

where ϵ and r_{m} still control the depth and minimum energy distance and α is a third parameter introduced by Buckingham to control the steepness of the potential around the minimum energy distance. Eq. 2.45 can be rewritten using the following relations

$$A = \frac{6\epsilon}{\alpha-6}e^{\alpha}, \qquad \rho = \frac{r_m}{\alpha} \qquad \text{and} \qquad C = \frac{\alpha\epsilon}{\alpha-6}r_m^6 \tag{2.46}$$

to yield a simplified form of the Buckingham potential

$$V_{\mathrm{Buck}}\left(r_{ij}\right) = Ae^{-\frac{r_{ij}}{\rho}} - \frac{C}{r_{ij}^6}. \tag{2.47}$$

This second form allows more flexibility in the parametrization of the potential by decoupling its repulsive and attractive parts and has been preferred in the past.

Polarizability

Polarizability is integrated into the FF Hamiltonian by using the core-shell model introduced in 1958 by Dick and Overhauser [94]. Observing that previous studies had demonstrated that the polarizability of ions were mostly due to the electrons of the outermost shells, the one in the inner shells being tightly bound to the nucleus, they proposed to model the ions using a shell of n valence electrons and a core consisting of the nucleus and the remaining core electrons. Exposed to an electric field, the system becomes polarized through the displacement of the shell with respect to the position of the core. To ensure the polarizability is finite, an harmonic potential with spring constant k acts between the shell and the core. A representation of the core-shell model is proposed in Fig. 2.1. The polarizability of such a system can easily be related to its parameters n and k using the basic definitions of polarizability, of the Coulomb force and of the restoring force of a harmonic potential:

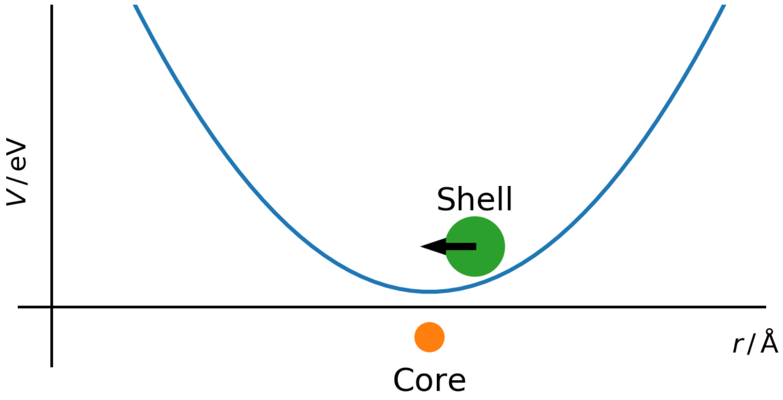

Figure 2.1 – Schematic representation of the core-shell model. The shell is trapped in a harmonic potential centered on the core of the atom.

$$p = \alpha E, \qquad E = \frac{F_E}{q} \quad \text{and} \quad F_k = -kx \tag{2.48}$$

where E is an electric field, α is the polarizability of the system and p is electric dipole produced by the field in the system, F_E is the force applied by an electric field on a charge q, and F_k is the force resulting of the harmonic potential with spring constant k for a displacement x.

If the coordinates of the nucleus is considered as the origin of the coordinate system, the dipole describing the core-shell system is equal to $p_{\mathrm{cs}} = x(ne)$, where e is the charge of an electron. At equilibrium, the force resulting of the shell interaction with the electric field and the one resulting of the displacement of the shell must cancel each other

$$|F_E| = E(ne) = kx = |F_k| \tag{2.49}$$

by substituting in the system dipole and polarizability, the equation becomes

$$\frac{x(ne)^2}{\alpha} = kx \tag{2.50}$$

that can be reduced to

$$\alpha = \frac{(ne)^2}{k} \tag{2.51}$$

This equality gives an opportunity to parametrize the core-shell model, assuming that the polarizability of the ion is known. By considering the charge of the shell as a parameter, we can express the spring constant as a function of said charge and polarizability.

$$k(n) = \frac{(ne)^2}{\alpha} \tag{2.52}$$

Although the core-shell model dates, its usage was for a long limited by its computational cost as it dramatically increases the number of particles in the system. Initial implementations were based on the self-consistent optimization of the position of massless shells between each integration step of the dynamics. To improve the performance of the model, the dynamics of the shells were later integrated to the the system by borrowing some mass from the cores. This method however requires smaller integration steps for the dynamics as the shells mass remains extremely small and therefore prone to large integration error.

Measuring Diffusion

Conductivity

The conductivity, σ_a, of a system is related to the mobility of its charge carrier λ_a by

$$\sigma_a = N_a \, q_a \, \lambda_a \tag{2.53}$$

where N_a and q_a are the number of carriers and their charge. This applies as much for electrical conductors than for the ionic ones. Though the conductivity can be observed experimentally using impedance spectroscopy, there is no easy way to derive ionic conductivity directly from molecular dynamics simulations. The Nernst-Einstein equation provides a solution to this problem by connecting the ionic mobility of the charge carrier to its diffusion coefficient, D_a,

$$\frac{\lambda_a}{D_a} = \frac{q_a}{k_\mathrm{B} T} \tag{2.54}$$

Eq. 2.54 can be derived by considering a system "blocked" between two electrodes with an electric potential ϕ applied to it. As a result of the potential, the charge carriers will experience a force that will push them to accumulate in the region of low potential. An equilibrium state will be reached when the diffusional flow following the carrier concentration gradient cancels out the flow resulting of the potential.

$$D_a^I \, \frac{\partial C_a(x)}{\partial x} = -C_a(x) \, \lambda_a \, \frac{\partial \phi}{\partial x} \tag{2.55}$$

where D_a^I is the intrinsic diffusion coefficient of the carrier and C_a is the fraction of sites occupied. For simplicity, it will be assumed that D_a^I and λ_a are constants. It follows that $D_a^I = D_a$, where D_a is the self-diffusion coefficient of the carrier. Integrating Eq. 2.55 gives

$$C_a = K \, e^{\frac{-\lambda_a \phi}{D_a}} \tag{2.56}$$

Eq. 2.56 can be compared to the well known prediction of the Maxwell-Boltzmann distribution

$$C_a = K \, e^{\frac{-q_a \phi}{k_\mathrm{B} T}}. \tag{2.57}$$

Equating the members in the exponential lead to the Nernst-Einstein equation

$$\frac{\lambda_a}{D_a} = \frac{q_a}{k_\mathrm{B} T} \tag{2.58}$$

McKee [95] showed how the exact same result can be found when removing the assumption that D_a^I and λ_a are constants. The ionic conductivity can be directly linked to the diffusion coefficient by combining Eq. 2.54 and 2.53

$$\sigma = \frac{N_a q_a^2 D_a}{k_\mathrm{B} T} = \frac{n_a z^2 F^2 D_a}{RT} \tag{2.59}$$

More generally, to remove the dependency on the sample size, the molar number of carriers n_a is replaced by its concentration, c_a in the system yielding

$$\sigma = \frac{c_a z^2 F^2 D_a}{RT} \tag{2.60}$$

Diffusion coefficient

It was shown in the previous part that the conductivity of a system could be expressed as a function of the self-diffusion coefficient of the charge carrier. It remains to show how that quantity can be expressed from a molecular dynamics trajectory. The self-diffusion coefficients can be obtained through one of two equivalent ways.

The first one uses the Green-Kubo relations to give an exact mathematical expression of the diffusion coefficient D in term of an integral of the velocity autocorrelation function

$$D = \frac{1}{d}\int_0^{\infty} \langle \mathbf{v}(t_0)\,\mathbf{v}(t_0+t)\rangle_{t_0}\,\mathrm{d}t \tag{2.61}$$

where d is the dimensionality of the system.

The second approach uses the displacement of the particles rather than their velocities:

$$\mathbf{r}(t) - \mathbf{r}(t_0) = \int_{t_0}^{t} \mathbf{v}\left(t'\right)\mathrm{d}t'. \tag{2.62}$$

The square of the displacement is therefore equal to

$$(\mathbf{r}(t) - \mathbf{r}(t_0))^2 = \int_{t_0}^{t}\int_{t_0}^{t} \mathbf{v}\left(t''\right)\mathbf{v}\left(t'\right)\mathrm{d}t''\mathrm{d}t'. \tag{2.63}$$

By taking an ensemble average, substituting $t'' = t' + s$ and integrating over t', one obtains:

$$\left\langle (\mathbf{r}(t) - \mathbf{r}(t_0))^2 \right\rangle = 2\int_0^{t} (t-s)\,\langle \mathbf{v}(t_0)\,\mathbf{v}(t_0+s)\rangle_{t_0}\,\mathrm{d}s. \tag{2.64}$$

By taking the derivative with respect to t, one finally recover the integral of the velocity autocorrelation function:

$$\frac{\partial}{\partial t}\left\langle (\mathbf{r}(t) - \mathbf{r}(t_0))^2 \right\rangle = 2\int_0^{t} \langle \mathbf{v}(t_0)\,\mathbf{v}(t_0+s)\rangle_{t_0}\,\mathrm{d}s. \tag{2.65}$$

Substituting Eq.2.65 back into Eq. 2.61, one obtains

$$D = \frac{1}{2d}\frac{\partial}{\partial t}\left\langle (\mathbf{r}(t) - \mathbf{r}(t_0))^2 \right\rangle \tag{2.66}$$

In the limit where $t \to \infty$, Eq. 2.66 is equivalent to the Einstein equation:

$$D = \frac{1}{2d}\frac{\left\langle (\mathbf{r}(t) - \mathbf{r}(t_0))^2 \right\rangle}{t} \tag{2.67}$$

When considering the self-diffusion of charged particles, as is the case with solid-state electrolytes, two different perspective can be used to observe the displacements of the charge carrier. In the first one, $\mathbf{r}(t)$ refers to the individual positions of the particles at time t and the ensemble average is taken over all particles. In the second point of view, $\mathbf{r}(t)$ represent the position of the center of mass of the carrier and already contains the ensemble average over all particles. The resulting diffusion coefficients are named $tracer$ and $charge$ diffusion coefficients.

$$D_{\mathrm{Tr}} = \lim_{t\to\infty} \frac{1}{2d} \frac{\left\langle (\mathbf{r_i}(t_0+t) - \mathbf{r_i}(t_0))^2 \right\rangle_{i,t_0}}{t} \tag{2.68}$$

$$D_{\sigma} = \lim_{t\to\infty} \frac{1}{2d} \frac{\left\langle \left(\langle \mathbf{r_i}(t_0+t) \rangle_i - \langle \mathbf{r_i}(t_0) \rangle_i \right)^2 \right\rangle_{t_0}}{t} \tag{2.69}$$

where r_i represent the position of the particle i and $\langle \cdots \rangle_X$ represents a mean over the quantity X.

Activation energy

Although the previous chapters have shown that it is possible to compare the experimental conductivity of materials to the one of their simulations, there is often a discrepancy in the results. Another value that can provide valuable information is however the activation energy of the diffusive process.

In chemistry, the rates of rate-limited thermally activated processes follow the Arrhenius law

$$k = A e^{\frac{-E_a}{k_\mathrm{B} T}} \tag{2.70}$$

where k is the reaction rate, A is a reaction dependent pre-exponential factor and E_a is the activation energy of the reaction. Since diffusion is also a rate-limited thermally activated process, a similar equality can be observed for the diffusion coefficient where

$$D = D_\circ e^{\frac{-E_a}{k_\mathrm{B} T}} \tag{2.71}$$

Consequently, when plotting the logarithm of the diffusion coefficient against the inverse temperature one should obtains a linear relation

$$\log D = \log D_\circ - \frac{E_a}{k_\mathrm{B} \ln 10} \frac{1}{T}. \tag{2.72}$$

The values of the activation energy of simulated system is often much more accurate than the absolute values of the conductivity. It is therefore an interesting value to compute and compare to experiment.

3 Lithium dynamics in LLZO

Introduction

This chapter aims at deepening the understanding of the issues related to the use of classical modelling in the description of the LLZO systems, and in particular of doped structures. The physics of W-doped systems, with formula $Li_{7-2x}La_3Zr_{2-x}W_xO_{12}$ is investigated, from both a kinetic (barriers and conductivity) and thermodynamic (phase stability) standpoint. The choice of the system was motivated by the experimental results provided by Li *et al.* [96], where several dopant concentrations and temperatures were explored with a consistent synthesis approach. The work mainly differs from previous analysis [68, 71, 74, 75, 76, 77, 78] by its focus. The target is to resolve the effects on the dynamics resulting from the change in charge carrier concentration and from the introduction of the doping agents. To this end, the comparison between two doping models is made: (*i*) an implicit model using a uniform background charge to compensate for the change in lithium ion concentration and (*ii*) an explicit model using substitution of hypervalent ions. For the second model, an additional averaging over the positions of the W ions is introduce to account for the frozen noise of the dopant distribution. The results are also analyzed within the framework of spin glass theory. Results shows that doping affects the conductivity both through a change of the charge carriers density and an increased potential barrier for the hopping by the hypervalent dopants. The delicate interplay between these two effects is what makes the physics of doped SSE very challenging for experimental and theoretical studies alike. Doping also influences the thermodynamic stability of the conductive cubic phase through entropic stabilization of the more disordered cubic structure.

This chapter is adapted from the article [97] published in the journal Physical Review Materials.

Computational methods

Classical molecular dynamics was performed using long range Coulomb interactions, short range Buckingham potentials of the form

$$U\left(R_{ij}\right) = Ae^{-\frac{R_{ij}}{\rho}} - \frac{C}{R_{ij}^{6}} \tag{3.1}$$

for all oxygen- and metal-oxygen pairs (i,j) within a cutoff distance $R_{ij} = 10$ Å, and a Dick–Overhauser core–shell model [94], defined by a shell charge, Y, a shell mass, m, and a harmonic constant k, to describe the polarization of the O atoms, as implemented in the LAMMPS [98] code for molecular dynamics simulations. The parameters for the polarization of the oxygen, *i.e.* the core-shell charge splitting, Y, and spring constant, k were fitted to the atomic polarization computed in the crystal environment at density functional theory (DFT) level of theory. The Buckingham parameters for the metal-oxygen pairs, Li−O, La−O and Zr−O, refined from the one used by Klenk *et al.* [75], and the value of the unit charge q were optimized using a fitting procedure based on first-principle data evaluated using DFT. The refinement of the parameters was carried out using a gradient based minimization of the error on the forces and energies as well as the correlation between the reference and computed forces, with the shells position being updated between every optimization step. All reference DFT calculations were carried out using the plane wave CPMD software package [99, 100]. The PBE functional and norm-conserving Goedecker pseudopotentials [101] were used in conjunction with a cutoff of 150 Ry. Only the repulsive part of the metal-oxygen pairs is considered with all other C parameters being set to 0. The parameters for the W−O pair were obtained using the same methodology by using random substitutions of Zr ions in LLZO trajectories. All parameters used for this work are listed in Table 3.1. The error on the force as well as a comparison between the equation of state of LLZO are displayed in Fig. 3.1 and 3.2.

Pair	A (eV)	ρ (Å)	C (eVÅ^6)	Charge and shell
Li−O	461.30	0.3074	-	q (e) = 0.962
La−O	4420.23	0.2980	-	
Zr−O	1269.33	0.3499	-	$m(a.u.) = 0.2$
W−O	1397.76	0.3549	-	Y (e) = −2.75
O−O	22764.30	0.1490	27.63	$k\left(\text{eVÅ}^{-2}\right) = 30.2$

Table 3.1 – Summary of the polarizable Buckingham force field used to investigate the dynamics of LLZO.

All MD simulations were carried out in the isothermal-isobaric (NPT) and canonical (NVT) ensembles, with an integration timestep of 0.25 fs, using a 2 × 2 × 2 supercell. A colored noise or generalized Langevin equation (GLE) thermostat for core-shell models [86, 87] was used to control the temperature of the system. The choice of the thermostat was motivated by non-negligible drifts observed in the energy when using the Nosé-Hoover thermostat with hypervalent ions present in the structure. The colored noise thermostat maximizes

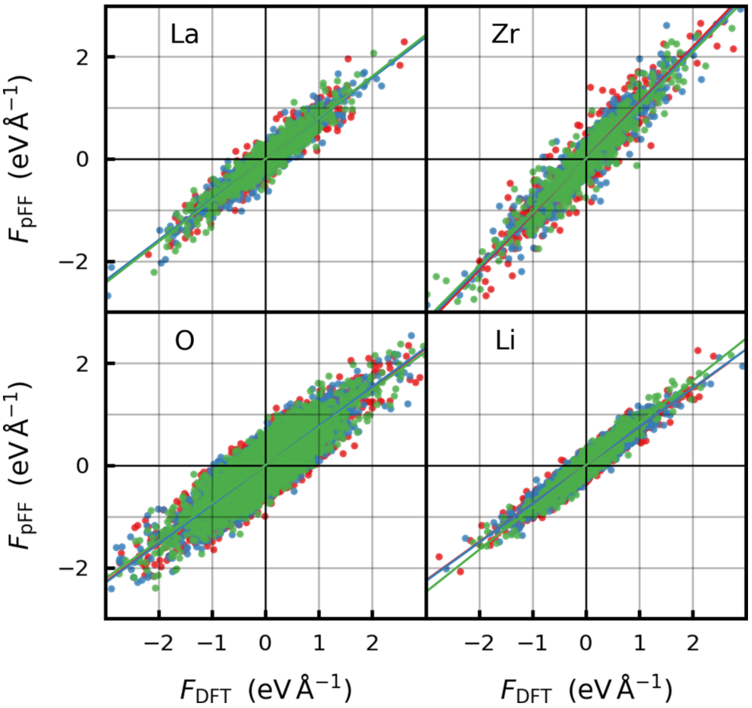

Figure 3.1 – Comparison between the DFT and force-field forces on Li, La, Zr, and O evaluated for the initial training set used for the parametrization of the force-field.

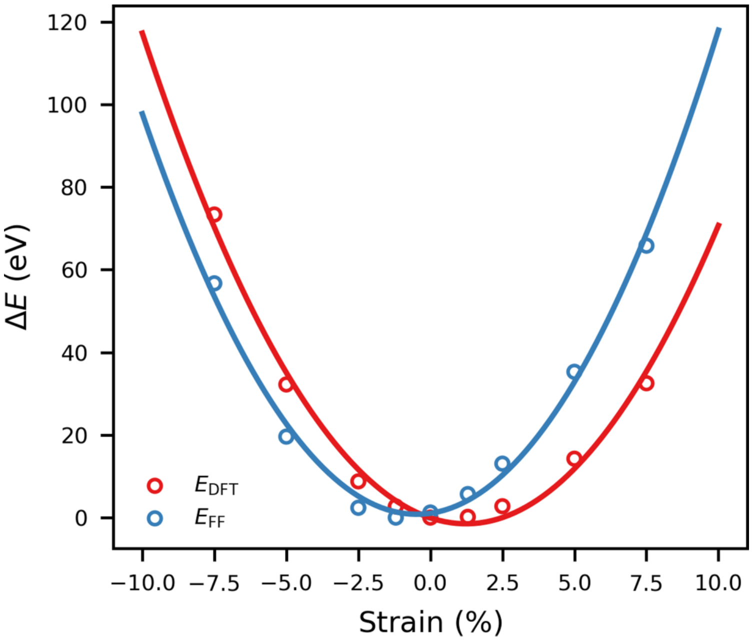

Figure 3.2 – Comparison between the reference DFT and force-field energies as a function of the strain applied to the system.

the adiabatic separation of the dynamics of the lightweight shells from the one of the ions while minimizing the impact on the shell dynamics. To account for a small energy transfer to the shells and maintain a stable dynamics over long simulation times, a zero temperature memory-less friction thermostat is coupled to the shells [86]. Fig. 3.3 shows that the use of the colored-noise thermostat as described here has only a minimal impact on the dynamical

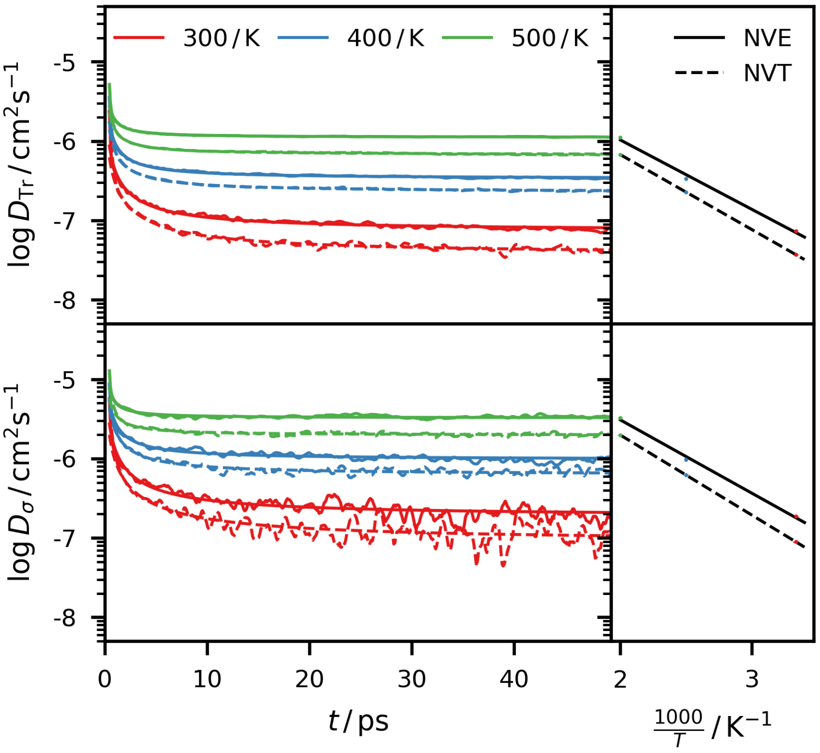

Figure 3.3 – **Left** Comparison between the NVE and NVT convergence of the charge and tracer diffusion coefficient of the Li ion with respect to the time lag in the LLWZO system with $x = 0.15$. **Right** The resulting Arhenius plots corresponding to the t^{-1} fits of the diffusion coefficient show little to no effect on the activation energy by only slightly shifting the curve up or down.

quantities of interest. In the case of the NPT simulations, a Berendsen barostat was used for the pressure control with a damping parameter of 25 ps. The phase diagrams (Fig. 3.6) were computed using temperature increments of 120 K from 200 to 1400 K, in both directions. In the temperature range where a phase transition took place, a finer sampling was performed using temperature increments of 25 K. At each temperature step, the system was equilibrated for 250 ps and statistics were collected over the subsequent 750 ps of dynamics. For the computation of the conductivity, the temperature was increased to the target temperature over 250 ps. After 250 more ps of equilibration, the positions were recorded every 0.1 ps for a duration of 4 ns. Block-averaging analysis was used to estimate the error for all the quantities computed along the trajectories. This technique relies on the division of the trajectory into long enough blocks, each block providing an independent estimate of the quantity of interest (e.g. lattice parameter, diffusion coefficient). The final error is derived from the standard error of the mean, reflecting the spread of the quantity measured throughout the different blocks [102].

Doping is used to vary the concentration of charge carriers in the structure. Each substitution introduces extra electrons/holes whose charges have to be compensated by the addition/removal of the corresponding number of Li-ions. The substitution of W^{6+} ions for Zr^{4+} ones is investigated here. To shed light on the origin of the observed changed in the material properties and identify whether they are triggered by the presence of hypervalent cations or by the change in carrier concentration, two models are compared: an *implicit* and an *explicit* doping protocol. In the *implicit* model the concentration of the charge carrier is changed without introducing the hypervalent cations. The extra charge is compensated by a positive background charge or gellium which does not influence the atomic forces during the dynamics. The *explicit* model incorporates the substitutions explicitely. Note that only the latter model is able to capture, in an approximate way, the local changes of the lithium potential energy surface due to the presence of the dopant. Comparison between the results of the two models can shed light on the different static and dynamical aspects at play in the doping of the garnet electrolytes.

The addition of a small fraction of dopants rises the issue of their distribution in the unit cell considered. This is particularly important since the position of the dopants remains frozen over the time of the simulations. This situation is reminiscent of the fixed disorder distribution in spin-glasses [103]. To account for the disorder of the dopant distribution, in addition to the block and time average, an additional average is introduced for all measured properties over a set of structures with different dopant distributions. The expectation value of an observable J therefore becomes

$$[\langle J\rangle]_{\mathrm{av}} = \sum_{\Gamma_D}\left(\sum_{R}\frac{e^{-\beta E_{\Gamma_{\mathrm{D}}}(R)}}{Z_{\Gamma_D}}J_{\Gamma_D}(R)\right)\cdot P_{\Gamma_{\mathrm{D}}}, \tag{3.2}$$

where R is the collective array of the nuclear coordinates, and Z_{Γ_D} is the partition function for a given realization of the disorder Γ_{D}, distributed with the propability $P_{\Gamma_{\mathrm{D}}}$. In the ergodic limit and using the fact that the Γ_{D} degrees of freedom are frozen

$$[\langle J\rangle]_{\mathrm{av}} = \sum_{\Gamma_D}\left(\lim_{t\to\infty}\frac{1}{t}\int_0^t J_{\Gamma_D}\left(R(t')\right)\mathrm{d}t'\right)\cdot P_{\Gamma_{\mathrm{D}}}. \tag{3.3}$$

The Boltzmann probability $P_{\Gamma_{\mathrm{D}}}$ is evaluated using a Monte-Carlo simulation in the ionic space composition [104], according to which Zr and W atoms are swapped at an effective temperature of 1200 K to mimic the dopant distribution at the usual sintering temperatures. Fig 3.4 presents the W–W radial distributions obtained for the Boltzmann distributed ionic configuration evaluated at two different doping concentrations, $x = 0.15$ and 0.25. It is important to note that the W–W pair distribution obtained from a random substitution of W ions for the Zr ones would result in a distribution overlaping the original Zr–Zr pair distribution corresponding to an undoped system. A depletion can be observed for the shortest distance pairs as a result of the increased Coulomb repulsion between the hypervalent W^{6+} ions. For the later presented results, when considering explicit doping, all reported properties are obtained averaging over an ensemble of Boltzmann-weighted structures unless otherwise stated.

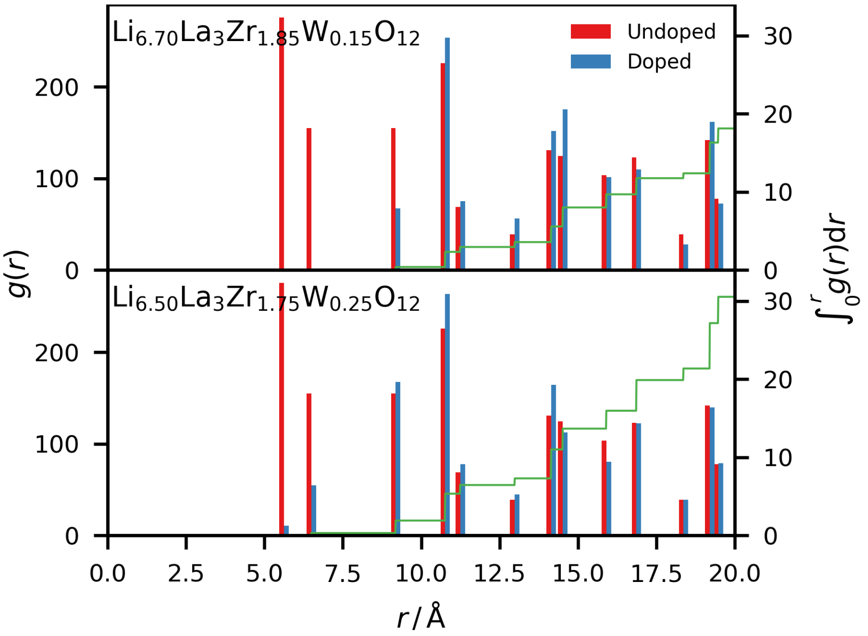

Figure 3.4 – Radial distributions of the Zr-Zr (red) and W-W (blue) pairs respectively in the undoped and Boltzmann-distributed doped structures with doping fraction $x = 0.15$ (top) and 0.25 (bottom). The shortest distance pairs are absent at low doping concentration structure due to the increased Coulomb repulsion between the hypervalent cations. Increasing the concentration saturates the structure enough that the shortest distances are forced to be occupied but longer distances remain favoured compared to the original *bcc* Zr structure. The green curve represents the integral of the W-W radial distribution function.

Results

Structure analysis

In order to assess the quality of the polarizable force-field Hamiltonian and the effects introduced by the use of the GLE thermostat, the simulation results are compared to experimental measurements, namely X-Ray diffraction (XRD) and lattice parameters measurements. In Fig. 3.5, XRD pattern computed for doped structures ($x = 0.15$) from NVT trajectories are compared to the corresponding experimental values as reported by Li *et al.* [96]. The position and amplitude of the peaks are well reproduced, despite a systematic shift. This is likely due to differences in the lattice parameters and effective charges on the atoms. Nevertheless, these first results show that the overall structure of the crystal is conserved by the model and ensure a good level of trust in the interpretation of the following simulations. Fig. 3.6 shows the

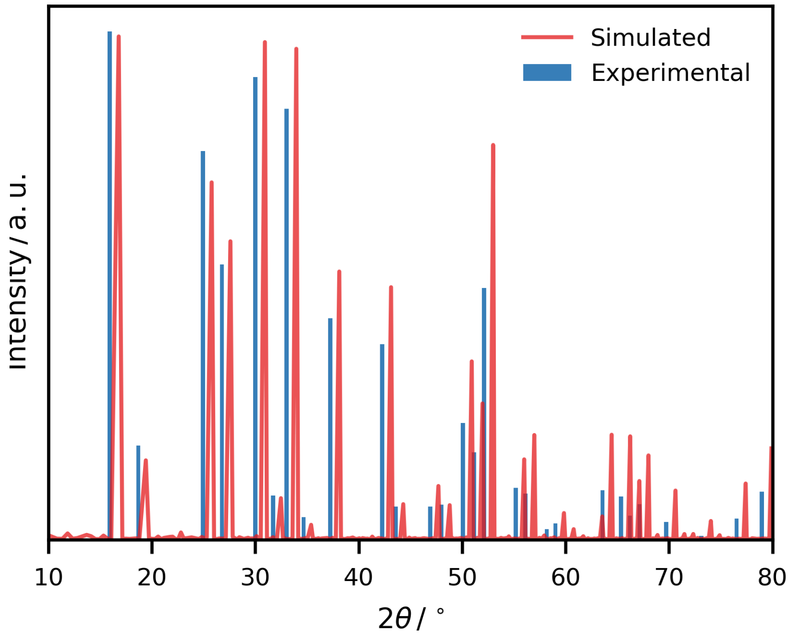

Figure 3.5 – XRD pattern of the $Li_{6.7}La_3Zr_{1.85}W_{0.15}O_{12}$ computed from the 300 K trajectories averaged over the dopant distribution. The pattern replicates the use of Cu $K\alpha$ radiation with 2θ in the range of 10 – 80°. For comparison the position and amplitude of the peaks reported by Li *et al.* [96] for the same structure are displayed.

lattice parameters obtained from the NPT simulations. In the case of the undoped system two different curves are presented, the first obtained from a heating process from 200 K upwards and the second from a cooling one from 1400 K downwards. The transition from the cubic to the tetragonal phase can clearly be observed between 800 and 900 K and is characterized by a small hysteresis. The difference between the two transition temperatures is however smaller than the temperature step used. Most importantly, in the case of the doped structures, both the implicit and explicit doping models at $x = 0.15$ are able to describe the stabilization of the cubic structure at low temperature. This suggests that the stabilization of the cubic phase induced by doping is a result of the change in the lithium concentration rather than of electrostatic effects induced by the presence of the dopant itself. This is in agreement with previous studies on the subject [78]. The model predicts quantitatively the experimental split between the lattice parameters despite a systematic shift towards smaller values. The discrepancy between the simulation and experimental measurement (as well as previously reported simulations [75, 76]) may be associated with the different force-field parametrization and with the use of the colored noise thermostat in the simulations.

Fig. 3.7 shows the radial distribution functions for the Zr-Li and W-Li pairs at various temperatures and their integrals for a doping of $x = 0.15$. The first coordination shell is well defined

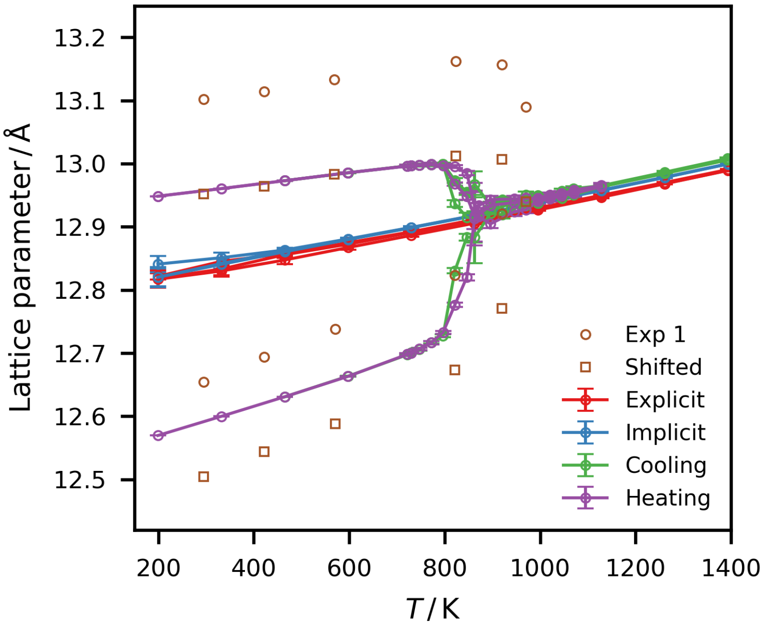

Figure 3.6 – Lattice parameters as a function of the temperature for an undoped structure (**green** and **purple**) and doped (**blue** implicit and **red** explicit) with a doping fraction $x = 0.15$. The **brown circles** are experimental values reported by Larraz *et al.* [69]. The **brown squares** are the same experimental values shifted as to align the cubic lattice parameters. The phase transition can be observed between 800 and 900 K for the undoped structure with a small hysteresis. Both doped models succesfully stabilize the cubic structure at low temperature.

and located at the distance corresponding to the nearest two octahedral sites, respectively 2.94 and 3.13 Å. Around Zr centers, no further coordination shell is well resolved indicating a liquid like behavior or the ions. Around the W centers, the lithium density located beyond the first shell is pushed back by the higher coulombic repulsion and forms a second shell near the next-nearest octahedral sites at a distance of 4.7 Å. Fig. 3.8 shows the lithium distribution around a Zr and W center sampled during 8 ns of simulation. The changes observed in Fig 3.7 are reflected here in the depletion of the lithium at the tetrahedral sites, cutting the lithium density into six blobs centered around the octahedral sites.

Dynamics and diffusion analysis

Velocity autocorrelation functions are valuable sources of insight for characterization of the dynamics of a system. The single-particle velocity autocorrelation of the lithium ions is first considered. It is defined as

$$C_v^{\mathrm{Li}}(t) = \left[\langle \mathbf{v}_i(t_0+t)\,\mathbf{v}_i(t_0)\rangle_{i,t_0}\right]_{\mathrm{av}} \tag{3.4}$$

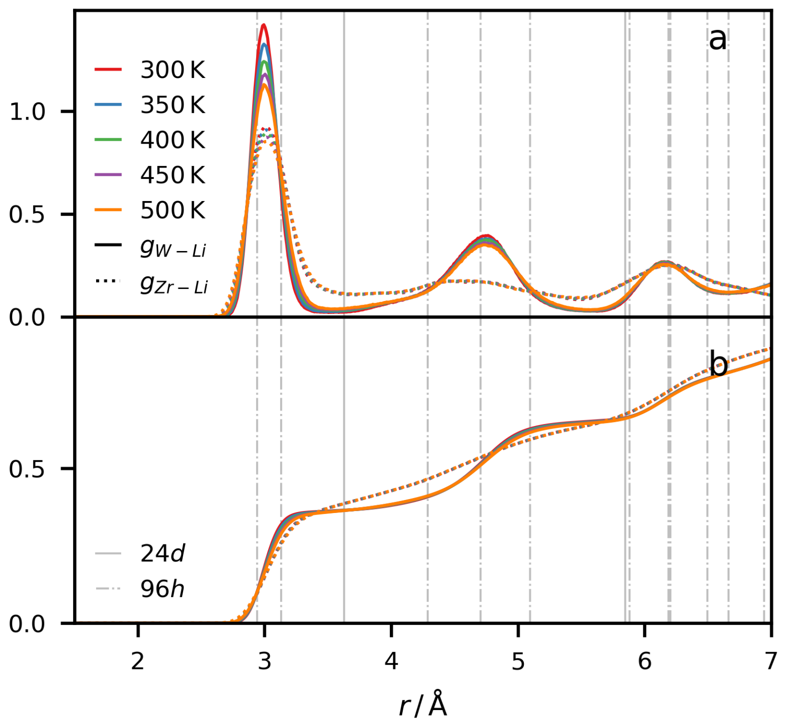

Figure 3.7 – **a)** Radial distribution function of the Li-M pairs, M = W (**solid**) and Zr (**dotted**) for $x = 0.150$ at temperatures between 300 and 500 K. The vertical lines indicate the distances to the neighboring octahedreal, 96*h*, (**dash-dotted**) and tetrahedral, 24*d*, (**solid**) crystallographic sites. **b** Integral of the radial distribution functions presented in *a*.

where $\mathbf{v}_i(t)$ is the velocity of a tagged lithium i at time t and brackets $\langle \cdot \rangle_X$ are used to represent the averaging over the variable X. Note that by ergodicity the average over the initial time, t_0, is equivalent to an ensemble average over initial configurations. Although the autocorrelation function displays a very fast decay, order of a few picoseconds, typical of liquid systems [105] and other fast ionic conductors [106], the diffusive process is reflected in the long time tails. The velocity autocorrelation functions in the garnet material follow a power law decay of the form τ^{-a}. In the considered simulations, a value of $a = 2$ is obtained for the undoped cubic structure and the explicitely doped material, and $a = 3$ for the implicitely doped one. This difference in the kinetics between the explicit and implicit model can be explained by the introduction of the hypervalent W^{6+} cations in the explicit models introducing new obstacles constraining the motion of the charge carriers, since the decrease of the carrier concentration is identical. These observation are in line with the effect of the W centers on the lithium distribution in Fig. 3.7 and 3.8. The Fourier transform of $C_v^{\mathrm{Li}}(t)$, *i.e.* the Li power spectrum, $C^{\mathrm{Li}}(\omega)$, shows two very broad peaks at frequencies of 130 and 270 cm^{-1} for the explicitly doped system. The peaks can be connected to the presence of the two nonequivalent lithium sites in the structure (see Fig. 1.6).

Central to the analysis of the dynamical effects of doping is the calculation and comparison of the diffusion coefficients. To this end the behaviors of the charge, D_σ, and tracer diffusion

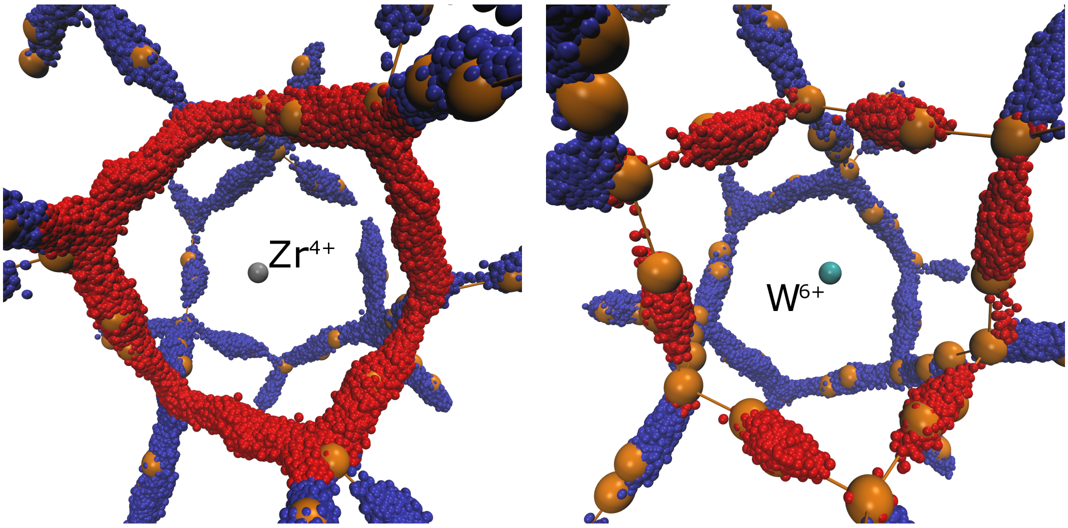

Figure 3.8 – Representation of the lithium distribution sampled during 8 ns of simulations around a central Zr (**left**) and W (**right**) ion. The lithiums are displayed in red when within a 3.75 Å distance of the central atom and blue otherwise. The sites of the crystallographic structures are overlaid in orange. The figure illustrates the depletion in lithium density around the tetrahedral sites already observed in Fig. 3.7 ($r = 3.6$Å).

coefficients, D_{Tr} are compared. Both quantities can be estimated by the derivative of the long time limit of the mean-squared displacements of, respectively, the center of mass of the particles and the particles,

$$D_\sigma = \left[\lim_{t\to\infty} \frac{N_{\mathrm{Li}}}{6}\frac{\partial}{\partial t}\left\langle \left|\langle \mathbf{x}_i(t_0+t)\rangle_i - \langle \mathbf{x}_i(t_0)\rangle_i\right|^2\right\rangle_{t_0}\right]_{\mathrm{av}} \tag{3.5}$$

$$D_{\mathrm{Tr}} = \left[\lim_{t\to\infty} \frac{1}{6}\frac{\partial}{\partial t}\left\langle \left|\mathbf{x}_i(t_0+t) - \mathbf{x}_i(t_0)\right|^2\right\rangle_{i,t_0}\right]_{\mathrm{av}} \tag{3.6}$$

with N_{Li} the number of Li ions in the simulation cell and $\mathbf{x}_i(t)$ the position of the Li ion i at time t. In particular, D_σ is directly proportional to the ionic conductivity [106]. The polynomial decay of the velocity autocorrelation function leads to a slow-down of the convergence of both the charge and particles mean square displacements used in the evaluation of the transport coefficients. The derivative of the mean square displacement can successfully be fitted to a $D_\infty + ct^{-(a-1)}$ function that can be used to evaluate the asymptotic values of the diffusion coefficients.

When performing explicit doping, large variations of the measured diffusion coefficients can be observed as a function of the dopant distribution. This effect is particularly strong at low temperatures. The convergence of the diffusion coefficient as a function of the dopant distribution is evaluated in the following way. Starting from an ensemble of 50 Boltzmann distributed dopant configurations, 50 independent trajectories were simulated and the corresponding charge diffusion coefficients, $D_{\sigma,i}$ with $i = 1,\ldots 50$ (using Eq. 3.5) computed. The average over these values is taken as the reference diffusion coefficient $D_{\sigma,\infty} = \langle D_{\sigma,i}\rangle_i$. To estimate the

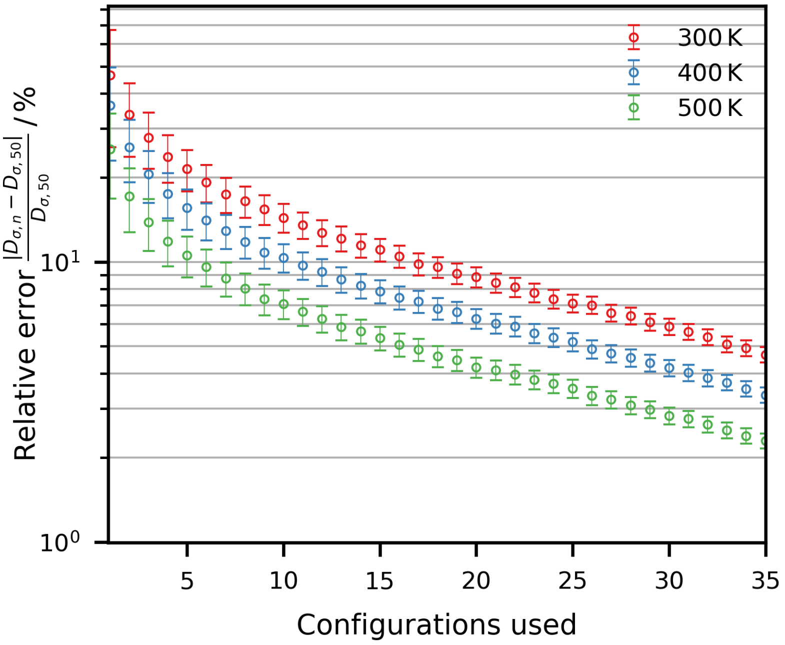

Figure 3.9 – Relative error of $D_{\sigma,n}$, the estimator of the charge diffusion coefficient using a subset of n structures of formula $\mathrm{Li_{6.5}La_3Zr_{1.75}W_{0.25}O_{12}}$, with respect to $D_{\sigma,50}$, used as an estimate of $D_{\sigma,\infty}$ at 300, 400 and 500 K.

convergence as a function of the number of dopant configurations k, the diffusion coefficients within N_k subsets of trajectories were averaged: $D^{(2)}_{\sigma,I}$ to $D^{(49)}_{\sigma,I}$, where $D^{(k)}_{\sigma,I}$, with $I = 1, \ldots N_k$, is an average diffusion coefficient computed using k trajectories sampled from the initial pool of 50 trajectories. Since the number of possible combinations grows extremely fast as $\binom{50}{k} = \frac{50!}{k!(50-k)!}$, a cutoff is applied to N_k ($N_k \leq 10000$). The relative error for the estimated diffusion coefficients (as compared to $D_{\sigma,\infty}$) is then defined as $Z^{(k)}_I = |D^{(k)}_{\sigma,I} - D_{\sigma,\infty}|/D_{\sigma,\infty}$. The corresponding mean values, $Z^{(k)} = \langle Z^{(k)}_I \rangle_I$, and standard deviations of $Z^{(k)}_I$ as a function of k are reported in Fig. 3.9. For these values to be meaningful, the error measured as the result of the dopant distribution, the *configurational noise*, must be independent and discernible from the error in the convergence of the simulations, the *sampling noise*. The sampling noise, which is the only on that needs to be considered in simulations of undoped materials [107, 102, 108] and in the implicit model, can be numerically estimated using block analysis [102] and is expected to decay with the simulation time T as $\frac{1}{\sqrt{T}}$. In the case of the doped structures used here, the sampling error can be estimated by averaging the sampling error on the diffusion coefficient of each trajectory over all dopant distribution

$$\sigma^{\mathrm{SAMP}}_{t_{\mathrm{lag}}} \equiv \left[\sigma^{\mathrm{SAMP}}_{t_{\mathrm{lag}},\Gamma_{\mathrm{D}}}\right]_{\mathrm{av}}. \tag{3.7}$$

The configurational noise on the other hand, is the average error of the diffusion coefficient,

$D_{\sigma,i}$, with respect to the reference diffusion coefficient, $D_{\sigma,\infty}$,

$$\sigma^{\mathrm{DOP}}_{t_{\mathrm{lag}}} = \left[\left|D_{\sigma,\Gamma_D} - D_{\sigma,\infty}\right|\right]_{\mathrm{av}}. \tag{3.8}$$

Fig. 3.10 shows a comparison between the configurational noise and the sampling noise

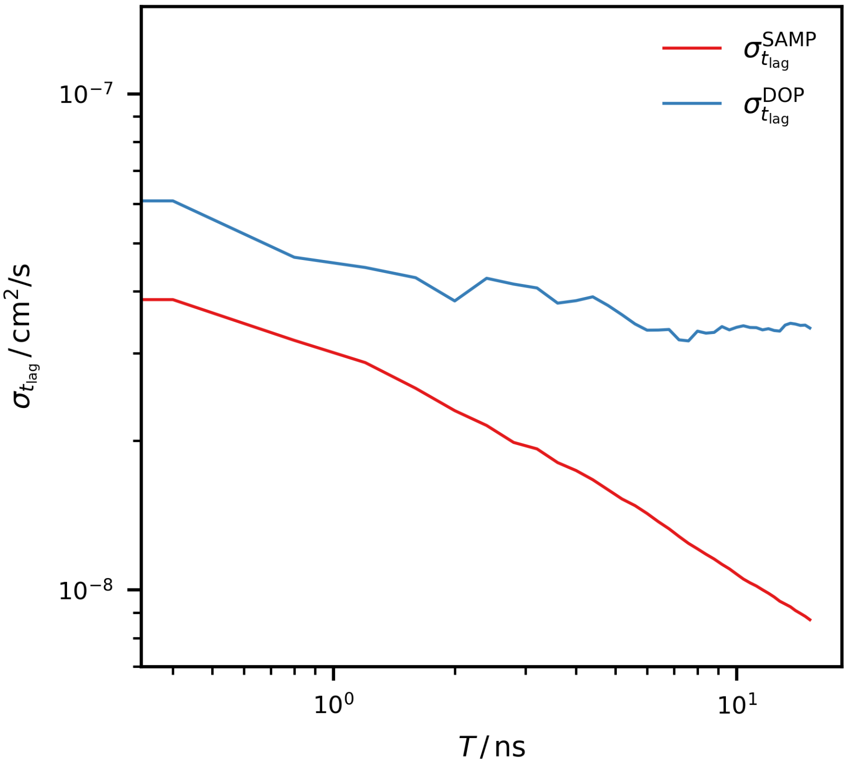

Figure 3.10 – Log-log plot of the configurational noise, $\sigma^{\mathrm{DOP}}_{t_{\mathrm{lag}}}(T)$, and of the sampling noises estimations, $\sigma^{\mathrm{SAMP}}_{t_{\mathrm{lag}}}(T)$ as a function of the simulation time T and for a lag time, t_{lag}, of 22.5 ps. A linear decay of the sampling noise can be observed, compatible with the theoretical $T^{-1/2}$ behavior. The stabilization of the estimator of the configurational noise at a much higher value shows that the simulations time T is large enough to guarantee $\sigma^{\mathrm{SAMP}}_{t_{\mathrm{lag}}}(T) \ll \sigma^{\mathrm{DOP}}_{t_{\mathrm{lag}}}$.

as a function of the simulation time T with a fixed time lag, t_{lag}. It can be observed that the simulation has reached a regime where the sampling noise decays linearly. This regime correspond to the expected theoretical $T^{-1/2}$ behavior. On the other hand, the configurational noise, $\sigma^{\mathrm{DOP}}_{t_{\mathrm{lag}}}$, has reached a plateau for the longer simulation time with $\sigma^{\mathrm{SAMP}}_{t_{\mathrm{lag}}}(T) \ll \sigma^{\mathrm{DOP}}_{t_{\mathrm{lag}}}$. Under these conditions, it is possible to estimate the configurational spread and clearly distinguish between configurational and sampling noise. These results clearly suggest that, from a statistical perspective, the average over the different dopant configurations is indeed needed in order to fully converge the results and to compare them with experiments.

Diffusion coefficients

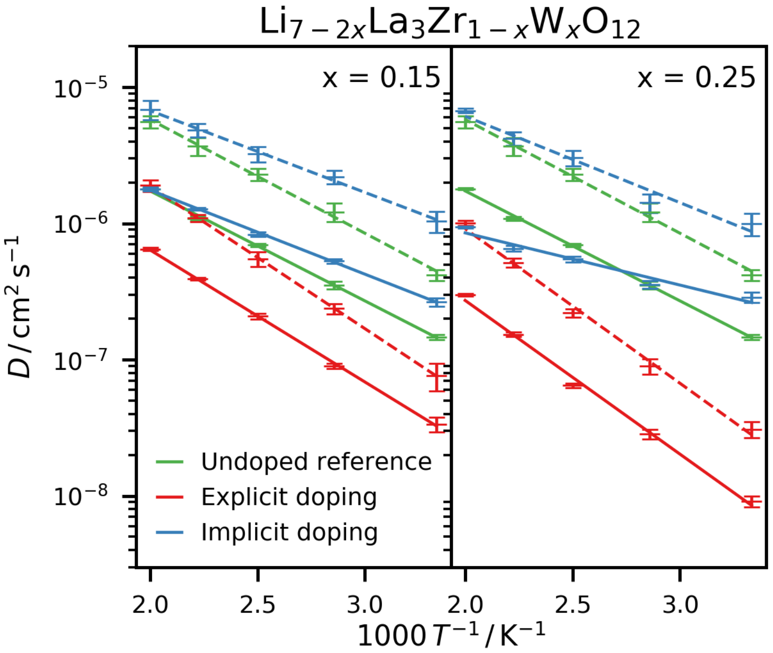

Figure 3.11 – Tracer (**solid**) and charge (**dashed**) diffusion coefficients for doping concentrations $x = 0.15$ (**left**) and $x = 0.25$ (**right**). Simulations considering explicit and implicit doping are reported and compared with ones of the cubic undoped structure. Activation energies are reported in the text.

The diffusion coefficients obtained after averaging over the dopant distributions at 300, 350, 400, 450 and 500 K are summarized in Fig. 3.11. At all temperatures the results are compatible with a linear Arrhenius behavior. For comparison, the values obtained for the undoped material constrained in the cubic geometry are also shown as a reference (green lines). The tracer diffusion coefficients, D_{Tr}, are first considered (solid lines in Fig. 3.11). The activation energy is estimated to be around 0.16 eV. However, since this structure is unstable at room temperature, it can only be compared with values extrapolated from higher temperature (900 – 1400 K) measurements. The results are in good agreement with the corresponding experimental activation energy estimated to be about 0.18 eV [70]. In the implicit scheme the values of the activation energies decrease compared to the undoped case to 0.13 ($x = 0.15$) and 0.08 eV ($x = 0.25$). The decrease in the number of charge carriers also correlates with an increase in the overall conductivity. This is most likely due to the increased number of empty sites allowing greater mobility of the ions. When considering the explicit model, the activation energies increase to 0.20 and 0.25 eV respectively, with an overall decrease in conductivity. This is coherent with the picture emerging from Fig. 3.7 and 3.8 where the hypervalent W ions displace some of the Li density around them creating obstacles to the diffusion. Compared to the experimental values of 0.44 and 0.42 eV reported by Li *et al.* [96], although the activation energy is underestimated, the model correctly yields a qualitative increase in the activation energy to values similar to those expected for Ta doping [109]. Similar observations can be made for the charge diffusion coefficients (dashed line in Fig. 3.11).

The ratio between the tracer and charge diffusion coefficients is named Haven ratio and provides information about the motion of carriers in the system [110, 111, 106, 112] . A Haven ratio, H, of 1 corresponds to uncorrelated Brownian motion, whereas lower values are an indication of coherent collective movements. Furthermore, a constant temperature Haven ratio implies an equality between the activation energies related to tracer diffusion and ionic conductivity. In LLZWO, a similar behavior to that of the thio-lisicon-type electrolyte $Li_{10}GeP_2S_{12}$ [106] is observed, displaying comparable activation energies. In the case of the undoped systems, $H \sim 0.3$ is observed, a value compatible with other recent simulation results [76, 112]. The same value is obtained for the Haven ratio of the implicitly and explicitly doped system. As discussed in Ref. [112] using nudged elastic bands (NEB) calculations, there is an understanding that diffusion events involving the simultaneous movement of different particles are much more favorable than single ion jumps. A similar conclusion can be reached considering the low value of the Haven ratio, which proves that the most probable, and therefore energetically favored, diffusion events involve a coherent particle motion. These result suggests that the same conclusion applies in the case of doped systems and therefore we can conclude that the local defects introduced by the dopant are not strong enough to decorrelate particle motion, even though they are able to change the energetics of the overall process. Only in the unphysical case of the implicit doping model can a slight decrease of H and a small temperature dependence of the Haven ratio be found, however neither of these observation change the overall interpretative picture.

Site occupancy auto-correlation function

Finally, in order to shed further light on the mechanism and dynamics of the Li diffusion in doped and undoped LLZO structures, the correlation of the occupancy of the Li sites described in Fig. 1.6 is also investigated. To this end, the set of binary variables $\sigma_I(\tau)$ associated with the occupation of a given site I at time τ (-1 when unoccupied and 1 when occupied) is mapped to the spin variables of an Ising model (down and up). The autocorrelation function is then averaged over the different realizations of the dopant distribution, as done in spin glass theory. For a single realization, the autocorrelation function is defined as

$$C_\sigma(t) = \left\langle \langle \sigma_I(t_0)\sigma_I(t_0+t)\rangle_{t_0} - \langle \sigma_I(t_0)\rangle^2_{t_0} \right\rangle_I \qquad (3.9)$$

where $\sigma_I(\tau)$ is, as previously defined, the instantaneous occupancy of the site I with value in $\{-1, 1\}$ and $\langle \sigma_I(t_0)\rangle_{t_0}$ corresponds to the time averaged occupancy of the site I and defines the initial departure from 1 at $t = 0$.

The calculation of the site occupancies was done using the following algorithm. The tetrahedral sites are first defined as the center of mass of the four oxygen atoms coordinating the sites. Each Li-ion is then assigned to either a single or a pair of tetrahedral sites using a distance cutoff of 3.1 Å. The ions assigned to pairs correspond to the ones occupying an Li3 octahedral site located between the two considered tetrahedral sites [1]

At $t = 0$, the auto-correlation function is equal to

$$C_\sigma(0) = \left\langle 1 - \langle \sigma_I(t_0) \rangle_{t_0}^2 \right\rangle_I \tag{3.10}$$

It is to be noted that this site occupancy does not correspond to the one reported in crystallographic measurements since (*i*) the occupancy of an empty site is set to -1 rather than to 0 and (*ii*) the number of crystallographic sites does not match the one resulting from the assignment methods where octahedral sites are degenerate.

In Fig. 3.12 is reported the disorder-averaged autocorrelation curves $[C_\sigma(t)]_{\text{av}}$ computed for the undoped model, the implicit doping model with $x = 0.15$ and the explicit doping model with different doping fractions ($x = 0.15$ and 0.25) at three temperatures: 300, 400 and 500 K. The curves are presented averaged over all sites (global) and resolved into partial-averages over tetrahedral and octahedral sites.

The autocorrelation functions show two distinct decay processes. The first one is extremely fast with a characteristic time of a few picoseconds and can be successfully fitted with a power law decay that takes the autocorrelation function to a plateau $c(t) = q_d$. The second process is much slower and fixes the time scale of the long time decay. This process shows a stronger temperature dependence and is best fitted with an exponential decay, typical of an ergodic diffusive behaviour [113]. The two regimes can be summarized as follows:

$$\begin{aligned} c(t) &\approx q_d + c_a\, t^{-a} \quad &&\text{for} \quad c(t) > q_d\,, \\ c(t) &\approx c_\beta\, e^{-\beta t} \quad &&\text{for} \quad c(t) < q_d\,. \end{aligned} \tag{3.11}$$

The parameters of the fits for the first and second decays, a and β respectively, are given in Table 3.2 and show interesting trends as a function of the dopant concentration.

Doping	a			β / ps^{-1}		
fraction	300 K	400 K	500 K	300 K	400 K	500 K
$x = 0$	1.015	0.673	0.514	0.011	0.058	0.139
$x = 0.15$	1.403	1.139	0.960	0.006	0.031	0.102
$x = 0.25$	1.882	1.469	1.157	0.002	0.004	0.017
$x = 0.15$	0.861	0.744	0.647	0.020	0.047	0.116

Table 3.2 – Fitting of the autocorrelation function of the site occupancies (Fig. 3.12) according to the model in Eq. 3.11. The first three lines report results for the explicit doping scheme, while the last one refers to the implicit doping model.

The decay associated with the first process occurs on too fast a time-scale for it to be associated

---

[1] This method is not able to resolve the two individual octahedral sites. However, because of the close proximity of the two sites, the probability of them both being occupied is extremely low. This shortcoming is therefore not an issue.

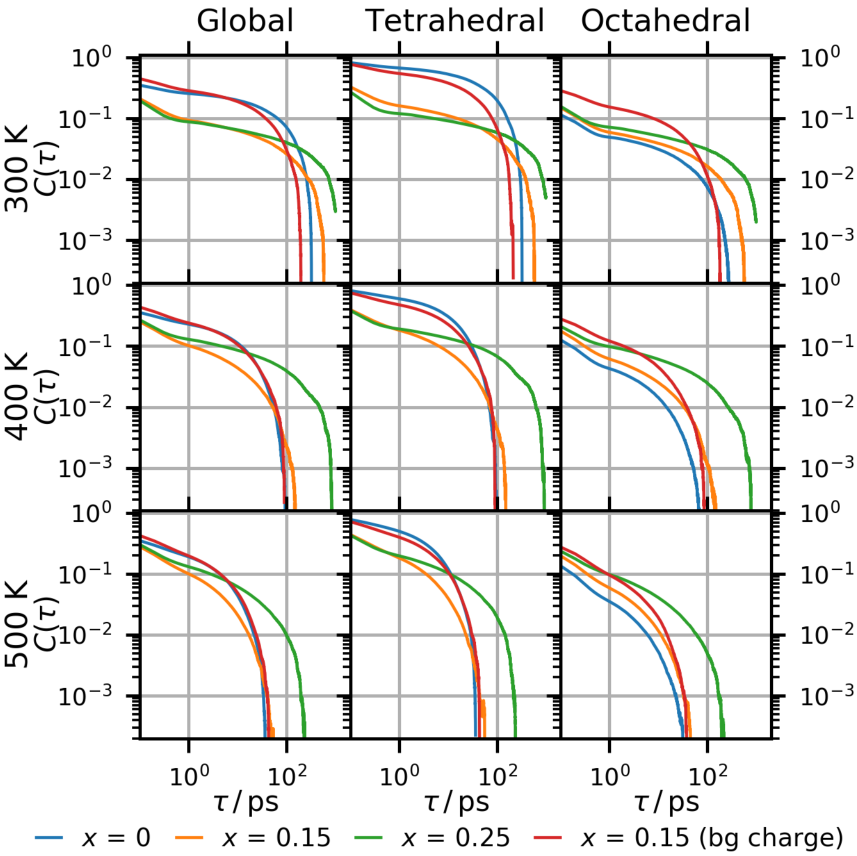

Figure 3.12 – Global and site-type resolved autocorrelation functions of the site occupancy σ_i at 300 K, 400 K and 500 K for the undoped (**blue**), $x = 0.15$ (**orange**) and $x = 0.25$ (**green**) explicit doping, and $x = 0.15$ (**red**) implicit doping.

with the diffusive motion of the Li ions. It is better interpreted as the result of a fast non-diffusive scattering of the lithium ions around the different sites. In the explicit doping model, the increment of the dopant concentration correlates with an increase of the decay rate of the first process. This accelerated decay of the site occupacy correlation is consistent with increased scattering of the trapped lithium ions around the octahedral sites described in Fig. 3.7 and 3.8. This interpretation is further supported by the fact that the change in carrier concentration alone cannot account for the increased decay rate as the implicit model displays an opposite trend. The second, exponential decay of the autocorrelation function is instead related to the long scale diffusive process. Its dependence on doping concentration and doping scheme is coherent with the behavior observed for the diffusion coefficient and ionic conductivity as presented in Fig. 3.11. The implicit doping facilitates the long time diffusion by decreasing the cluttering through lowering of the concentration of charge carriers, leading to the faster decay of the autocorrelation function. Similarly to the first process, the trend is reversed in the explicit model where the correlation time is increased by the presence of the dopant hindering the diffusive process. These observations are coherent with the change similarly observed in the velocity autocorrelation function.

Conclusion

The thermodynamic and kinetic properties of doped LLZO were investigated in this chapter by means of molecular dynamics simulations based on an ab-initio parametrized polarizable force-field.

The results show that the overall quality of the force-field description is particularly good at characterizing both the thermodynamic and kinetic aspects of the diffusion process in LLZO. This was achieved despite some discrepancies observed during the direct comparison of the activation energies of the doped systems with experimental data [114, 96]. While experiments point towards activation energies around 0.45 eV, close to the activation energy of the undoped tetragonal phase, values between 0.20 and 0.25 eV are observed, closer to the high temperature experimental activation energy of the cubic phase. However, a word of caution is always needed when directly comparing simulations to experiments. In fact, while real materials are composed by nanostructures arranged in a disordered array, the simulations deal with perfectly periodic systems with no grain boundaries. In addition, the extraction of activation energies from experimental data also requires the use of models and therefore it cannot be unequivocally compared to the outcome of the simulations. The aim of this chapter is a qualitative understanding of the different trends associated with the increase of the dopants concentration, namely W ions and the isolation of the different contributions by means of specific analysis tools and theoretical ‘experiments’, e.g. the use of explicit versus implicit doping models. Despite the above mentioned discrepancies, the overall experimental trends are confirmed by the simulations.

The first observation is the fact that the distribution of the W dopant atoms affects the efficiency of the charge transport process. For this reason, in addition to the canonical ensemble average, it is critical to consider the use of an average over different realizations of the dopants distribution using an approach derived from spin glass theory. Overall, the results lead to the identification of two main effects induced by the introduction of the dopant, significantly affecting the conductivity of LLZO. The first is of a thermodynamic nature and relates to the stabilization of the conducting cubic phase at lower temperatures, which can clearly be identified as an effect of the lowering of the concentration of the charge carriers exclusively. The second, kinetic, is affected by both the change in the concentration of the carrier and the local modification of the potential energy landscape felt by the Li ions. The first contribution is isolated through the use of the implicit model, smearing the additional positive charge of the dopant uniformly over the entire simulation box. The analysis of the conductivity reveals a substantial decrease of the activation energy compared to the reference one, namely the undoped structure. This shows that the decrease of the Li concentration induced by doping results in the decongestion of the network of channels allowing a higher mobility of the Li. In addition, when considering the nature of the defects induced by the hypervalent dopants (W centers in the explicit model), the additional coulombic repulsion promotes further scattering of the Li ions, causing an overall decrease of the conductivity and an increase of the activation energy, similar to the proton trapping effect in hydrogen conductors [115, 116]. This is also evident from the analysis of the Li ions distribution around the dopants, which shows a depletion after the first coordination shell associated with the breaking of the Li "wire" (Fig. 3.7 and 3.8). Interestingly, the analysis of the autocorrelation functions of the site occupancies (Fig. 3.12) confirms that the long term diffusive process slows down considerably as a result of the scattering W centers whereas the short time oscillation between neighboring sites is in general accelerated by the presence of the dopant.

In conclusion, the atomistic simulations reveal a very complex behavior of the LLZO conductivity as a function of the dopant concentration. While a quantitative description of the diffusion process is probably still beyond the capabilities of the model, the approach is nonetheless able to capture the different trends due to both temperature and dopant concentration. This offers valuable insights into the interplay between thermodynamic phase stabilization and kinetic slow down mechanisms happening in the doped systems.

4 Molecular Dynamics based Force-Field Parametrization

Introduction

The accuracy of any force-field based molecular dynamics simulation is completely reliant on the quality of the parameters used in the force-field. The parametrization of these parameters is therefore a critical first step to obtain reliable results. Initial efforts to parametrize force-fields relied heavily on the use of experimental data [117, 118]. Such training not only relies on molecular or crystal structure but also benefit from information about the curvature of the potential energy surface around the equilibrium, information that can be provided through various quantities such as the elastic constant, bulk moduli, piezoelectric constants or phonon frequencies in solid-state structures. The development of first principle methods and the lowering of their cost has then led to an increased amount of data being available for the purpose of parametrization. Consequently force-matching algorithm [119] quickly took advantage of this trove of data and took the spotlight. The use of computed references provide an advantage as they not only increase the amount of reference data available for fitting but also provide access to structures that have not yet been synthesized or characterized experimentally.

The fitting of a force-field is based on the minimization of a cost function defined for the system. The most commonly used form of cost function is the sum of square error on the system observables:

$$\mathcal{C} = \sum_{i}^{N} \omega_i \, |x_i - X_i|^2 \tag{4.1}$$

where x_i is an observable quantity, X_i is the respective reference value, ω_i is the weight of the contribution of observable x_i and the sum is made over all observable quantities i in the system. When fitting parameters to first principles data, the most commonly used observables are the forces and the energy. One can isolate the different components of the loss function based on the type of observable considered

$$\mathcal{C} = \omega_F \mathcal{C}_F + \omega_E \mathcal{C}_E \tag{4.2}$$

where ω_F, ω_E and $\mathcal{C}_F$, $\mathcal{C}_E$, are respectively the weights and loss functions relative to the atomic forces and the system potential energy. Eq. 4.1 cannot always be used as such as direct comparison between observable and reference is not always possible. When considering the potential energy of a system, the relative values of the different configurations of the systems are what matters and therefore only relative measurements can be compared. One way to do so is to compare the difference in energy between the different structures used in the training set. A normalization factor can also be introduced.

$$\mathcal{C}_E = \frac{\sum_{i,j}^{N} \left|(\epsilon_i - \epsilon_j) - (E_i - E_j)\right|^2}{\sum_{i,j}^{N} \left|E_i - E_j\right|^2} \tag{4.3}$$

where ϵ_i and E_i are the force-field and reference first-principle energies derived for the structure i and the sum is done over all pairs of structures.

Alternatively, forces can be directly compared as they correspond to the derivative of the potential with respect to the individual positions. A similar normalization factor can be introduced to reduce the difference in amplitude between the different parts of the cost function

$$\mathcal{C}_F = \frac{\sum_{i}^{N} |\mathbf{f}_i - \mathbf{F}_i|^2}{\sum_{i}^{N} |\mathbf{F}_i|^2} \tag{4.4}$$

Other measures of the fitness of the parameters can be used, such as the alignment of the reference and calculated forces [120]. This can be measured by calculating the correlation coefficient $\mathcal{C}_C$,

$$\mathcal{C}_C = \frac{\sum_i \mathbf{f}_i \cdot \mathbf{F}_i}{\sqrt{\sum_i |\mathbf{f}_i|^2}\sqrt{\sum_i |\mathbf{F}_i|^2}} \tag{4.5}$$

where f_i and F_i are the computed and reference forces on atom i.

Atomic polarization

A particular difficulty of the fitting a polarizable force-field to first principle data is the the absence of correspondence between the shells of the core-shell model and any objects in the reference first-principle structure. The exact position at which the shells should be located is therefore initially unknown. Past attempts have initially tried to fit polarizable force-fields while fixing the shells on top of the cores. These attemps have however resulted in potentials tuned to minimize the polarization of the system by minimizing the shell displacements. Current solution to the problem are to update the positions of the shell during the fit. Two schemes have been used to this effect. The first one optimize the position of the shells before each evaluation of the cost function. The second approach, named *simultaneous fitting*, considers the coordinates of each shells extra parameters added to the optimization. The shell position being optimized as the fitting procedure proceeds.

State-of-the-art methodologies

Two tools have come up as state-of-the-art for the derivation of forces fields: the General Utility Lattice Program (GULP) and DFTFIT.

Developed in the group of Prof. J. Gale in Curtin University, the General Utility Lattice Program (GULP) [121, 122, 123] is a tool used to perform a variety of types of simulation on molecules and materials. GULP includes a wide range of potentials and the option to fit them to a variety of observables, including energy, stress, forces and many other experimental properties. Though GULP uses analytic derivatives of up to the second degree for the computation of the forces and properties, the software relies on numerical derivatives for the optimization of the force-field parameters. GULP fully support the use and training of core-shell model and implements the simultaneous fitting of the force-field and shell positions.

DFTFIT is a python based fitting library leveraging Lammps to allow the fit of multiple potentials using DFT training data. It offers an extensive set of single- and multi-objective functions, inherited from its use of the nlopt[124] and pagmo[125] libraries. Despite the many positive aspects and the flexibility of DFTFIT, the lack of support for polarizable force-fields, limits its usefulness in this work.

Global optimization

Although GULP only present options for local optimization of the force-fields parameters, DFTFIT also provides methods for the global optimization of the parameters through the use of genetic algorithm also known as evolutionary algorithm. Evolutionary algorithm are general-purpose stochastic methods that search for the global optimum of a function. They are inspired by natural selection and evolution in biological systems. They mainly differ from other optimization methods such as Simulated Annealing [126] by conserving a population of solution to the problem rather than a single one.

Introduced in 1995 by Storn and Price [127], the Differential Evolution (DE) method is one such algorithm. Similar to Genetic Algorithms [128], they demark themselves by using arithmetic combination of individuals to generate new generations. The mutation operator of DE initially favors the exploration of the solution space. As the evolution progress, it will shift towards the exploitation of the favorable traits discovered. DE require little parameter tuning [129] while exhibiting fast convergence [130]. It has been successfully applied to a wide range of optimization problems and is generally considered reliable, accurate and robust.

The key idea of DE is for each parent $x_i(t)$ of generation t, an offspring $x'_i(t)$ is generated as follow. Three individuals $x_{i1}(t)$, $x_{i2}(t)$ and $x_{i3}(t)$ are randomly selected with $i1 \neq i2 \neq i3 \neq i$. A random integer $r \in \{1, ..., N_d\}$ is selected, with N_d the number of parameters or traits of an individual. For each trait $j = 1, ..., N_d$, let

$$x'_{i,j}(t) = \begin{cases} x_{i3,j}(t) + F\left(x_{i1,j}(t) - x_{i2,j}(t)\right), & \text{if } \mathcal{U}(0,1) < P_r \text{ or } j = r \\ x_{i,j}(t), & \text{otherwise} \end{cases} \tag{4.6}$$

where $x_{i,j}(t)$ and $x'_{i,j}(t)$ represent the j-th paremeter of the offspring, F is a positive scaling factor and P_r is the probability of reproduction. If the value of the loss function with the offspring's parameter is better than for the parent, the offspring replace the parent in the next generation, otherwise the parent remains.

Though little tuning is required, control parameters, F and P_r, still have to be selected for each problem and finding the optimal values can be time-consuming. To circumvent this issue, Omran *et al.* proposed in 2005 a *Self-adaptive* version of DE (SDE or SADE) [131].

For the self-adaptive scheme the generation of the offspring is altered in two ways. First, P_r is drawn from a normal distribution $\mathcal{N}(0.5, 0.15)$. Second, the scaling factor is now inherited from the parent generation.

$$x'_{i,j}(t) = \begin{cases} x_{i3,j}(t) + F_i(t)\left(x_{i1,j}(t) - x_{i2,j}(t)\right), & \text{if } \mathcal{U}(0,1) < \mathcal{N}(0.5, 0.15) \text{ or } j = r \\ x_{i,j}(t), & \text{otherwise} \end{cases} \tag{4.7}$$

where

$$F_i(t) = F_{i4}(t) + \mathcal{N}(0, 0.5)\left(F_{i5}(t) - F_{i6}(t)\right) \tag{4.8}$$

with $i4$, $i5$, $i6$ randomly drawn from the parent generation. The scaling factor for the initial population is again drawn from a normal distribution $\mathcal{N}(0.5, 0.15)$.

Shells and global optimization

Although the use of genetic algorithm provides a opportunity to discover parameters sets without the need to provide starting values, they create difficulties when dealing with the core shell model.

The first approach described above relies on the continuous relaxation of the shell position throughout the optimization process. However, in the case of genetic algorithm, two difficulties are introduced here. Firstly, the whole parameter population need to have its shell positions optimized, leading to the optimization of the shell positions for many "unfit" individuals. Secondly, there is no guarantee that the individuals will generate force-fields where the shell positions can be optimized quickly.

The second approach is not faring much better since adding the shell position as extra traits on the individuals dramatically increase the complexity of the optimization problem.

To account for these issues, a new methodology is proposed to deal with the shells.

As the Buckingham potentials are traditionally applied to the shells, and not to the cores, the only forces acting on the cores are the Coulombic forces and the harmonic force of the shell

$$\mathbf{f}_{\text{core}} = \mathbf{f}_{\text{Coul}} + \mathbf{f}_k \tag{4.9}$$

Rephrased, this means that the harmonic forces needed to minimize the errors on the cores are known

$$\mathbf{f}_k = \mathbf{F}_{\text{DFT}} - \mathbf{f}_{\text{Coul}} \tag{4.10}$$

The position of the shells can therefore be updated self-consistently to reduce the error on the cores to the level of accuracy needed. Given that this position should be considered as the optimal position for the shells, the goal is then to minimize the forces on the shells. This method allows the position of the shells to be fixed at the start of the optimization and reduce the complexity of the problem.

Local optimization and gradients

In the various fitting software packages available the gradients of the loss function is achieved using the finite difference method to allow for more flexibility in term of the form of the force-field and fitted observables. Although this method gives good approximate gradients and allow for a good flexibility, the resulting gradients can be noisy. However, if the fit is restricted to observables that can be derived from the energy and its first derivative, such as the forces or stress, and to a finite set of potentials, it is fairly easy to derive the analytic gradient of the loss function with respect to the various parameters at play.

Considering a force-field based on Coulomb interactions, on the interactions of Buckingham pairs potentials and by the harmonic potentials of the core-shell model. The total potential energy of a system described by this model is defined as the sum of the Coulomb, Buckingham and harmonic potentials

$$\begin{aligned} U = & U_{\text{Coul}}\left(\{\mathbf{r}_i\}, \{q_i\}\right) \\ & + U_{\text{Buck}}\left(\{\mathbf{r}_i\}, \{A_{IJ}\}, \{\rho_{IJ}\}, \{C_{IJ}\}\right) \\ & + U_{\text{Shell}}\left(\{\delta\mathbf{r}_i\}, \{k_i\}\right) \end{aligned} \tag{4.11}$$

where $\mathbf{r}_i$ are the position of the atoms of the system and q_i their charge, A_{IJ}, ρ_{IJ} and C_{IJ} are the parameters of the pair of atoms i and j of respective atomic types I and J, $\delta\mathbf{r}_i$ the displacement of the shell i and k_i is the spring constant for the core-shell pair i. The gradients of the individual component can be considered with respect to the different parameters they depend on. The Buckingham contribution, U_{Buck}, is a function of the parameters of the considered pairs. On the other hand the Coulomb potential and the shell potentials, U_{Coul} and U_{Shell} can be considered together.

Buckingham gradients

The Buckingham contribution to the total gradient is defined as

$$U_{\text{Buck}}\left(\{\mathbf{r}_i\},\{A_{IJ}\},\{\rho_{IJ}\},\{C_{IJ}\}\right) = \sum_{i,j} A_{IJ} e^{-r_{ij}/\rho_{IJ}} - \frac{C_{IJ}}{r_{ij}^6} \tag{4.12}$$

where A_{IJ}, ρ_{IJ} and C_{IJ} are the parameters of the pair of atoms i and j of respective atomic types I and J, and r_{ij} is the inter atomic distance between the two atoms i and j. The forces, the derivative of the energy with respect to the coordinates, are

$$f_{\beta,i,\text{Buck}} = -\frac{\partial}{\partial \beta_i} U_{\text{Buck}} = \sum_j \frac{\beta_i A_{IJ}}{r_{ij}\rho_{IJ}} e^{-r_{ij}/\rho_{IJ}} - \frac{6\beta_i C_{IJ}}{r_{ij}^8} \tag{4.13}$$

where β_i is one of the cartesian coordinates x, y or z of atom i.

From there, the gradients of the energy and forces with respect to the parameters A_{XY}, ρ_{XY} and C_{XY} of the potential between two atoms of types X and Y are easily derived as

$$\begin{aligned}
\frac{\partial}{\partial A_{XY}} U_{\text{Buck}} &= \sum_{i\in X, j\in Y} e^{-r_{ij}/\rho_{XY}} \\
\frac{\partial}{\partial \rho_{XY}} U_{\text{Buck}} &= \sum_{i\in X, j\in Y} \frac{A_{XY} r_{ij}}{\rho^2} e^{-r_{ij}/\rho_{XY}} \\
\frac{\partial}{\partial C_{XY}} U_{\text{Buck}} &= \sum_{i\in X, j\in Y} -\frac{1}{r_{ij}^6}
\end{aligned} \tag{4.14}$$

for the energies as defined in Eq. 4.12 and

$$\begin{aligned}
\frac{\partial}{\partial A_{XY}} f_{\beta,i,\text{Buck}} &= \sum_{j\in Y} \frac{\beta_i}{r_{ij}\rho_{IJ}} e^{-r_{ij}/\rho_{XY}} \\
\frac{\partial}{\partial \rho_{XY}} f_{\beta,i,\text{Buck}} &= \sum_{j\in Y} \frac{A_{XY}\beta_i}{r_{ij}\rho_{IJ}^3} \left(r_{ij} - \rho_{XY}\right) e^{-r_{ij}/\rho_{XY}} \\
\frac{\partial}{\partial C_{XY}} f_{\beta,i,\text{Buck}} &= \sum_{j\in Y} -\frac{6\beta_i}{r_{ij}^8}
\end{aligned} \tag{4.15}$$

for the forces defined in Eq. 4.13. Analogous formula can be defined for the original form of the Buckingham potential (Eq. 2.45)

$$
\begin{aligned}
\frac{\partial}{\partial \epsilon_{XY}} f_{\beta,i,\text{Buck}} &= \left(\frac{\partial A_{XY}}{\partial \epsilon_{XY}}\frac{\partial}{\partial A_{XY}} + \frac{\partial C_{XY}}{\partial \epsilon_{XY}}\frac{\partial}{\partial C_{XY}}\right) f_{\beta,i,\text{Buck}} \\
&= \frac{1}{\alpha_{XY}-6}\left(6e^{\alpha_{XY}}\frac{\partial}{\partial A_{XY}} + \alpha_{XY} r^6_{m,XY}\frac{\partial}{\partial C_{XY}}\right) f_{\beta,i,\text{Buck}} \\
\frac{\partial}{\partial \alpha_{XY}} f_{\beta,i,\text{Buck}} &= \left(\frac{\partial A_{XY}}{\partial \alpha_{XY}}\frac{\partial}{\partial A_{XY}} + \frac{\partial C_{XY}}{\partial \alpha_{XY}}\frac{\partial}{\partial C_{XY}} + \frac{\partial \rho_{XY}}{\partial \alpha_{XY}}\frac{\partial}{\partial \rho_{XY}}\right) f_{\beta,i,\text{Buck}} \\
&= \left(\frac{6\epsilon_{XY}\left(\alpha_{XY}-7\right)}{\left(\alpha_{XY}-6\right)}\frac{\partial}{\partial A_{XY}} + \frac{6\epsilon_{XY}}{\left(\alpha_{XY}-6\right)^2} r^6_{m,XY}\frac{\partial}{\partial C_{XY}} - \frac{r_m}{\alpha^2_{XY}}\frac{\partial}{\partial \rho_{XY}}\right) f_{\beta,i,\text{Buck}} \\
\frac{\partial}{\partial r_{m,XY}} f_{\beta,i,\text{Buck}} &= \left(\frac{\partial rho_{XY}}{\partial r_{m,XY}}\frac{\partial}{\partial rho_{XY}} + \frac{\partial C_{XY}}{\partial r_{m,XY}}\frac{\partial}{\partial C_{XY}}\right) f_{\beta,i,\text{Buck}} \\
&= \left(\frac{1}{\alpha_{XY}}\frac{\partial}{\partial rho_{XY}} + \frac{6\alpha_{XY}\epsilon_{XY}}{\alpha_{XY}-6} r^5_{m,XY}\frac{\partial}{\partial C_{XY}}\right) f_{\beta,i,\text{Buck}}
\end{aligned}
\tag{4.16}
$$

The derivatives of the different components of the loss functions with respect to the Buckingham parameter χ are then defined as

$$
\begin{aligned}
\frac{\partial}{\partial \chi}\mathcal{C}_E &= \frac{2}{N_\text{S}}\sum_{I,J}^{N_\text{S}}\left|\left(\epsilon_I-\epsilon_J\right)-\left(E_I-E_J\right)\right|\left(\frac{\partial}{\partial \chi}\epsilon_{I,\text{Buck}} - \frac{\partial}{\partial \chi}\epsilon_{J,\text{Buck}}\right) \\
\frac{\partial}{\partial \chi}\mathcal{C}_F &= \frac{2}{N_\text{F}}\sum_{i}^{N_\text{F}}\left|\mathbf{f}_i-\mathbf{F}_i\right|\cdot\frac{\partial}{\partial \chi}\mathbf{f}_{i,\text{Buck}} \\
\frac{\partial}{\partial \chi}\mathcal{C}_F &= \frac{1}{\sqrt{\sum_i|\mathbf{F}_i|^2\sum_i|\mathbf{f}_i|^2}}\left[\sqrt{\sum_i|\mathbf{f}_i|^2}\left(\sum_i \mathbf{F}_i\cdot\frac{\partial}{\partial \chi}\mathbf{f}_i\right) - \left(\sum_i \mathbf{f}_i\cdot\mathbf{F}_i\right)\frac{\sum_i \mathbf{f}_i\cdot\frac{\partial}{\partial \chi}\mathbf{f}_i}{\sqrt{\sum_i|\mathbf{f}_i|^2}}\right]
\end{aligned}
\tag{4.17}
$$

These derivatives can then be used in the analytic derivative of the loss function.

Coulomb and Core-Shell gradients

The unit charge $\hat{q}$, is introduced as a parameter of the system. The charge of any species in the system is then define as the product between this unit charge and the oxidation state of the species, $q_\text{X} = \hat{q} n_\text{X}$. This formulation is convenient to consider the Coulomb potential and forces since $\hat{q}$ can be isolated from the rest of the equations:

$$
U_\text{Coul}\left(\hat{q}\right) = \hat{q}^2 U_\text{Coul}(1) \tag{4.18}
$$

and

$$
\mathbf{f}_{\text{Coul},i}\left(\hat{q}\right) = \hat{q}^2 \mathbf{f}_{\text{Coul},i}(1) \tag{4.19}
$$

where $U_\text{Coul}(1)$ and $f_{\text{Coul},i}(1)$ represent the potential and forces with a unit charge of 1. The scaling of the shell charge however has an adverse effect on polarization. In Eq. 2.51, we defined the polarization, as a function of the shell charge. To keep the polarizability of the core-shell model constant, the spring constant of the model must be adapted as well:

$$k\left(\hat{q}\right) = \hat{q}^2 \frac{(ne)^2}{\alpha} = \hat{q}^2 k\,(1) \tag{4.20}$$

where n is the shell oxidation state, α the polarizability of the modeled ion and $k\,(1)$ is the spring constant defined for a unit charge of 1. The resulting potential and forces are

$$U_{\text{Shell}}\left(\hat{q}\right) = \sum_i \frac{\hat{q}^2}{2} k_i\,(1)\,|\delta\mathbf{r}_i|^2 = \hat{q}^2 U_{\text{Shell}}\,(1) \tag{4.21}$$

and

$$\mathbf{f}_{\text{Shell},i}\left(\hat{q}\right) = -\hat{q}^2 k_i\,(1)\,\delta\mathbf{r}_i = \hat{q}^2 \mathbf{f}_{\text{Shell},i}\,(1)\,. \tag{4.22}$$

The derivative of the total potential depending on the unit charge and its derivatives can then easily be derived as

$$\frac{\partial}{\partial\hat{q}} U = 2\hat{q}(U_{\text{Coul}}\,(1) + U_{\text{Shell}}\,(1)) \tag{4.23}$$

and

$$\frac{\partial}{\partial\hat{q}} \mathbf{f}_i = 2\hat{q}(\mathbf{f}_{\text{Coul},i}\,(1) + \mathbf{f}_{\text{Shell},i}\,(1)). \tag{4.24}$$

Regularization

Due to the use of the second formulation of the Buckingham potential introduced in Eq. 2.47

$$U\left(R_{ij}\right) = Ae^{-\frac{R_{ij}}{\rho}} - \frac{C}{R_{ij}^6}, \tag{4.25}$$

and the decoupling of the repulsive part from the attractive one, it is possible to derive potentials which are unbound, without barriers. This is particularly likely if the information concerning shorter distances is lacking in the training set. As a consequence, the dynamics can become unstable with shells being affected by large forces leading in their ejection far from their cores. In order to prevent this behavior, a regularization of the optimization can be introduced to guarantee the presence of a sufficiently repulsive barrier in the fitted potentials.

One such regularization scheme can achieved by enforcing a specific minimum barrier for the pair potentials. By defining ΔU as the difference between the potential value at the top of the barrier and the minimum potential value after the barrier, as shown in Fig. 4.1. The constraint

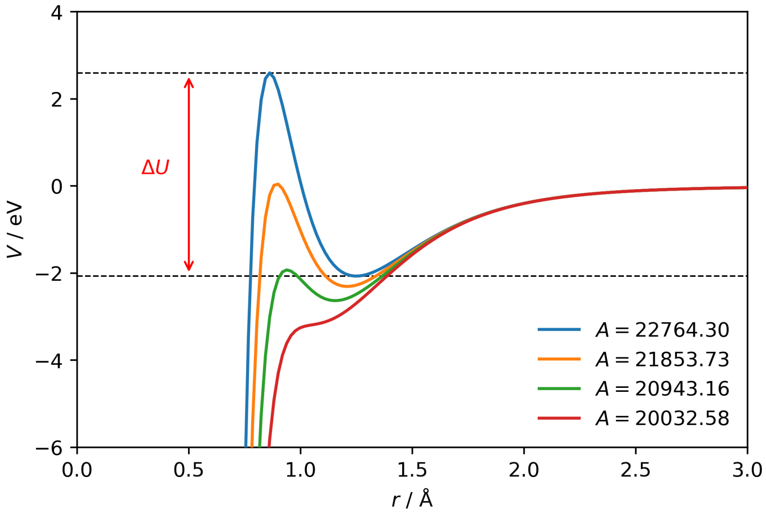

Figure 4.1 – With small variations of the A parameter, the repulsive barrier of the O−O Buckingham pair used in Chap. 4 vanishes and result in a purely attractive potential. The barrier ΔU is shown for the initial parameters.

becomes

$$\mathcal{C}_R = \begin{cases} K, & \text{if } \Delta\mathcal{U} < \Delta U_{\text{min}} \\ 0, & \text{otherwise} \end{cases} \tag{4.26}$$

where K is the penalty. The constraint will penalize individuals with too low or nonexistent barriers. This approach works very well with global optimization methods but lacks a proper gradient for its use in local optimization. This can be circumvented by replacing the step by a function with a define derivative such as the hyperbolic tangent

$$\mathcal{C}_R = \frac{K}{2}\left(1 + \tanh\left(\alpha\left(\Delta U - \Delta U_{\text{min}}\right)\right)\right) \tag{4.27}$$

where the α parameter controls the width of the step.

Computational methods

The fitting of a force-field for lithium tantalum oxide was used to investigate the efficiency of the methodology. The force-field comprises three pair potentials: Li-, Ta- and O-O. A core-shell model is used to represent the oxygen atoms. The loss function

$$\mathcal{C} = \omega_E \mathcal{C}_E + \omega_F \mathcal{C}_F - \omega_C \mathcal{C}_F \tag{4.28}$$

is initially optimized using the *Self-adaptive Differential Evolution* algorithm implemented in the pygmo [125] library. The initial population is made of 100 individuals randomly drawn from the parameter spaces listed in Table 4.1. Because the optimization of the position of the shells with random parameters is problematic, the cost function is computed with shells placed in their *idealized* position, minimizing the error on the forces applied to the oxygen cores. The fitting is performed on three phases of lithium tantalate. Each phase is represented by 80 structures drawn from a DFT trajectory at regular intervals.

	Li-O		Ta-O		O-O	
	Min	Max	Min	Max	Min	Max
A	0.00	10000.00	0.00	10000.00	0.00	30000.00
ρ	0.05	1.00	0.05	1.00	0.05	1.00
C	0.00	25.00	0.00	25.00	0.00	50.00

Table 4.1 – Parameter space used for the initial global optimization of the lithium tantalate force-field.

The best individuals obtained in the first global optimization step are then optimized locally using the low-storage BFGS implementation of NLopt [124]. The computation of the gradients for the local optimization is achieved using the analytic gradients of the energy and forces as defined in 4.14 and 4.15. These were implemented for the Buckingham pair styles in LAMMPS as a compute.

It is important to note that the error on the forces of the cores will increase with the variation of the unit charge parameter. Assuming that the position was optimized using a unit charge q_0, the error on the forces is defined as

$$\Delta \mathbf{f}_i \left(q\right) = \left(q^2 - q_0^2\right) \mathbf{f}_i \left(1\right). \tag{4.29}$$

If the mean error on the shells becomes greater than that on the other species, the position of the shells should be updated to better fit the current state of the force-field.

To assess the validity of the gradients, the comparison between the numerical and analytic gradients is made. Fig. 4.2 shows the atomic forces on one of the oxygen atoms of the training, and the respective numeric and analytic derivatives with respect to each parameter. The advantage of using analytic derivatives is particularly visible when considering the derivative with respect to ρ where the amplitude of the noise is highest in the numeric gradient. Similarly, Fig. 4.3 shows the loss function for the forces, $\mathcal{C}_F$, and its derivative, as defined in Eq. 4.4 and 4.17 respectively, the noise observed in the derivative of the forces is propagated to the numerical derivative of the loss function.

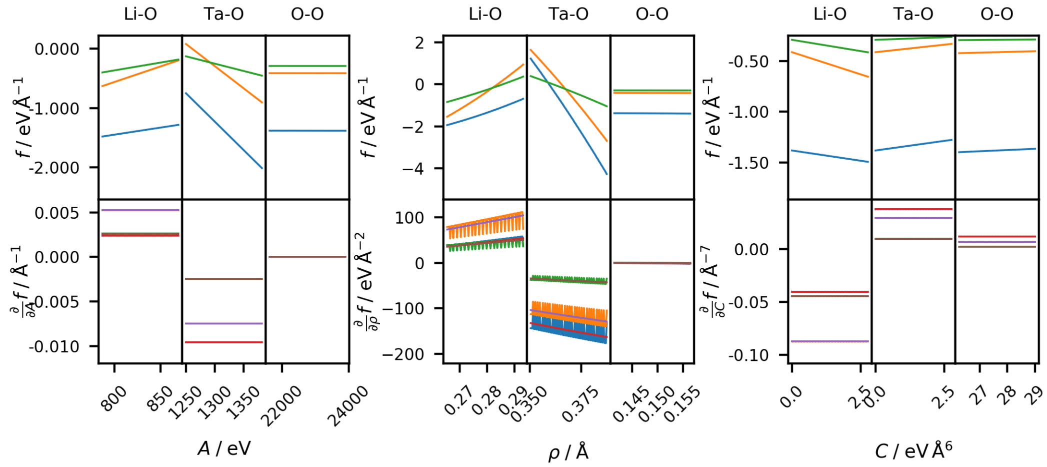

Figure 4.2 – Atomic forces on an oxygen atom (**top**) as a function of the parameters A, ρ and C of the Li-, Ta- and O-O pairs. (**bottom**) Graphs of the numerical and analytic derivatives of the three components of the forces with respect to each of the parameters of the pair. The numerical derivatives are characterized by an important noise, in particular visible on the middle panel.

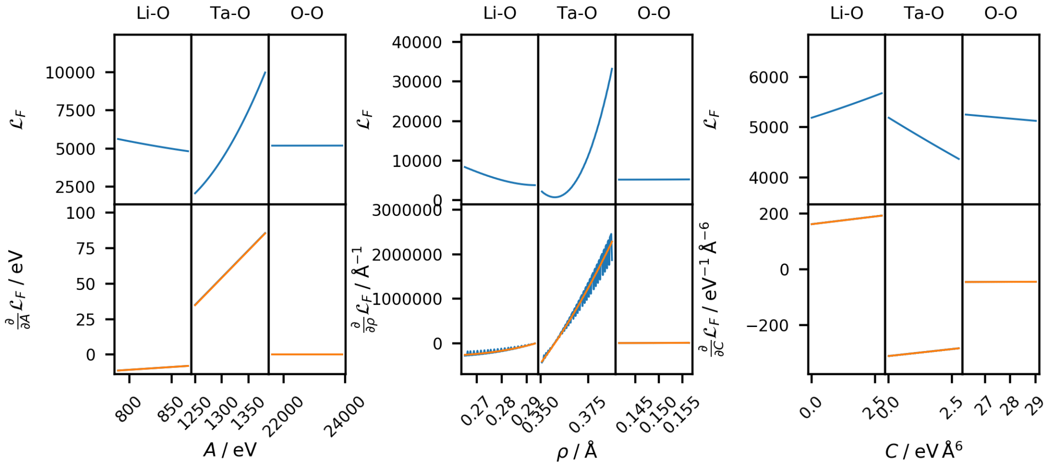

Figure 4.3 – Normalized value of $\mathcal{C}_F$ as a function of the parameters A, ρ and C of the Li-, Ta- and O-O pairs. The bottom figures show the numerical and analytic derivative of the upper functions. The numerical are characterized by a consequent noise carried over from the derivative of the forces.

Global Optimization

As shown in Fig. 4.4, the global optimization process is able to rapidly optimize the value of the loss function within few hundreds of iterations after which progress becomes extremely slow. The red line, indicative of the median value of the loss function is located closer to the minimum value of the window, showing that the algorithm quickly explores interesting areas of the phase space before exploiting the traits to optimize further these individuals.

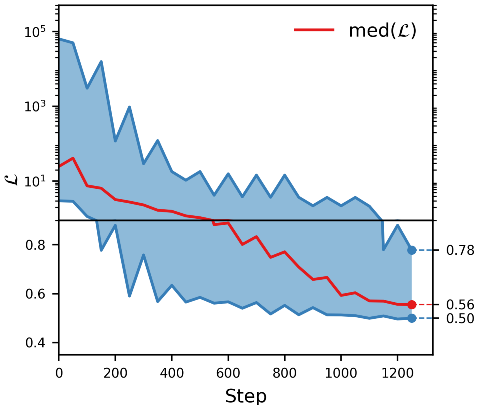

Figure 4.4 – Progress of the SADE population throughout the optimization

Paying closer attention to the top individuals of the population, the fittest one being investigated in Fig. 4.5, one can see that the forces are overall well fitted to the reference data when considering the ions. The result is not so straightforward when looking at the shells. The shells have a mean square error on the forces of 1.19 $\mathrm{eV}^2\,\mathrm{Å}^{-2}$, almost five times higher than the one of the ionic species at 0.25 $\mathrm{eV}^2\,\mathrm{Å}^{-2}$. To try to understand how this error will affect the position of the shells, and therefore the forces on the core particles and more widely on the whole system, it is interesting to relax the shells. Fig. 4.6 shows the updated forces for the structure with relaxed shells. This relaxation has its most visible impact on the force correlation of the oxygen cores. The mean square error for all ionic species however remains overall stable with a slight increase to 0.29 $\mathrm{eV}^2\,\mathrm{Å}^{-2}$. On the other hand, the mean square error on the shells goes down to 0.02 $\mathrm{eV}^2\,\mathrm{Å}^{-2}$, a value in line with the convergence criteria set for this initial relaxation. These relatively small changes in the oxygen core forces and the narrowing of the Li and Ta forces are a good indication that the force-field should already be able to successfully drive insightful molecular dynamics simulations.

Local Optimization

The second step of the optimization using the low-memory BFGS algorithm only marginally changes the parameters of the force-field. Fig. 4.7 and 4.8 show the resulting forces, before and after a relaxation of the shells, in a similar way to Fig. 4.5 and 4.6. The local optimization was not able to yield improved parameters though with a mean square error on the forces growing to 0.32 and 0.39 $\mathrm{eV}^2\,\mathrm{Å}^{-2}$ before and after relaxation. The gradients observed for the various parameters are small and resulting in oscillation of the parameters, with BFGS failing to converge in most cases.

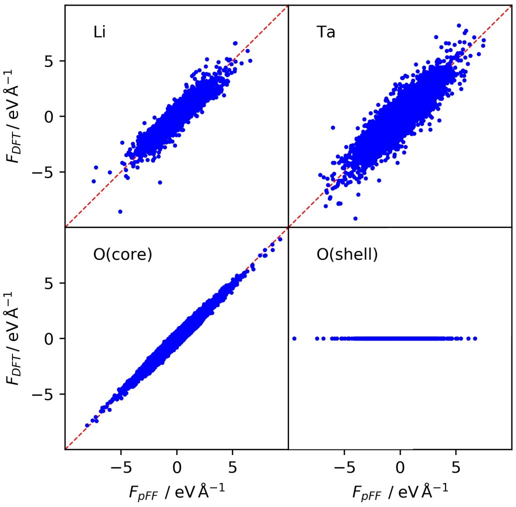

Figure 4.5 – Correlation of the reference DFT forces with the one computed using the trained force field. The latter ones are computed with the shells at positions minimizing the error on the oxygen, with a tolerance of 1 eVÅ^{-1}. For all core species, a good agreement is shown between the reference and fitted forces. The error on the forces of the shells are the only one staying relatively high.

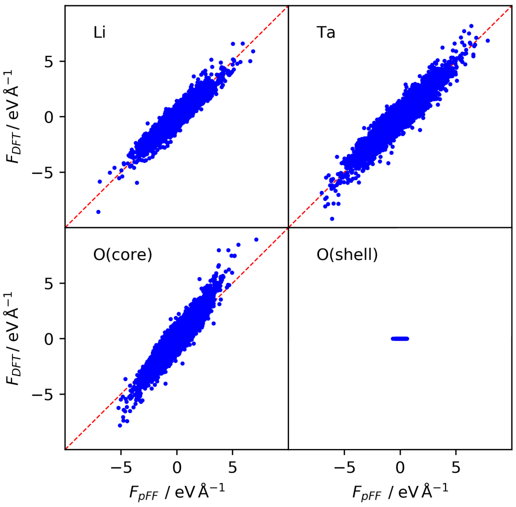

Figure 4.6 – Correlation of the reference DFT forces with the one computed using the trained force field. The latter ones are computed with the shells having been relaxed from their initial positions. The quality of the correlation remains high despite a tendency to underestimate the forces on the oxygen cores. The error on the forces of the shells is greatly reduced to the level of accuracy of the other forces.

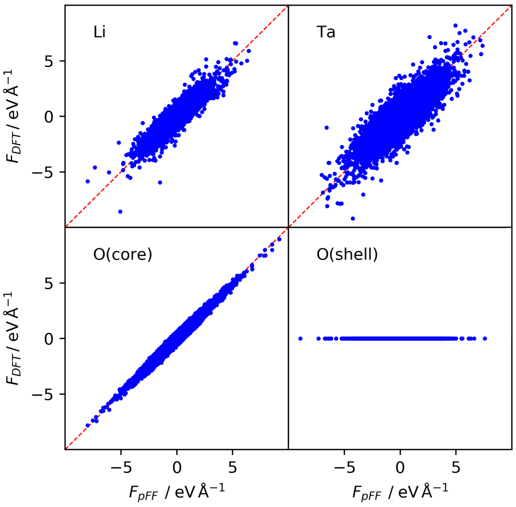

Figure 4.7 – Correlation of the reference DFT forces with the one computed using the locally optimized force field starting from the result of the global optimization. The latter ones are computed with the shells at positions minimizing the error on the oxygen, with a tolerance of 1 eVÅ^{-1}. No noticeable improvement can be seen compared to the results of the globally optimized parameters shown in Fig. 4.5.

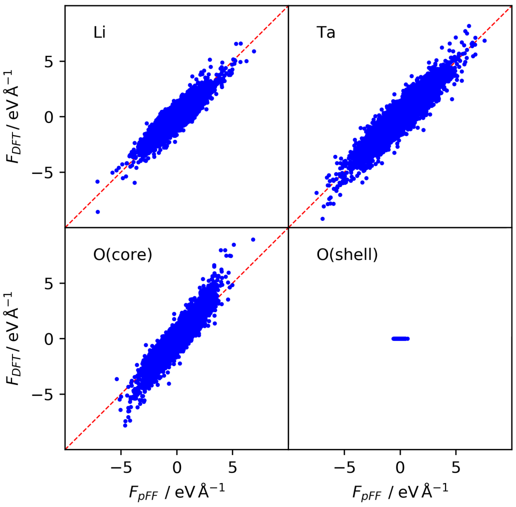

Figure 4.8 – Correlation of the reference DFT forces with the one computed using the trained force field. The latter ones are computed with the shells having been relaxed from their initial positions. Again, no noticeable improvement can be seen compared to the results of the globally optimized parameters shown in Fig. 4.6.

Conclusion

Global optimization methods have long been reliable tools in the optimization of complex multivariate problems. The fitting of force-field falls clearly in the problem definition and previous work has already shown the potential of genetic algorithms in the training of non-polarizable force-fields. In this chapter, a methodology for the application of differential evolution to the training of polarizable force-fields was demonstrated. It relies on the initial optimization of the shell position with respect to the error on the cores. This methodology reduces the problem to the more simple one of training a non-polarizable force-field.

The capacity of the methodology was demonstrated through the training of a force field for lithium tantalate. The resulting forces correlates well with the first-principle forces despite a failure to completely negate the forces on the shells. Further relaxation of the shells to their true equilibrium positions has however only lead to minor effects on the quality of the force correlation for the other elements. This shows that the method is a viable candidate for the generation of parameter sets for polarizable force-fields from first-principles data set. This is particularly interesting in the case of pairs where no previous polarizable force-field is reported. In the case of highly charged, ions the refinement of parameters from non polarizable force-field can be difficult. This was the case for the W – O pair described in Chap. 4 where the optimization of the parameters resulted in force-fields that were later unstable during simulations. A global optimization approach would have greatly helped to reduce the effort needed to produce a working force-field.

Efforts to improve the accuracy of the globally optimized parameters through the use of gradient-based local optimization was unsuccessful. Despite the successful reproduction of the numeric gradient through analytic means, in order to obtain smoother gradients, the small norm of the gradients with respect to the parameters of the O – O pair is problematic as this pair should plays a key role in the correction of the error on the shell forces.

5 Synthetic Training Set based Force-Field Parametrization

Introduction

The generation of training sets for the parametrization of a force-fields is usually done by running short first-principle trajectories [132] or force-field based ones with approximate parameters [133, 134]. The first method is extremely costly since it requires long trajectories to guarantee the presence of uncorrelated frames in the training sets. The second one allows to generate trajectories much faster. However, it still requires the input of a preexisting approximate force-field. Being able to generate training sets without the cost of such lengthy simulations or initial input of parameters is highly desirable for large scale training of parameters in the context of automated and unsupervised screening of material databases. The training sets used in Chapters 3 and 4 were generated using respectively the approximate force-field method and the first-principles based one.

Different approaches have already been attempted to take on the issue of the sampling of training structures. Of particular interest is the idea of approaching the training of the force-field self-consistently, using weaker versions of the force-field to generate trajectories through molecular dynamics. Structures are then selected during the trajectory and their forces computed using the reference first principles method. These new forces are then used to refine the parameters of the force-field. This scheme, named adaptive force-matching method [135] (AFM) was introduced by Akin-Ojo *et al.* in 2008 and its potential is demonstrated on the development of a force-field for water, a particularly difficult task. The authors suggest in particular that this methodology could be applied using QM/MM systems where representative QM clusters are used to refine the force-field parameters of the MM domain on-the-fly.

A different approach was discussed by Fracchia *et al.* [134], whose proposed methodology is based on the optimal selection of the set of training structures from a trajectory. Focusing on the solvation of metal salts into water, they make use of a metal-centric dissimilarity score to tackle the case. They use a greedy randomized adaptive search procedure (GRASP) to optimize the dissimilarity score of a training set drawn from trajectories generated using parallel tempering. This methodology however does not solve the issues discussed previously since it concentrates on the optimal selection of the structures to be used for the training rather than their generation.

Here, a methodology is proposed for the unsupervised generation of a training set with high resemblance to molecular dynamics trajectories and their use for the training of a force-field. The procedure uses the addition of random thermal fluctuations to crystallographic structures to generate a training set with structural descriptor similar to a molecular dynamics trajectory. The forces and energies of these structures are then computed and used for the training of a force-field. The presence in most solid-state electrolytes of partially occupied sites stands as an obstacle to the direct use of this methodology. To circumvent it, a procedure is proposed to build a library of possible realization of these partially occupied structures using an initial Monte-Carlo simulation. This simulation is driven by the Coulomb interaction between the atoms in the structure, considered as point charges.

To allow the use of the procedure described above in an automated and unsupervised fashion, it was implemented as a plugin for the AiiDA [79] platform. AiiDA is an interactive infrastructure and database designed for the automation of computational science. The framework is based on the so-called ADES model, ADES standing for the four pillar on which it is built: **A**utomation, **D**ata, **E**nvironment and **S**haring. The first pillar, Automation, is responsible for the abstraction of all low-level tasks such as the preparation, submission, monitoring, and retrieval of computations on remote high performance computers, as well as the the storage of the results of these computations. The second pillar, Data, focuses on the modeling of the data and the management of its storage. In particular the issues of provenance is emphasized by organizing the data into an acyclic directional graph that allows users to follow and even reproduce the flow of data and computations that led to a specific result. While the two first pillars relates to the abstraction of low-level concepts, the third pillar, Environment, provides a higher-level, user facing environment designed to leverage the two first pillars. Two important aspects of this environment are the the plugins and the workchains. Plugins allow to enrich the environment by interfacing with various computational packages such as QUANTUM ESPRESSO [136]. On the other hand, a workchain is a structure allowing developers and users to implement a scientific workflow into the AiiDA environment. Workchains allow the creation of checkpoints, the access to other workflows, or the submission of calculations. These operations can be done asynchronously, allowing the parallelization of operations operations. The fourth and last pillar, Sharing, is dedicated to the creation of an infrastructure for the sharing of scientific results and workflows through the standardization of data and the creation of repositories. The last point is exemplified by the use of AiiDA to power the Materials Cloud platform (https://www.materialscloud.org), a platform developed for the sharing of resources in computational materials science. The implemented workchains are available on GitHub (https://github.com/zrl-aiida-toolbox/zrl-aiida-toolbox).

To demonstrate the capabilities of the methodology, the training of a force-field for lithium tantalates is achieved in this chapter. The starting points for the training are three structures available in the Inorganic Crystal Structure Database (ICSD). The three structures, with collection codes 74949[137], 74950 [137] and 423372 [37] are from that point referred as structures A, B and C. The structures A and B are the ones initially reported by Wehrum *et al.* in 1994. A is a highly symmetric rhombohedral crystal ($R\bar{3}$) with a partially occupied Li site and B is a less symmetrical rhombohedral crystal ($P3$) with all its sites fully occupied. Finally, C was reported by Mühle *et al.* in 2004. Though they observe a similar cell structure to the one reported by Wehrum *et al.* for Li_7BiO_6, they report a triclinic one ($P\bar{1}$) for Li_7TaO_6. The training is done using all three structures. To assess the quality of the resulting force-field, various structural and dynamic properties are investigated and compared to previous experimental and computational results.

Methodology

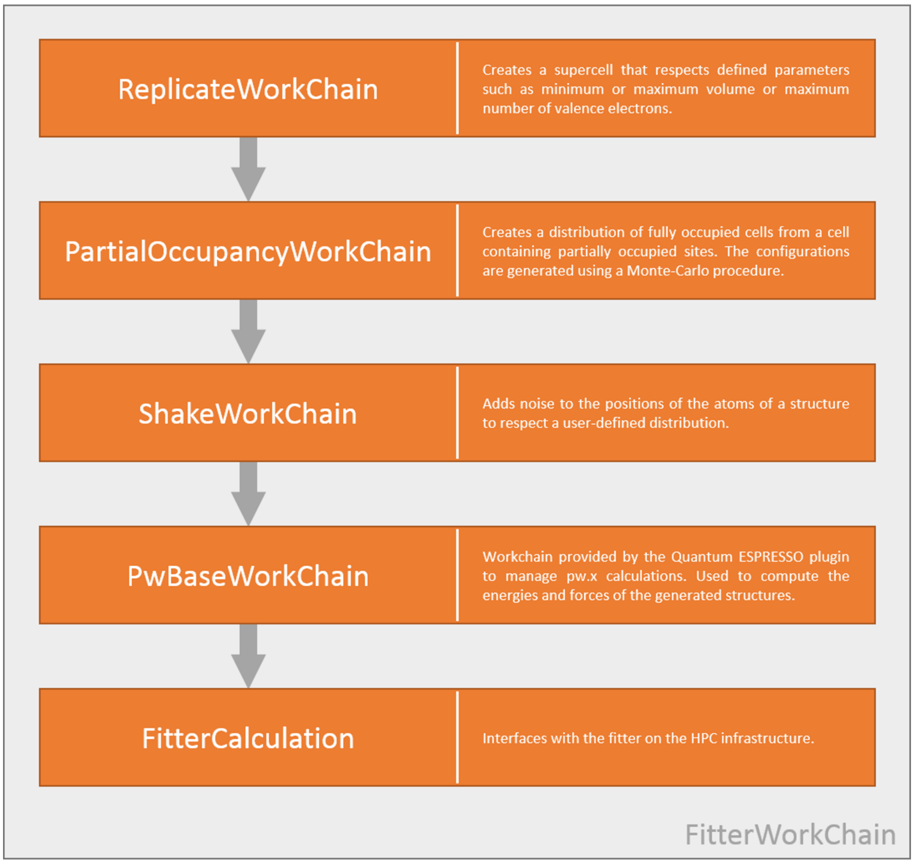

Creates a supercell that respects defined parameters such as minimum or maximum volume or maximum number of valence electrons.

Creates a distribution of fully occupied cells from a cell containing partially occupied sites. The configurations are generated using a Monte-Carlo procedure.

Adds noise to the positions of the atoms of a structure to respect a user-defined distribution.

Workchain provided by the Quantum ESPRESSO plugin to manage pw.x calculations. Used to compute the energies and forces of the generated structures.

Interfaces with the fitter on the HPC infrastructure.

Figure 5.1 – Diagram of the implemented fitting procedure.

The fitting procedure presented in the introduction and summarized in Fig. 5.1 was split into five workchains and a calculation plugin implemented using the AiiDA platform. More details on the implementation of the *ShakeWorkChain* and *PartialOccupancyWorkChain* are discussed further in the chapter. Fig. 5.2 shows the typical graph resulting from the execution of the *FitterWorkChain*.

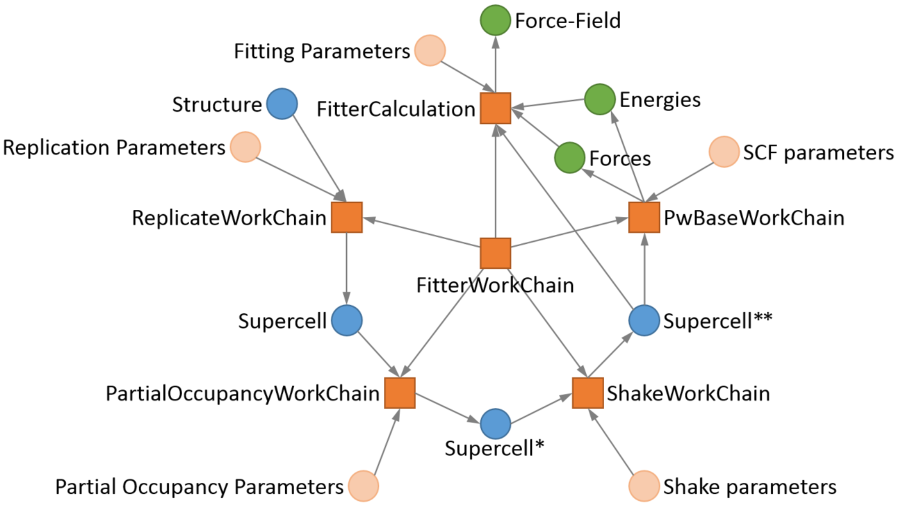
Force-Field
Fitting Parameters
Structure
FitterCalculation
Energies
Replication Parameters
Forces
SCF parameters
ReplicateWorkChain
PwBaseWorkChain
FitterWorkChain
Supercell
Supercell**
PartialOccupancyWorkChain
ShakeWorkChain
Supercell*
Partial Occupancy Parameters
Shake parameters

Figure 5.2 – Representation of the typical directed graph resulting of the use of the *FitterWorkChain*. WorkChains and Calculations are represented by orange boxes, structures by blue circle, input dictionaries by light orange circles and results by green circles. Supercell* represent a supercell with no partial occupancy and Supercell** one with added thermal noise.

Partial occupation

To handle the partial occupation of sites in a structure, the sites with non integer occupancy are first grouped based on their composition, *i.e.* similar elements with similar occupations are grouped together. This first step allows the conservation of the occupancy for each type of site. Each groups are then randomly filled with atoms the needed number of atoms to respect its occupancy. Finally, to select favorable configurations, a Monte-Carlo simulation is run. Each step corresponds to the random move of a ion from one site to another one in the same group. The energy of each visited configuration is approximated by the energy resulting of the Coulombic interactions between all atoms, considered as point charges. The new configurations are accepted if energetically favorable, *i.e.*:

$$\min\left(1, e^{-\beta\Delta E}\right) > r \tag{5.1}$$

where ΔE is the difference between the energy of the old and new configuration, $\beta = (k_\mathrm{B} T)^{-1}$ with k_B, the Boltzmann constant and T is the effective temperature and r is a random number drawn from a uniform distribution, $\mathcal{U}(0,1)$. Long enough trajectory will result in Boltzmann distributed sets of structures.

The correctness of the distribution will however only hold if the selection criterion used for the Monte Carlo trajectories is accurate enough. This will be the case if the change in the approximated energy used, *i.e.* the Coulombic potential of the structure, is proportional to the actual change in energy. To establish this equivalence, Fig. 5.3 shows, for several known solid-state ionic conductors, a comparison between the energies of randomly drawn structures

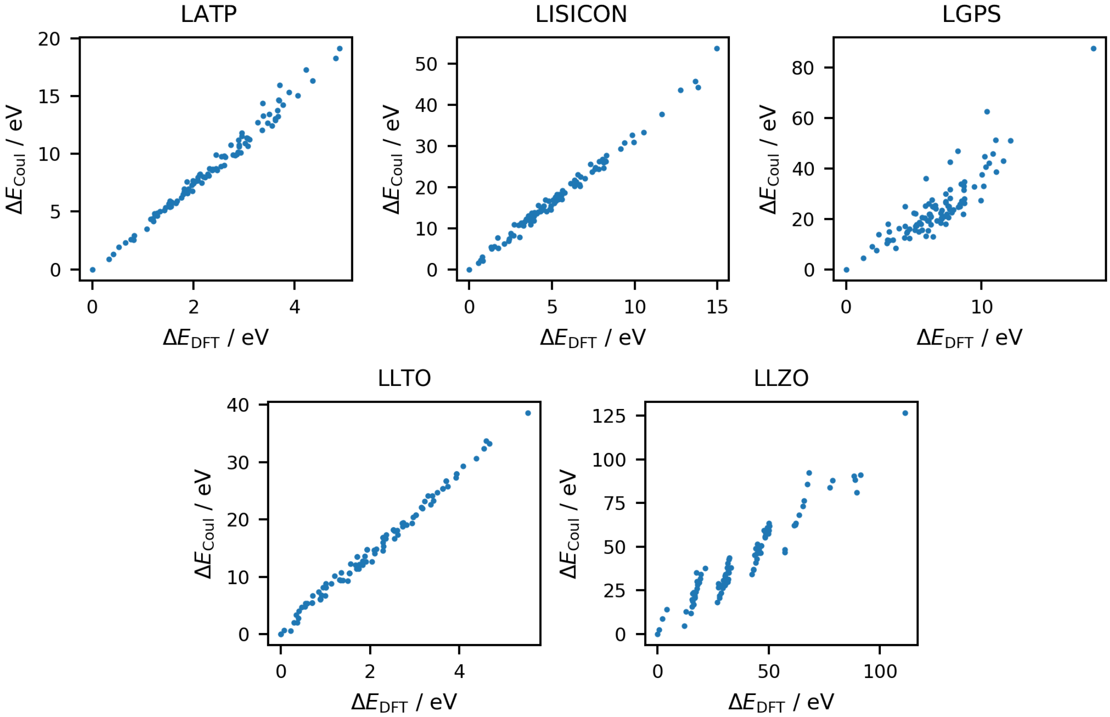

Figure 5.3 – DFT versus Coulombic energy for random structures of 5 classes of ionic conductors (LATP, LISICON, LGPS, LLTO and LLZO) showing high correlation between both models.

computed using the Coulombic approximation and their DFT energies. The data shows a high degree of correlation between the two methods allowing a linear fit of the data

$$E_{\mathrm{Coul}} = \alpha E + \beta, \tag{5.2}$$

demonstrating the validity of the approach in the selection of lower energy domains of the phase space. Some substructures can be observed in the case of LLZO, more likely related to the two independent partially occupied lithium sites.

The slope α is however larger than 1 for all fits but the one of LLZO. This will lead to an overestimation of the change in energy between the structures when using the Coulombic model

$$\Delta E_{\mathrm{Coul}} = \alpha \Delta E_{\mathrm{DFT}}. \tag{5.3}$$

Overestimating the change in energy will skew the trajectory towards lower energy structures and prevent a correct reproduction of the structure distribution. Scaling the effective temperature in Eq. 5.1 by the same factor α can restore the distribution.

This algorithm is implemented in the *PartialOccupancyWorkChain*. Three schemes are made available for the selection of a subset of the structures visited during the simulation. Two simple schemes select either the last or lowest energy structures visited during the trajectory. Though these schemes can be useful in specific cases, they will cancel the distribution observed during the trajectory. The final scheme uses reservoir sampling to select random structures from the trajectory. Reservoir sampling is a useful algorithm allowing to randomly sample a stream without the need to store it or to know its length. It works in the following way. To select n random structures from a trajectory, the n first visited structures are selected and stored in a size-n array. Each structure visited afterwards is then selected if $\mathscr{U}(0,1) < \frac{n}{i}$. In case the structure is selected, it will replace a structure in the array at random. This schemes guarantees the probability of keeping any of the visited structures has an equal probability, no matter how long the trajectory. A schematic representation of the process is presented in Fig. 5.4.

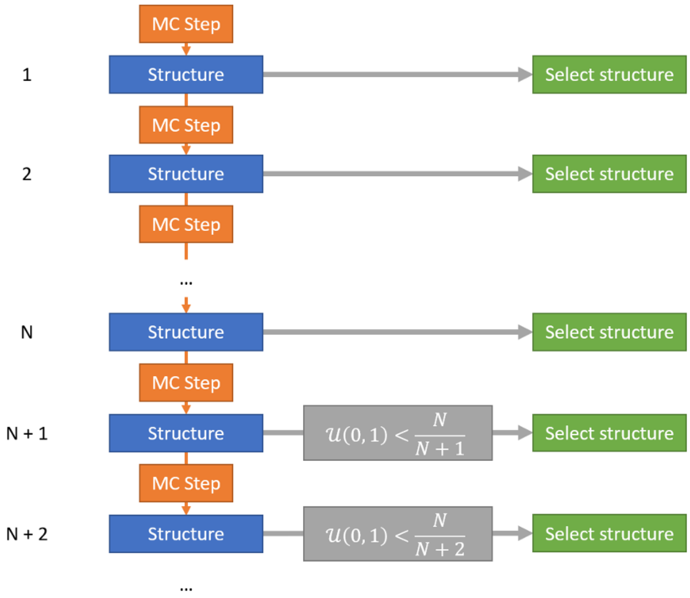
MC Step
1
Structure
Select structure
MC Step
2
Structure
Select structure
MC Step
...
N
Structure
Select structure
MC Step
N + 1
Structure
$\mathcal{U}(0,1) < \frac{N}{N+1}$
Select structure
MC Step
N + 2
Structure
$\mathcal{U}(0,1) < \frac{N}{N+2}$
Select structure
...

Figure 5.4 – Schematic representation of the *PartialOccupancyWorkChain* with *Reservoir sampling*. Each Monte Carlo step correspond to numerous swap attempts within the different group of sites. After the step, the structure is selected or discarded with probability i/n, with i the current step and n the target number of selection leading to an equiprobable selection of all the visited structures.

Thermal fluctuations

The addition of thermal fluctuation to the atomic positions is central to the replication of the structural properties of the training data since it is essential to reproduce a distribution of interatomic distances comparable to that observed in a molecular dynamics trajectory. Fig. 5.5 show the distribution of the displacement of the particles from their average position in a first principle based trajectory of lithium tantalate. The trajectories are the ones used in Chapter 4 for the parametrization of the force-field.

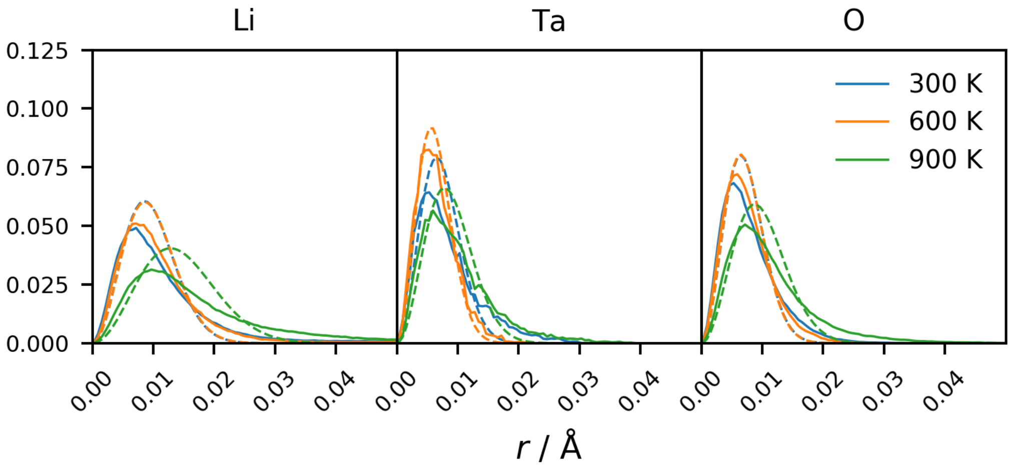

Figure 5.5 – Distribution of the displacement of each ionic species from their mean position in trajectories at 300, 600 and 900 K. The dashed line shows the Maxwell-Boltzmann distributions parametrized to minimize the mean square error.

Along the observed distributions, Maxwell-Boltzmann distributions parametrized to minimize the mean square error of the distribution with respect to the simulated one are shown. These distributions are the best fits for the distribution though they underestimate their tails. This is particularly true for the displacement of lithium at higher temperatures. This last point is likely linked to the diffusive behavior of the lithium which will not be reproduced by simply adding noise to the equilibrium positions.

The *ShakeWorkChain* allows to add to a provided structure thermal fluctuations corresponding to the desired distribution. For each atom in the structure, a random displacement is added. This displacement is defined by a direction and a norm. The direction is defined by a random vector of norm 1. The norm is defined by a random number, drawn from a user defined distribution, the Maxwell-Boltzmann distribution in this specific case.

Force calculation and fitting

The force calculation is done using QUANTUM ESPRESSO through the *PwBaseWorkChain*. An energy cutoff of 70 Ry and 560 Ry for the wavefunction and electron density respectively are used for the computation of the energy and forces of the lithium tantalate structures.

The global optimization was accomplished with various population sizes and regularizations. The parameters were restricted to ranges detailed in Table 5.1.

Pair	Li – O		Ta – O		O – O	
Parameter	Min	Max	Min	Max	Min	Max
A [eV]	0.000	5000.000	0.000	5000.000	0.000	30000.000
ρ [Å]	0.100	0.900	0.100	0.900	0.100	0.900
C [eV Å^6]	0.000	10.000	0.000	10.000	0.000	50.000

Table 5.1 – Parameter ranges for the reported training.

Results

Partial occupation

Of the three structures used for the training, only A and C, exhibit partially occupied sites in their crystallographic structures. To compute the scaling factor α for their Coulomb potential, random structures were drawn for each phase and their purely Coulombic and DFT energies were computed. Fig. 5.6 shows the correlation between those two energies. The linear fit of the data is also included with scaling factors α of 3.627 and 3.346.

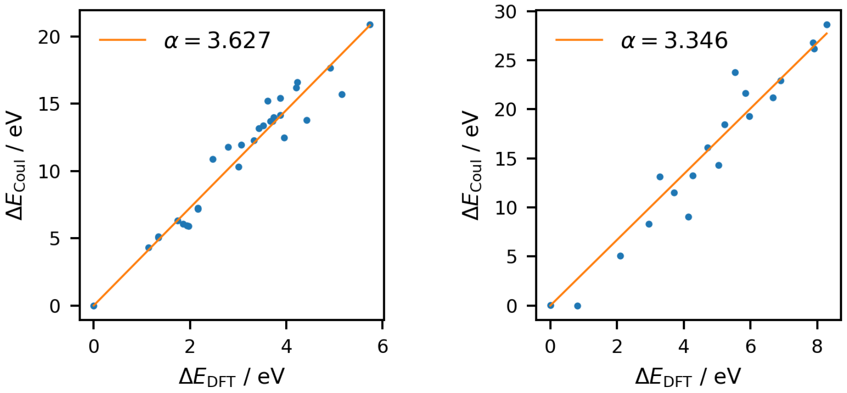

Figure 5.6 – DFT versus Coulombic energy of randomly selected structures for the two phases of lithium tantalate with partially occupied sites. The orange line show the slope, α of the linear fit of the data.

Fig. 5.7 shows 6 Monte-Carlo trajectories computed for each of the two phases at effective temperatures of 300, 600 and 900 K with a common α value of 3.5 for both structures. Each trajectory is composed of 5000 rounds of equilibration followed by 20000 rounds of simulation where each round is composed of 100 selection step with 1, 3 or 5 swaps. The energy of the systems shows an initial drop during the equilibration of the system away from the high energy random initial structures. The system then converges to low energies configurations. The two structures then show quite different behavior. Structure A shows the expected behavior with what resemble the expected Maxwell-Boltzmann distribution of energies. Structure B however remains stuck in two low energy levels with only the higher 900 K temperature being able to reach higher energies. The issue here lies with the algorithm used for the selection of the site groups. Structure B presents 4 different Li sites with occupancy 0.875 which are grouped

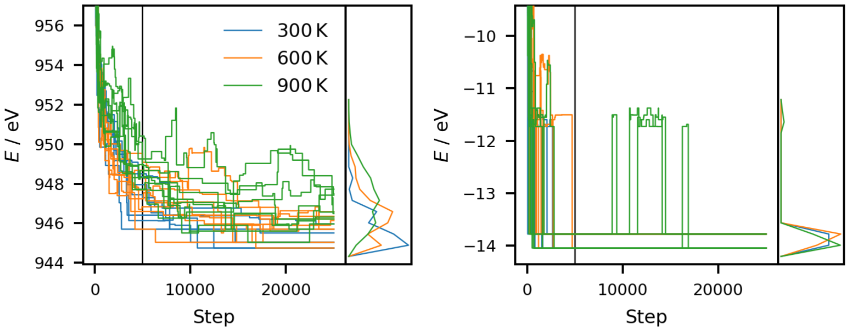

Figure 5.7 – Energy along Monte-Carlo trajectories used to resolve the occupancy of partially occupied sites of structures A (**left**) and B (**right**), corresponding to the ICSD entries 74949 [137] and 413372 [37] respectively. Three temperatures, 300 K (**blue**), 600 K (**orange**) and 900 K (**green**) are shown. Next to the energy is displayed the energy distribution of the visited states after the initial equilibration.

together in the current methodology. A quick fix is to add small variations to these sites occupancy. Similar trajectories were computed with occupancy guaranteeing the segregation of the four lithium sites. The resulting trajectories are presented in Fig. 5.8. The change made in the site grouping is results in the reproduction of a Boltzmann like distribution of energies throughout the trajectory. The methodology successfully yields structures with energies following a Boltzmann like distribution if the sites are correctly grouped. Random sampling from the trajectory can therefore be used to generate a representative set of fully defined structures for the training sets.

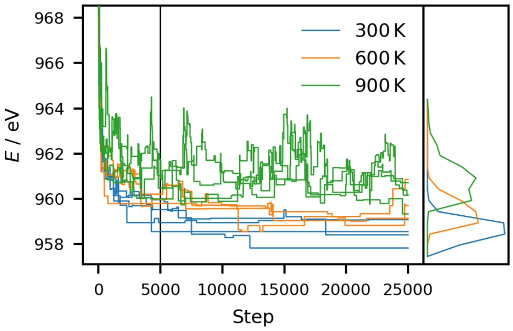

Figure 5.8 – Energy along Monte-Carlo trajectories of structure C, corresponding to the ICSD entry 413372 [37] with the sites correctly grouped to guarantee the occupancy of all four lithium sites at three temperature, 300 K (**blue**), 600 K (**orange**) and 900 K (**green**). Next to the energy is displayed the energy distribution of the visited states after the initial equilibration.

Thermal fluctuations

A random subset of the structures from the Monte Carlo trajectories are used to generate the training structures. Noise is added to the atomic positions to simulate thermal fluctuations.

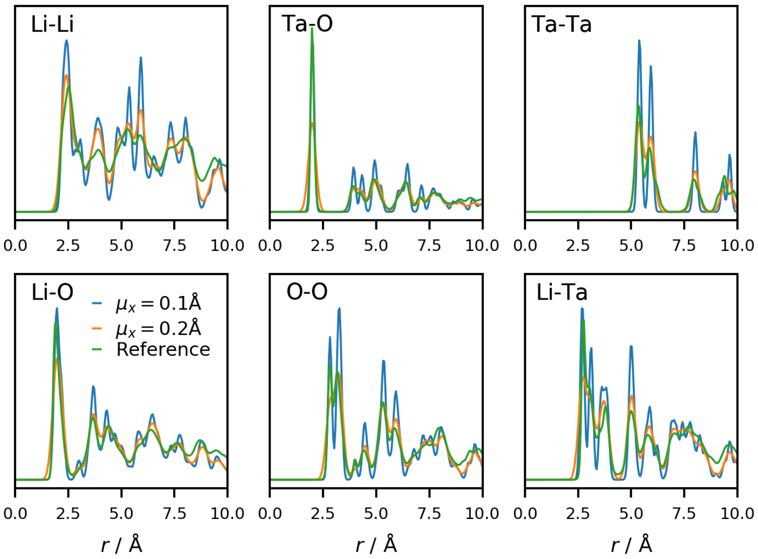

Figure 5.9 – Radial distribution function, $g(r)$, of lithium tantalate structures generated using Monte-Carlo and artificial thermal noise. Three distributions of the thermal noise are compared with various standard deviations: Maxwell-Boltzmann (**left**), normal (**center**) and exponential (**right**). The radial distribution function of a first-principle trajectory is also drawn for reference.

The norm of the noise is drawn from a Maxwell-Boltzmann distribution of mean 0.1 and 0.2 Å. The radial pair distribution of the resulting structures is shown in Figure 5.9 along with the ones of the reference trajectories. The pair distributions match relatively well the ones present in the first-principle dynamics. The lithium containing pairs are the least accurately represented with some missing finer features. These discrepancies are most likely caused by the absence of lithium density in the diffusive pathways of the structures as mentioned earlier. Instead, the ions are solely located around their equilibrium positions around the crystallographic sites. The rest of the pair distributions are better approximations of the pair distributions of the reference trajectory, despite relatively small under- and overestimation of the width of some of the peaks. From these results, one can expect that the generated structures are sufficiently representative of the reference trajectories and should be a good approximation for the training of the force field.

Atomic forces

With a set of structures showing good agreement with the reference trajectories in term of pair distributions, it is important to consider whether the reference data, the forces, is also appropriately reproduced. The distribution of amplitude of the forces on the different species in the synthetic set is compared to the reference trajectory in Fig. 5.10. The distribution is well reproduced in the case of the lithium ions. In the case of the heavier tantalum and oxygen however, the synthetic set falls short. The structures contained in the training set show

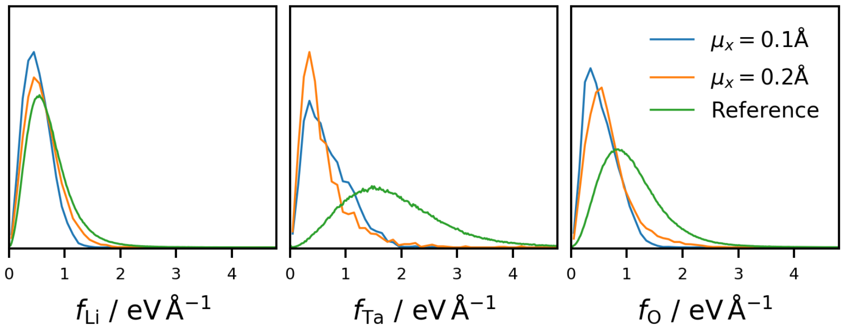

Figure 5.10 – Distribution of the amplitude of the atomic forces in the reference DFT trajectories (**green**) compared to the ones generated using a mean displacement of 0.1 (**blue**) and 0.2 Å (**orange**). The distributions are shown for lithium (**left**), tantalum (**center**) and oxygen (**right**) particles.

forces with lower amplitude for these two atoms. This discrepancy can be due to the lack of correlation in the random displacement of the particles and in particular the absence of any vibrational modes or concerted movement which might push the system further out of equilibrium. This however should not have any negative impact on the fitting of the short-range potential. The good reproduction of the radial distribution of the O-X pairs should guarantee a good sampling of the potential.

Global optimization

Fig. 5.11 shows the potential obtained by global optimization of the parameter using minimum barrier of 5, 10, 20, and 40 eV. Although the different optimizations were initialized with different random parameter populations, they converge to very similar potentials, with little influence of the height of the barrier. Table 5.2 shows the parameters of the force-fields trained using a population size of 100. The various parameters are stable with the largest differences being present in the O – O pair where the difference in the potential and its relation to the minimum enforced barrier is clearly visible in Fig. 5.11. It is interesting to note that the divergence of the O – O potentials occurs below the 2.5 Å corresponding to the first solvation shell of the O – O pair. The difference in the three potentials should therefore have minimal effect. For both the Li – O and Ta – O pairs, the attractive part of the potential is negligible compared to the repulsive one. For both the Ta – O and O – O pairs, the *C* parameter finds itself "saturated", at the border of the range of allowed values.

Given the similarity of the parameters, it comes as no surprise that the energies and forces computed using these force-fields are very similar. Fig. 5.12 and 5.13 show the correlation between the reference DFT energies and forces and the computed force-field ones after relaxation of the shell positions. The computed energies are in good agreement with their reference counterpart while the forces have some divergence with a general underestimation of the forces by the force-field, the largest departure with the reference forces happening for

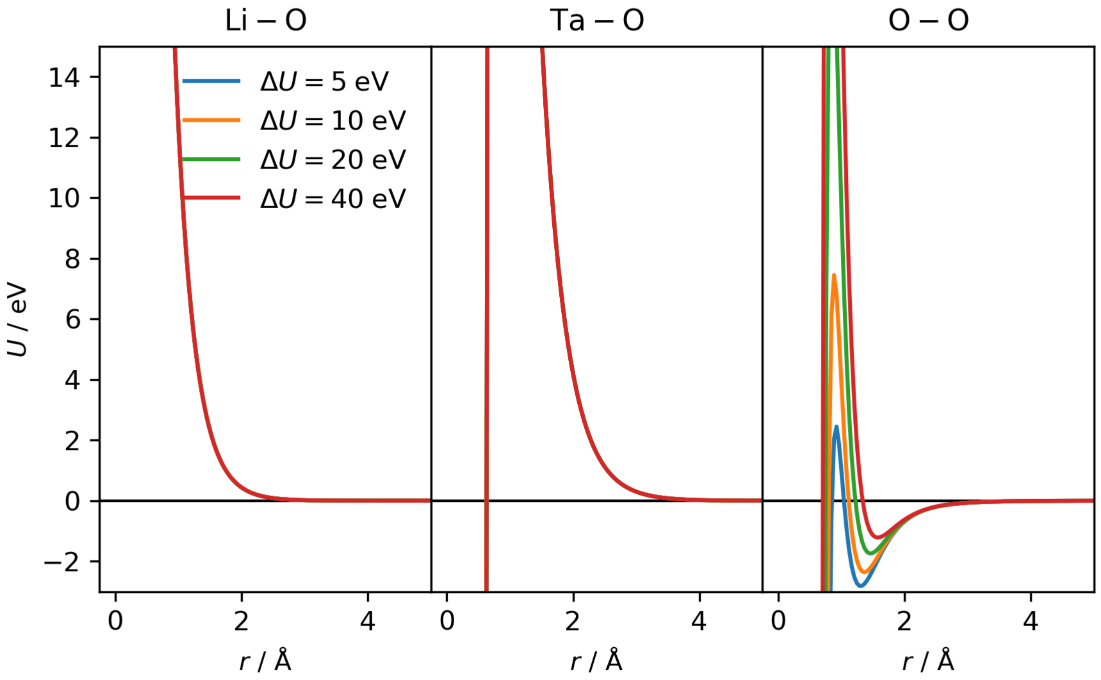

Figure 5.11 – Pair potentials parametrized for the Li–O, Ta–O and O–O pairs with enforced barriers of 5, 10, 20 and 40 eV and parameters described in Table 5.1. The parameter for all potentials can be found in Table 5.2.

Pair	Parameter	$\Delta U = 5\,\text{eV}$	$\Delta U = 10\,\text{eV}$	$\Delta U = 20\,\text{eV}$	$\Delta U = 40\,\text{eV}$
Li–O	$A\,[\text{eV}]$	349.392	349.849	350.773	352.149
	$\rho\,[\text{Å}]$	0.29930	0.29920	0.29900	0.29870
	$C\,[\text{eV}\,\text{Å}^6]$	0.000	0.000	0.000	0.000
Ta–O	$A\,[\text{eV}]$	854.414	855.000	856.119	857.701
	$\rho\,[\text{Å}]$	0.37910	0.37900	0.37880	0.37850
	$C\,[\text{eV}\,\text{Å}^6]$	10.000	10.000	10.000	10.000
O–O	$A\,[\text{eV}]$	29892.060	29983.081	29978.320	29930.250
	$\rho\,[\text{Å}]$	0.15690	0.15820	0.16080	0.16430
	$C\,[\text{eV}\,\text{Å}^6]$	50.000	50.000	50.000	50.000

Table 5.2 – Parameters of globally optimized force-field using populations of 100 individuals and starting from different random populations. The Li–O and Ta–O pair parameters converge to very similar values while the O–O pair shows the largest difference.

the forces of the oxygen.

To further gauge the quality of the force-field, NPT trajectories where run between 300 and 900 K with increments of 50 K for the force-fields obtained with minimum barriers of 5, 10 and 20 eV. Fig. 5.14 shows averaged structural parameters *i.e.* volumes, lattice vector lengths and angles for each of the three structures A, B and C. The reference crystallographic values are indicated by horizontal dashed lines. As suggested earlier the minimum barrier used

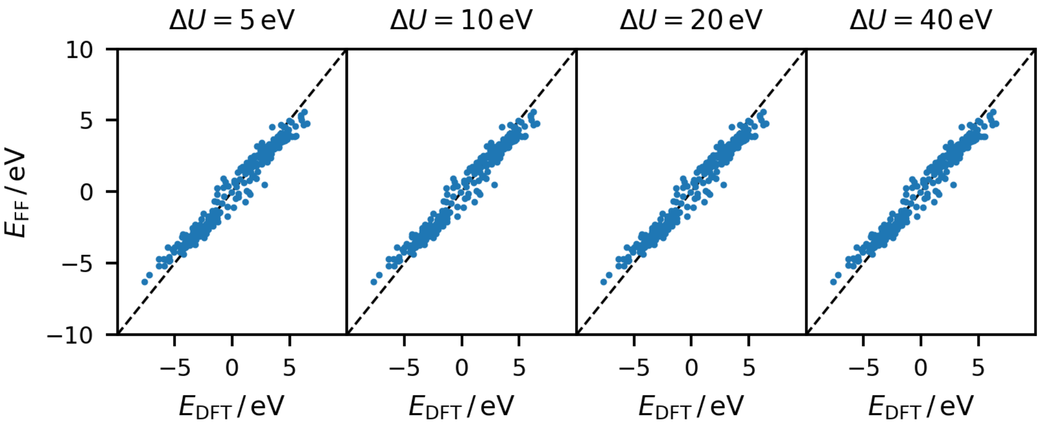

Figure 5.12 – Correlation plot between the reference DFT energies and the one given by the force-field after relaxation of the shells.

for the regularization does not seem to play any role with the three force-field giving very similar results and highest variations in the low temperatures. The trajectories starting from the two hexagonal cells, structures A and B, behave in a very similar fashion with the a and b vectors being fairly well reproduced while the c vector contracts slightly compared to the crystallographic data. The cell volume is overall well respected with an error of about 3% compared with the experimental crystallographic volume. The angles are again well conserved with the structure keeping its hexagonal shape. The reproduction of structure C is less successful. Though the volume is underestimated with a similar amplitude. The cell geometry however changes dramatically from its crystallographic reference. Its angles α and β change from the reported values of 120° to about 90°, while the γ angle increases from 63° to approximately 70°.

The mean square displacement of the lithium ions during the 750 ps of NPT trajectories are computed with a maximum lag time of 200 ps and displayed in Fig. 5.15. The force-field does not show much influence on the mean squared displacement, which is not very surprising given the similar structural result shown by the three force-field reported here. The diffusion coefficients are computed from the mean squared displacement of the lithium ions in the NPT trajectories where the lag time was superior to 150 ps, The resulting diffusion coefficient are plotted in the Arrhenius plots in Fig. 5.16. The diffusion coefficients follow the expected Arrhenius behavior with activation energies between 0.23 and 0.30 eV. These values are much lower than the experimental value of 0.66 eV [36]. They are however similar to the one reported by Muhle *et al.* [37] for the high-temperature behavior of the system, *i.e.* 0.28 eV. Previous first principle and force-field dynamics have described similar values. This points to the lithium in the system being much more mobile than in the experiment, mirroring more the high temperature behavior described by Muhle *et al.* with a liquid like lithium sublattice. This overestimation of the lithium mobility is also reflected in the absolute value of the conductivity. Muhle *et al.* report a conductivity between 10^{-7} and $0.2\,\mathrm{S\,cm^{-1}}$ for temperatures between 300

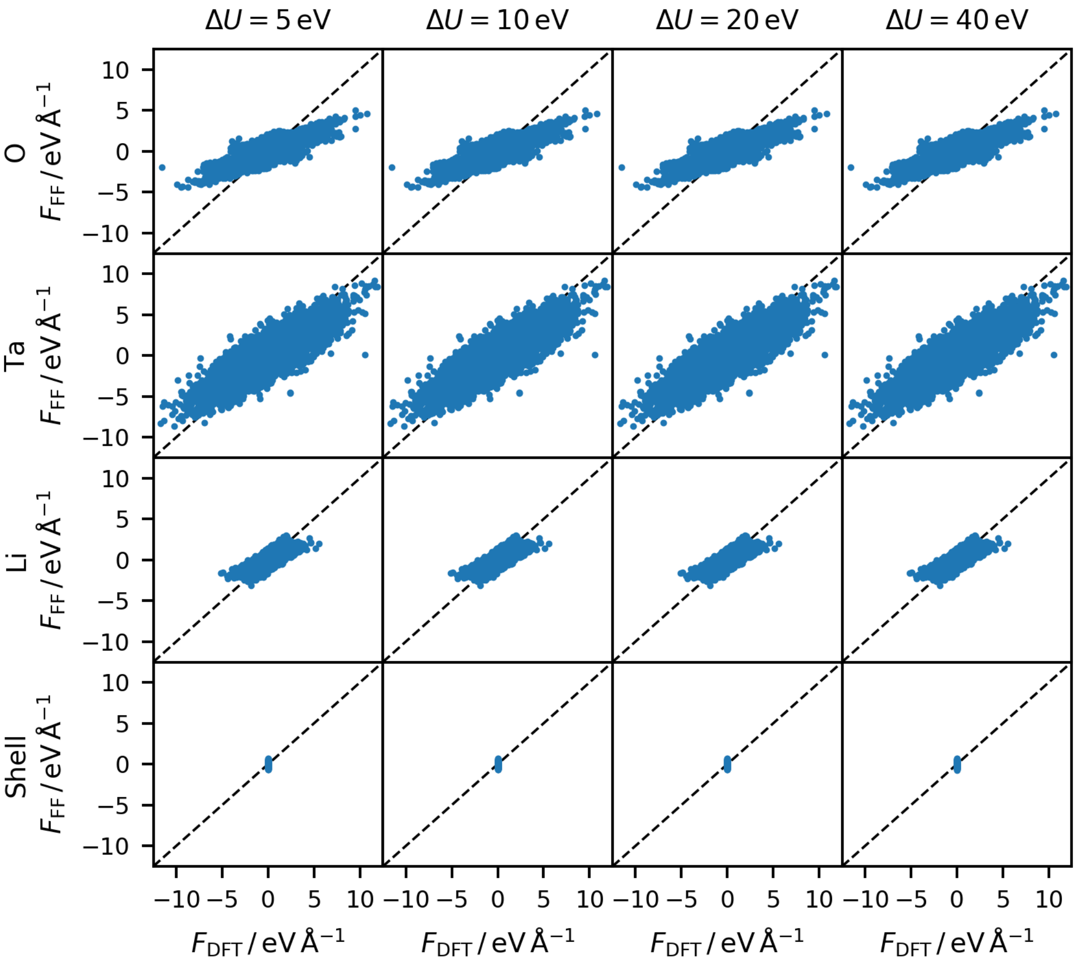

Figure 5.13 – Correlation plot between the reference DFT forces and the ones given by the force-field after relaxation of the shells.

and 800 K with the phase transition occuring around 700 K. In comparison the values obtained by simulation are situated between 10^{-2} and $10\,\mathrm{S\,cm^{-1}}$ for temperatures between 300 and 700 K.

The mean square displacement and diffusion coefficient were also computed using constant volume trajectories with the averaged structure parameters presented in Fig. 5.14. This time only the two rhombohedral structures A and B were used since the force-field was not able to correctly reproduce the structure of C. Fig. 5.17 present the mean square displacements at constant temperature and energy for the force-fields optimized with minimum energy barrier of 10 and 20 eV. The resulting mean square displacements in NVT trajectories are very similar to the ones of the initial NPT trajectories showing no significant effect of the volume change on the lithium diffusion. On the other hand, the NVE trajectories display an increased mean square displacement by a factor 1.5 with respect to the constant temperature trajectories. This shows that the GLE thermostat has a visible effect on the lithium dynamics and diffusion in the

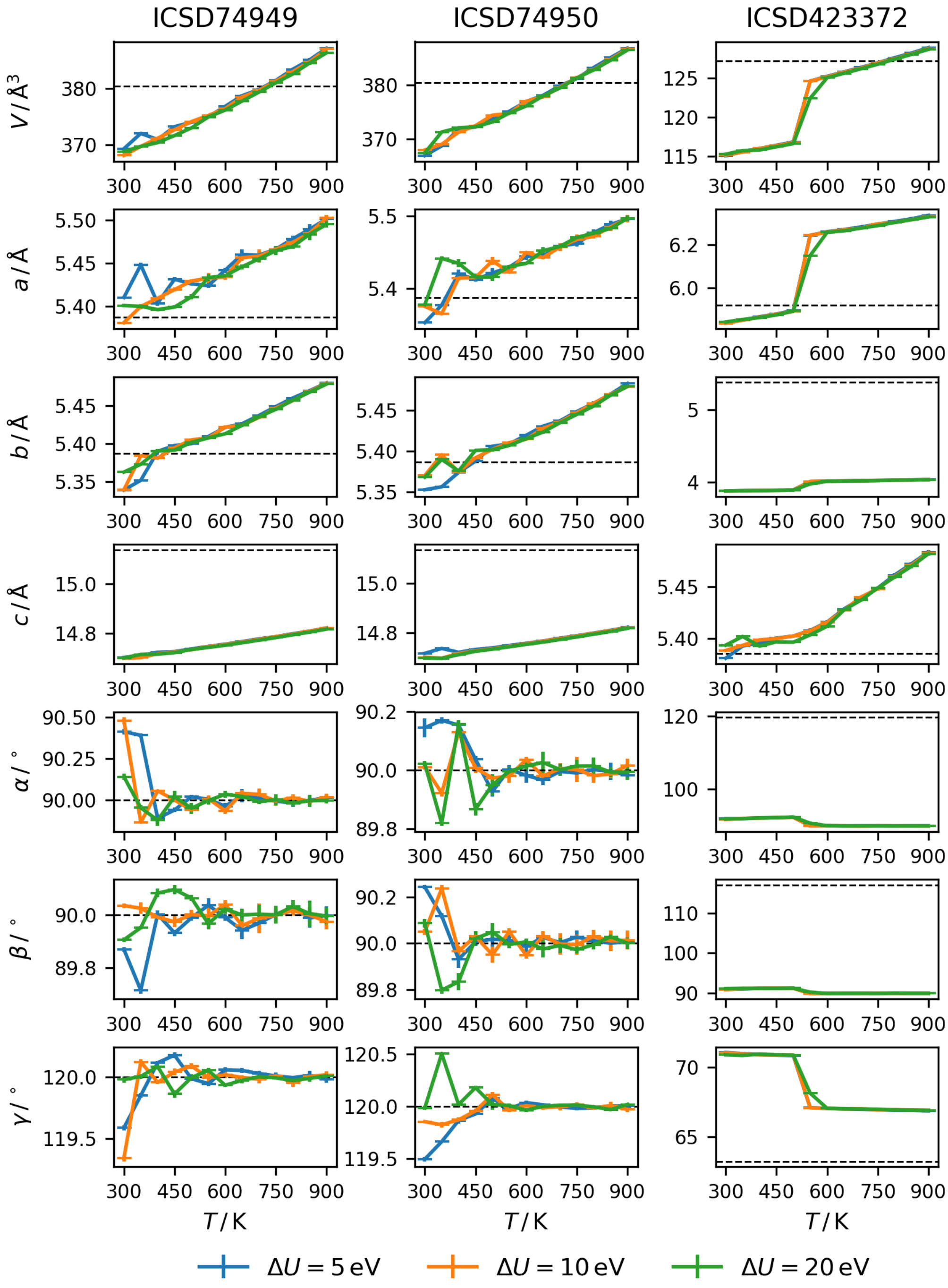

Figure 5.14 – Volumes, lattice parameters and angles averaged over NPT trajectories between 300 and 900 K using the force-field obtained with a minimum barrier ΔU of 5, 10 and 20 eV. The volume shows a linear increase without phase change. Similarly, the length of the lattice vectors and angle stay stable throughout the simulations. Each point is averaged over 750 ps of simulation and the error is estimated using bloc averages over blocs of 150 ps.

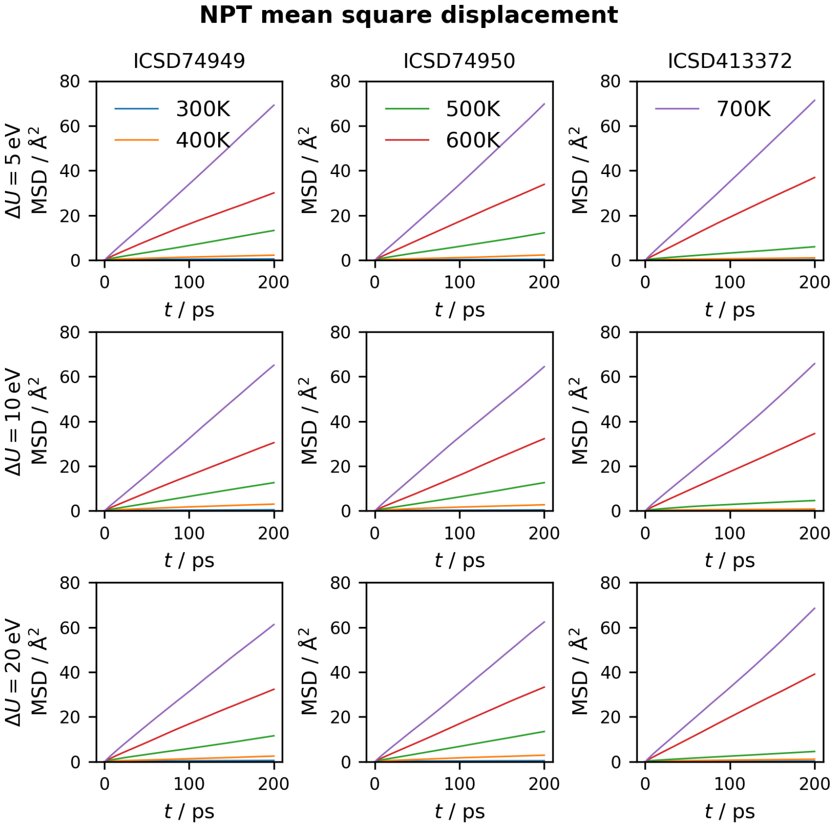

Figure 5.15 – Mean square displacement at temperatures between 100 and 700 K for 750 ps of NPT trajectories with a maximum lag time of 200 ps. The trajectories were produced using the globally optimized force-field with minimum barriers of 5 10 and 20 eV. The MSD is presented for three phases of lithium tantalate described by their ICSD collection ids.

system. However, when comparing the diffusion coefficient of both NVT and NVE trajectories shown in Fig. 5.18, the two Arrhenius plots appear shifted with similar activation energies showing that the mechanisms are slowed down rather than blocked or modified.

Conclusion

The use of the Monte-Carlo sampling of partially occupied structures was demonstrated for lithium tantalate structures. Although the currently implemented mechanism for the site grouping needs updated to be better able to identify true crystallographic sites, potentially through the use of symmetry based detection, the results show that the methodology is able to successfully sample the configurational space of the structure to yield Boltzmann distributed samples that can be used for the training of force-fields.

The use of purely random displacement to mimic thermal displacement during the trajectory works successfully as a first approximation though improvement could be achieved

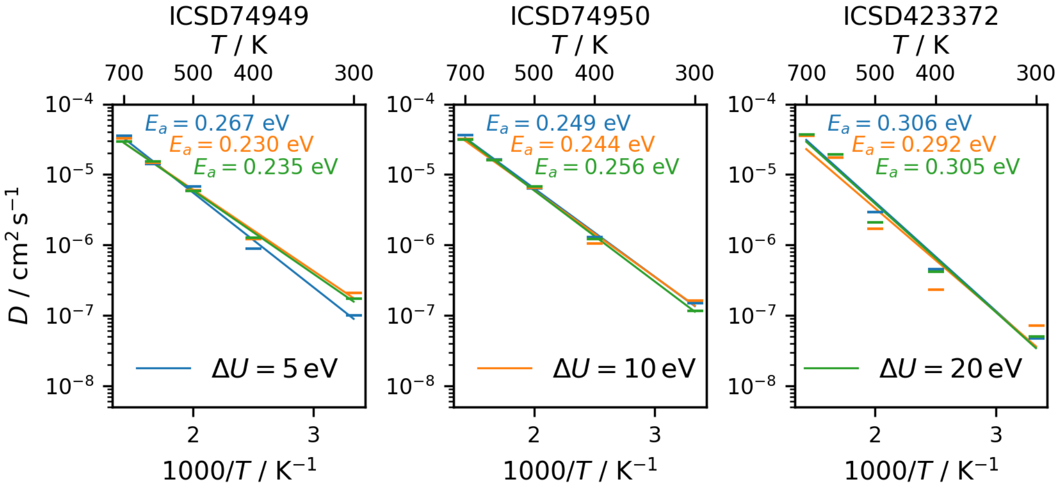

Figure 5.16 – Comparison of the diffusion coefficients corresponding to the mean square displacements shown in Fig. 5.15 with their respective activation energies.

through the use of the structure's phonons to provide a better approximation of the expected displacements.

The use of a synthetic training set for the parametrization of the force-field parameters was successfully demonstrated in the case of lithium tantalate crystals. The resulting force-field is able to reproduce structural parameters of the rhombohedral phases within reasonable margin of error in a relatively short time. The resulting force-fields is also able to reproduce diffusion values and activation energies at par with previous description of first-principle and force-field molecular dynamics.

Despite the overall success of the force-field training in the case of the rhombohedral structures. The procedure failed at successfully stabilize and reproduce the correct structure for the trigonal phase. As both phases have been used to describe the same system, this could be due to a difficulty to stabilize both systems with a unique force-field as a result of their close structural similarity.

Although the results presented here for lithium tantalates are only partially successful, considering the issues to correctly model the rhombohedral phase, the methodology still remains an improvement over supervised training methods. Furthermore the it is likely that such issue would not occur in systems such as LLZO where the phase transition is dictated by entropic effects rather than a deeper change in structure and interactions.

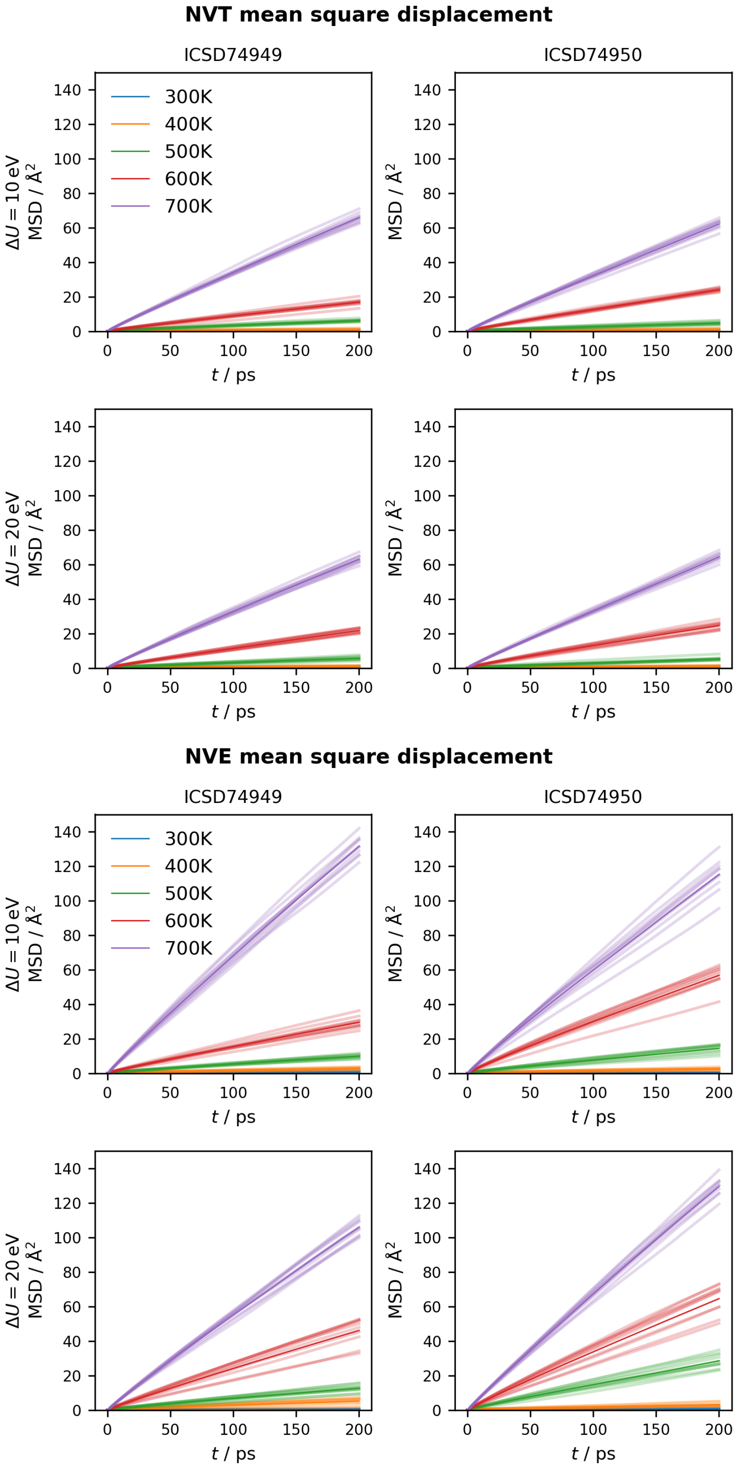

Figure 5.17 – Mean square displacement at temperatures between 100 and 900 K for 750 ps of NVT and NVE trajectories. The trajectories were produced using the globally optimized force-field with minimum barriers of 10 and 20 eV.

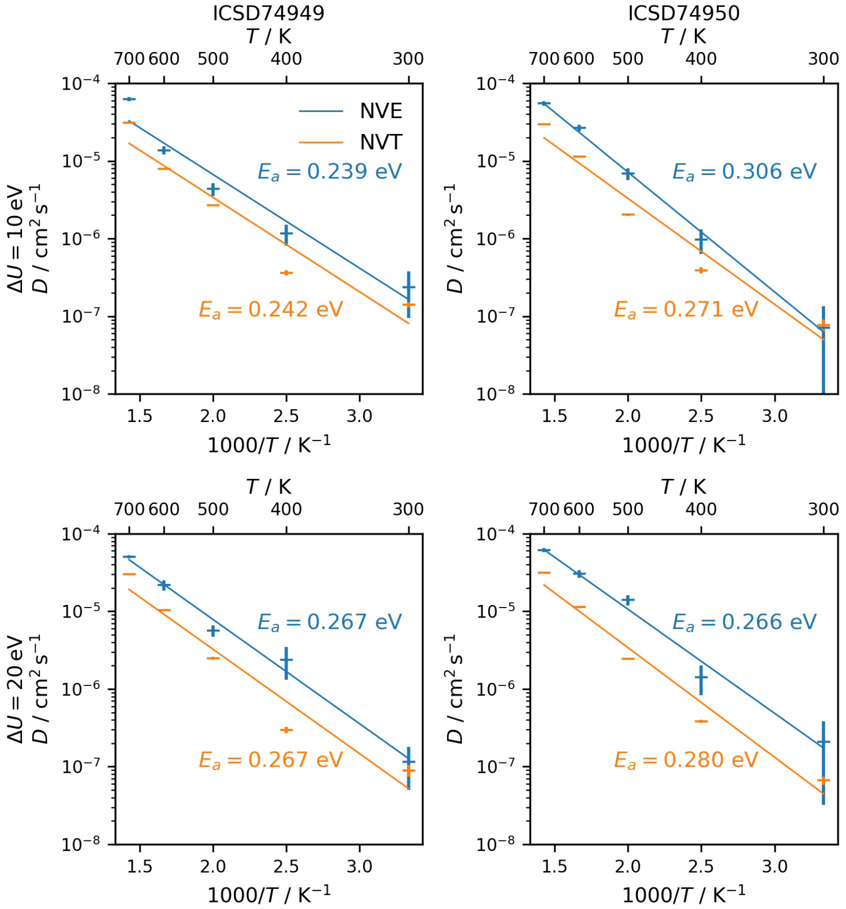

Figure 5.18 – Diffusion coefficients at temperatures between 100 and 900 K computed from NPT trajectories of 750 ps. The trajectories were produced using the globally optimized forcefield with minimum barriers of 10 and 20 eV.

6 Comparison of computational methods for the electrochemical stability window of solid-state electrolyte materials

Although conductivity remains on of the key element of a good solid-state electrolyte, other factors come into play. In particular its electrochemical stability is an important aspect that determines its potential stability against electrodes and the probability of creating a solid-electrolyte interphase (SEI) that could lower the overall conductivity of the electrochemical cell.

In this article, three computational methods used to evaluate the electrochemical stability window of solid-state electrolytes were reviewed, the HOMO-LUMO method, the stoichiometry stability method and the phase stability method. All three methods were implemented for material screening as AiiDA workflows. The results of all three methods for several solid-state electrolytes is compared.

The version presented is a preprint version of the article published in the Journal of Materials Chemistry A [138]. The supplementary information of the article are included in Appendix A.1.

6.1 Introduction

Solid-state electrolyte (SSE) materials, i.e. materials that provide ionic but no electronic conductivity, are key components of all-solid-state batteries (ASSBs), which are regarded as promising candidates for next generation Li- or Na-ion batteries. State-of-the-art Li-ion batteries are based on liquid organic electrolytes, which are flammable and furthermore thermodynamically unstable against the low-potential electrode, e.g. metallic Li. Their operation is possible only because of the formation of a passivating layer between the electrode and the liquid electrolyte, termed the “solid electrolyte interphase”[1] (SEI) [139, 140]. In comparison to liquid electrolytes, many SSE materials offer superior stability against reduction and oxidation. Nevertheless, only few SSE materials provide true thermodynamic stability against the corresponding metallic anode [141, 142]. Therefore, interfacial stability between the electrode and the solid-state electrolyte is a focus topic in current ASSB research [143, 144]. For many SSE materials, a passivating interphase layer forms between the metallic low-potential electrode and the SSE [145, 141, 143, 144], which consists of SSE decomposition products, similar to the SEI layer in liquid electrolyte Li-ion cells. Although such a “metal–solid electrolyte interphase (MSEI) layer” [145] can render an ASSB meta-stable due to passivation and also provide a certain ionic conductivity to sustain battery operation, the battery performance will be deteriorated because of the reduced ionic conductivity of the interphase layer. The same conclusion holds for passivating interphase layers between SSE and high-potential electrode [142]. Thus, for ASSBs to unfold their full potential, stability of the SSE against both electrodes is desirable to avoid the formation of interphase layers.

The interface stability properties of an SSE material in contact with an electrode are best described by its electrochemical stability window. We refer to “electrochemical stability” as the stability of an SSE material against *reactions that contain transfer of mobile species atoms*, e.g. Li- or Na-atoms. It must be emphasized that only the transfer of *neutral* atoms represents an SSE instability. In contrast, the transfer of mobile species ions, e.g. Li^+ or Na^+, across the electrode–SSE interface is part of the normal battery operation and it does not alter the SSE composition or structure.

This definition of “electrochemical stability” comprises both potential-driven SSE instability processes in a closed-circuit cell and direct reactions between SSE and electrodes under exchange of mobile species atoms that can also proceed in an open-circuit cell. In fact, both types of processes are equivalent: In an electrochemical process, the electrode represents an electron reservoir and electron transfer occurs across the electrode–electrolyte interface. If only electrons are transferred, the build-up of charge quickly stops the process. Thus, for an instability reaction to proceed, charge neutrality must be preserved i.e. the electronic charge transfer must be compensated by the movement of mobile ions to/from the instability reaction interface RI, cf. Figure 6.1. In a closed-circuit electrochemical cell, Figure 6.1a, the compensating ions are supplied to interface RI through the SSE by the counter-reaction at the opposite electrode CE. However, in an ASSB the electro-active electrode materials are also ion

---

[1] Strictly speaking, the orignial term was chosen to denote the solid “phase” of the passivating layer with a certain ionic conductivity, i.e. a “solid electrolyte phase” in between the electrode and the liquid electrolyte. Nowadays, however, also the term “solid–electrolyte *interface*” is commonly used for SEI, i.e. the layer at the “interface” between the solid electrode and the liquid electrolyte. The use of the abbreviation SEI allows to neglect these subtle differences in terminology.

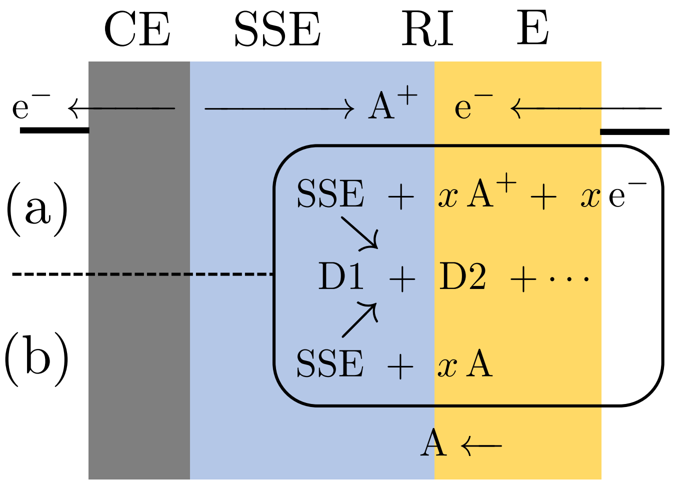

Figure 6.1 – The same SSE instability reaction in a closed-circuit cell (a) and open-circuit cell (b). CE = counter electrode, RI = reaction interface, E = electrode, A = mobile species (Li, Na, …).

reservoirs. Therefore, the compensating ions for the instability reaction can also be provided in an open-circuit ASSB from electrode E itself across the same electrode–SSE interface RI as the electrons. The combination of electron and ion transfer represents a transfer of *neutral* mobile atoms between electrode and SSE, Figure 6.1b.

According to this reasoning, a general electrochemical SSE instability reaction is written

$$\mathrm{SSE} + x\mathrm{A} \longrightarrow \mathrm{D1} + \mathrm{D2} + \cdots \tag{6.1}$$

where A = Li, Na, ... denotes the mobile species within an SSE material and D1, … denotes different decomposition products. The coefficient x can be positive or negative, depending on the direction of A-transfer. Reaction (6.1) represents the overall cell reaction of Figure 6.1. The electrochemical character becomes more obvious from the corresponding half-cell reaction at the electrode–SSE interface RI,

$$\mathrm{SSE} + x\mathrm{A}^{+} + x\mathrm{e}^{-} \longrightarrow \mathrm{D1} + \mathrm{D2} + \cdots \tag{6.2}$$

Thus, for $x > 0$ the instability reaction is an SSE reduction, and for $x < 0$ an SSE oxidation. If an A-metal counter electrode is used, the counter half-cell reaction is simply given by

$$x\mathrm{A} \longrightarrow x\mathrm{A}^{+} + x\mathrm{e}^{-} \tag{6.3}$$

i.e. A-metal oxidation for $x > 0$ or plating for $x < 0$. The equilibrium potential of the electrochemical SSE instability reaction (6.2) versus the reference electrode reaction (6.3) is expressed by the Nernst equation in terms of the Gibbs free energy of the overall cell reaction (6.1), cf.

Supporting Information for derivation,

$$\Phi_{\text{eq}} = -\frac{\Delta G}{e\,x} = -\frac{1}{e}\left(\frac{G_{\text{D1}} + G_{\text{D2}} + \cdots - G_{\text{SSE}}}{x} - G_{\text{A}}\right) \tag{6.4}$$

where G_i denotes the Gibbs free energy of compound i. For $x > 0$ (SSE reduction), reaction (6.2) proceeds if the SSE material is in contact with an electrode potential $\Phi < \Phi_{\text{eq}}$. Vice versa, for $x < 0$ (SSE oxidation), reaction (6.2) proceeds if the SSE material is in contact with an electrode potential $\Phi > \Phi_{\text{eq}}$. The equilibrium potentials of all possible SSE instability reactions of type (6.1) yield an electrochemical series of SSE reduction and oxidation potentials. The limiting SSE reduction potential Φ_{red} is given by the maximum of all equilibrium potentials for reactions with $x > 0$, $\Phi_{\text{red}} = \max(\{\Phi_{\text{eq},i} \,|\, x_i > 0\})$, and the limiting SSE oxidation potential Φ_{ox} by the minimum of all equilibrium potentials for $x < 0$, $\Phi_{\text{ox}} = \min(\{\Phi_{\text{eq},j} \,|\, x_j < 0\})$. For electrode potentials $\Phi_{\text{red}} < \Phi < \Phi_{\text{ox}}$, no reduction or oxidation of the SSE occurs. Therefore, the potential range $[\Phi_{\text{red}}, \Phi_{\text{ox}}]$ is the *electrochemical stability window* of the SSE material.

Different computational methods have been applied to determine the electrochemical stability window. The positions of the electronic HOMO and LUMO states, i.e. the valence and conduction band edges, provide an estimate of the electrochemical stability window [146, 147, 148]. In this approach, the electrode in contact with the SSE is regarded as “electron reservoir” and only electron transfer between electrode and SSE is considered. The “HOMO–LUMO method” allows for a rather quick estimation of the width of the stability window in terms of the electronic band gap. However, its absolute position with respect to a reference electrode is difficult to determine with this methodology [147] because of the dipole at the electrode–SSE interface that shifts the relative positions of electronic states. Furthermore, because the electrode is assumed chemically inert, the HOMO–LUMO gap is considered only an upper bound for the electrochemical stability window [148, 142].

The interface dipole problem is avoided by considering combined electron and ion transfer between SSE and electrode, i.e. transfer of neutral mobile Li- or Na-atoms, as described by reactions (6.1) and (6.2). The dipole does not affect the energies of charge-neutral states. Thus, the absolute position of the stability window w.r.t. a reference potential can be conveniently determined from bulk computations. Two different cases are distinguished corresponding to two different methods to compute the stability window.

The first method considers reactions of type (6.1) in the limit of small x where the only product is the same SSE phase with a changed stoichiometry of the mobile species. Accordingly, we denote it “stoichiometry stability method” in the following. Such processes are similar to Li-insertion or Li-extraction reactions in electro-active electrode materials. Whereas in the latter case such reactions are part of the required function, for an SSE they represent an instability. This method was applied to compute the Li-insertion potentials of various garnet-type Li-SSE materials [149], the Li-insertion and Li-extraction potentials of LGPS [150], and the Na-extraction potentials of various Na-SSE materials [151]. A similar defect chemistry-derived perspective on SSE stability was adopted to investigate the instability of $Li_4P_2S_6$ SSE against metallic Li [152]. Although this type of instability reaction is sometimes referred to as “topochemical” or “topotactic”, we believe that this terminology must be used with care, because, strictly speaking, the latter terms denote an insertion reaction “that results in significant structural modifications to the host”, as defined by IUPAC [153]. In contrast, apart from some local relaxation, the SSE structure is usually considered unchanged when computing the insertion/extraction potentials of mobile species by filling/generating vacancies within the SSE host structure.

On the contrary, the “phase stability method” considers reactions of type (6.1) that result in major decomposition of the SSE phase into several different product phases. This is typically done by constructing the grand canonical phase diagram of the SSE and identifying the critical values of the mobile species chemical potential that define the limiting SSE reduction and oxidation potentials [154, 148, 141]. Because the phase stability method takes into account a set of instability reactions that is disjoint from the stoichiometry stability method, the corresponding stability windows are complementary in the sense that the overall electrochemical stability window of an SSE material is the intersection of the stoichiometry stability window and the phase stability window. It is commonly assumed that the phase stability window is generally narrower than the stoichiometry stability window [151], so that the overall stability window is determined by the former. However, to the best of our knowledge, no rigorous proof for this assumption exists to date. In contrast to the HOMO–LUMO method, both the stoichiometry stability method and the phase stability method yield a reliable absolute position of the electrochemical stability window w.r.t. a reference electrode potential, however at the expense of an increased computational effort.

In the present work, we analyse the relation between the different methods with a focus on the stoichiometry stability method. We provide computational implementations in an open-source repository and we compare the results for a set of relevant Li- and Na-SSE materials.

6.2 Methodology

In the following, we indicate with A = Li, Na, . . . , the mobile species within an SSE material. We first discuss the stoichiometry stability method, then its connection with the HOMO–LUMO method, and finally the phase stability method.

6.3 Stoichiometry stability window

We denote as A_nM the stable composition for a unit cell of an SSE material, where the meaning of “stable” is further specified below. As explained in the Introduction, the stoichiometry stability method considers A-insertion/extraction reactions to/from the SSE structure,

$$\epsilon \mathrm{A} + \mathrm{A}_n\mathrm{M} \longrightarrow \mathrm{A}_{\mathrm{n}+\epsilon}\mathrm{M} \tag{6.5}$$

$$\mathrm{A}_n\mathrm{M} \longrightarrow \mathrm{A}_{\mathrm{n}-\epsilon}\mathrm{M} + \epsilon \mathrm{A} \tag{6.6}$$

where ϵ is small compared to n. The critical difference between these instability processes and the transfer of A^+ ions during normal battery operation is the fact that the former change the SSE stoichiometry and the oxidation state of certain species in the M-matrix. They represent redox-reactions between SSE and the respective electrode material: SSE reduction (6.5) and SSE oxidation (6.6).

For a general SSE stoichiometry $\mathrm{A}_{n+z}\mathrm{M}$ that deviates by z from the stable composition, reactions (6.5) and (6.6) read

$$\mathrm{A}_{n+z}\mathrm{M} \pm \epsilon \mathrm{A} \longleftrightarrow \mathrm{A}_{n+(z\pm\epsilon)}\mathrm{M} \tag{6.7}$$

The equilibrium potential Φ_{eq} of reaction (6.7) vs. the reference potential of the A-metal oxidation process (6.3) is a function of the deviation z from the stable stoichiometry, and, according to equation (6.4), it is given by

$$\Phi_{\mathrm{eq}}(z) = -\frac{1}{e}\left(\frac{G_{\mathrm{A}_{n+(z\pm\epsilon)}\mathrm{M}} - G_{\mathrm{A}_{n+z}\mathrm{M}}}{\pm\epsilon} - G_{\mathrm{A}}\right) \tag{6.8}$$

$$= -\frac{1}{e}\left(\mu^{\mathrm{A}}_{\mathrm{SSE}}(z) - \mu^{\mathrm{A}}_{\mathrm{A}}\right) \tag{6.9}$$

Here, $\mu^{\mathrm{A}}_{\mathrm{A}} = G_{\mathrm{A}}$ is the chemical potential of A-metal, i.e. its Gibbs free energy per atom, and $\mu^{\mathrm{A}}_{\mathrm{SSE}}(z)$ corresponds to the chemical potential of neutral species A in the SSE composition $\mathrm{A}_{n+z}\mathrm{M}$,

$$\mu^{\mathrm{A}}_{\mathrm{SSE}}(z) = \lim_{\epsilon\to 0}\frac{G_{\mathrm{A}_{n+(z+\epsilon)}\mathrm{M}} - G_{\mathrm{A}_{n+z}\mathrm{M}}}{\epsilon} = \frac{\mathrm{d}G}{\mathrm{d}z} \tag{6.10}$$

which is equal to the derivative of the Gibbs free energy $G(z) := G_{\mathrm{A}_{n+z}\mathrm{M}}$ as a function of the stoichiometry deviation z. Equation (6.8) is identical to the general relation for the A-insertion potential of electro-active battery materials [155, 156, 157].

In general, the stable SSE composition $\mathrm{A}_n\mathrm{M}$ corresponds to a stoichiometry where all constituting ions are formally in an electronic closed-shell configuration. Consequently, SSE materials have a band gap $E^{\mathrm{LUMO}}_{\mathrm{A}_n\mathrm{M}} - E^{\mathrm{HOMO}}_{\mathrm{A}_n\mathrm{M}} > 0$ and are electronic isolators as required for their function as electrolyte. There exists a qualitative difference between adding A to and extracting A from the stable composition $\mathrm{A}_n\mathrm{M}$: The electrons of added A populate LUMO states of $\mathrm{A}_n\mathrm{M}$, whereas the electrons of extracted A are removed from HOMO states of $\mathrm{A}_n\mathrm{M}$. Therefore, the stable stoichiometry n separates two distinct energetic manifolds with the consequence that the chemical potential $\mu^{\mathrm{A}}_{\mathrm{SSE}}(z)$ has a discontinuity at $z = 0$ with $\lim_{z\to 0^+}\mu^{\mathrm{A}}_{\mathrm{SSE}}$ being strictly larger than $\lim_{z\to 0^-}\mu^{\mathrm{A}}_{\mathrm{SSE}}$. Consequently, we obtain two different equilibrium potentials: The potential of A-insertion (SSE reduction) into the stable SSE stoichiometry A_nM,

$$\Phi_{\text{red}}^{\text{stoi}} = -\frac{1}{e}\left(\lim_{z\to 0^+}\mu_{\text{SSE}}^{\text{A}} - \mu_{\text{A}}^{\text{A}}\right) = -\frac{1}{e}\left(\left.\frac{\mathrm{d}G}{\mathrm{d}z^+}\right|_{z=0} - \mu_{\text{A}}^{\text{A}}\right) \tag{6.11}$$

and the potential of A-extraction from the stable SSE stoichiometry A_nM,

$$\Phi_{\text{ox}}^{\text{stoi}} = -\frac{1}{e}\left(\lim_{z\to 0^-}\mu_{\text{SSE}}^{\text{A}} - \mu_{\text{A}}^{\text{A}}\right) = -\frac{1}{e}\left(\left.\frac{\mathrm{d}G}{\mathrm{d}z^-}\right|_{z=0} - \mu_{\text{A}}^{\text{A}}\right) \tag{6.12}$$

For electrode potentials $\Phi_{\text{red}}^{\text{stoi}} < \Phi < \Phi_{\text{ox}}^{\text{stoi}}$, the SSE stoichiometry is stable and fixed at A_nM, and the valencies of the SSE constituent ions remain constant. Therefore, we call the potential range $[\Phi_{\text{red}}^{\text{stoi}}, \Phi_{\text{ox}}^{\text{stoi}}]$ the *stoichiometry stability window* of the SSE material.

Two simple models that grasp the essential behaviour of the SSE A-stoichiometry as a function of the electrode potential are presented in the Supporting Information. Similar models exist for the Li-insertion into electro-active materials [158]. The resulting SSE stoichiometry vs. electrode potential curves are plotted in Figure 6.2 for generic values of the model parameters given in the Supporting Information. Within $[\Phi_{\text{red}}^{\text{stoi}}, \Phi_{\text{ox}}^{\text{stoi}}]$, the A-stoichiometry is fixed at n. Outside the stoichiometry stability window, the SSE stoichiometry quickly changes by inserting (for $\Phi < \Phi_{\text{red}}^{\text{stoi}}$) or extracting (for $\Phi > \Phi_{\text{ox}}^{\text{stoi}}$) A-atoms. In this region, the behaviour of the A-stoichiometry is determined by the configurational entropy of A-site occupation, which produces a steep step of the stoichiometry within a narrow potential range: The SSE turns into an electro-active material with a plateau of the equilibrium potential as a function of A-stoichiometry, cf. Figure 6.2 rotated by 90°.

6.3.1 Stoichiometry stability window: Relevance for ASSB application

The stable stoichiometry A_nM corresponds to an electronic insulator with a band gap. However, addition of A to the material introduces electrons into the conduction band. Similarly, extraction of A generates electron holes in the valence band. Therefore, even small stoichiometry changes of the SSE material can significantly increase its electronic conductivity with the consequence of an electronic short circuit between anode and cathode via the SSE. Electronic short-circuit of the electrodes causes self-discharge of an ASSB via combined electron and ion migration through the SSE. Of course, the extent of electronic conductivity increase due to A-stoichiometry changes is strongly material-specific, because it depends on whether the additional electronic charge carriers occupy mobile states within the conduction or valence band, or whether they get trapped by in-gap states.

Furthermore, local changes of the SSE stoichiometry at one or both of the SSE–electrode interfaces can result in a chemical short circuit between the electrodes and a diffusion-driven self-discharge of the ASSB. At both contact interfaces, the SSE stoichiometry equilibrates with the respective electrode potential. If both the anode potential Φ_A and the cathode potential Φ_C lie inside the potential window $[\Phi_{\text{red}}^{\text{stoi}}, \Phi_{\text{ox}}^{\text{stoi}}]$, the SSE stoichiometry deviation z is equal to zero

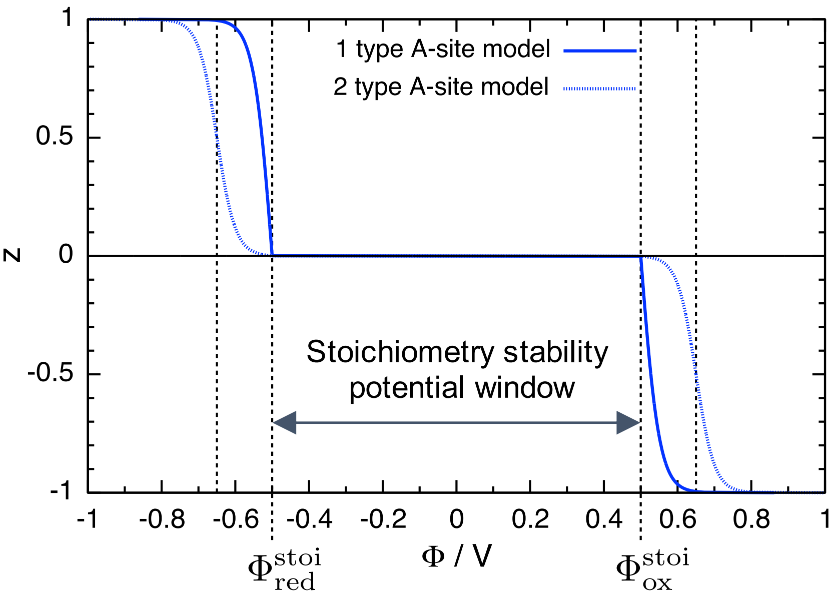

Figure 6.2 – The stoichiometry deviation z in the general SSE composition $A_{n+z}M$ as a function of the electrode potential Φ as derived from two simple models for generic values of the model parameters, cf. Supporting Information.

everywhere, cf. Figure 6.2. If, however, $\Phi_A < \Phi_{\mathrm{red}}^{\mathrm{stoi}}$ and/or $\Phi_C > \Phi_{\mathrm{ox}}^{\mathrm{stoi}}$, the SSE stoichiometry deviation z_A at the anode contact interface will be different from the value z_C at the cathode contact interface, with $z_A > z_C$. This causes an A-concentration gradient across the SSE layer and triggers diffusion of neutral A-species from the anode side to the cathode side. This mechanism can also proceed at open-circuit and result in self-discharge of the ASSB via mobile species diffusion.

The speed of the diffusion self-discharge depends critically on the value of the diffusion coefficient of *neutral* A within the non-stoichiometric $A_{n+z}M$ SSE phase. We consider an ASSB with an SSE layer thickness of $d_{\mathrm{SSE}} = 100\,\mu$m. Assuming a small relative SSE stoichiometry gradient of $\Delta z/n = 0.05$ between the anode interface and the cathode interface, we estimate a gradient of mobile ion density $\Delta n_A/d_{\mathrm{SSE}} = n_A\,(\Delta z/n)/d_{\mathrm{SSE}} = 5 \times 10^{21}\,\mathrm{cm}^{-4}$ for a typical mobile ion density $n_A = 10^{21}\,\mathrm{cm}^{-3}$. According to Fick's law of diffusion, an A-diffusion coefficient $D_A = 10^{-7}\,\mathrm{cm}^2\mathrm{s}^{-1}$ yields an A-diffusion flux of $|j_A| = D_A \Delta n_A/d_{\mathrm{SSE}} = 5 \times 10^{14}\,\mathrm{cm}^{-2}\mathrm{s}^{-1}$, which is equivalent to an electrical self-discharge current of $|j_{el}| = e|j_A| \approx 0.08\,\mathrm{mA\,cm}^{-2}$. A typical Li-ion battery contains approx. 20 mg cm^{-2} active cathode material with specific capacitance of approx. 150 mAh/g, yielding an area-specific battery capacitance of approx. 3 mAh cm^{-2}. Such a battery would be entirely self-discharged within approx. 1.5 days. Even for $D_A = 10^{-8}\,\mathrm{cm}^2\mathrm{s}^{-1}$, a complete self-discharge time of approx. two weeks is obtained.

Values of 10^{-8}–$10^{-7}\,\mathrm{cm}^2\mathrm{s}^{-1}$ are common for the *ionic* diffusion coefficient in SSE materials with high ionic conductivity. However, ionic diffusion of A^+ is different from the diffusion of *neutral* A considered here: The latter is equivalent to a parallel diffusion of both A^+ ions and electrons as described by Maier [159]. If the electronic mobility is large, the diffusion coefficient of neutral A will be essentially equal to the ionic one. This is clearly not fulfilled for an SSE material in its stable stoichiometry which is an electronic isolator. But, as discussed above, the electronic conductivity of the non-stoichiometric SSE can be significantly increased. Thus, whether diffusion self-discharge can be relevant depends on the SSE material at hand and on the electronic conductivity properties of its non-stoichiometric phase.

6.3.2 Stoichiometry stability window: Computational Implementation

We implemented the stoichiometry stability method in the Python workflow environment AiiDA [160] utilizing methods of the Python Materials Genomics (pymatgen) module [161]. We provide the stoichiometry stability plug-in in the ZRL-AiiDA-toolbox repository on GitHub [162].

The potential limits $\Phi^{\mathrm{stoi}}_{\mathrm{red}}$ and $\Phi^{\mathrm{stoi}}_{\mathrm{ox}}$ of the stoichiometry stability window are given by equations (6.11) and (6.12), respectively. We choose a large supercell of the SSE structure with a stable stoichiometry $\mathrm{A_NM}$ and we approximate the derivatives of the Gibbs free energy by the energy differences of adding/removing one A atom to/from the supercell, respectively, $\left.\frac{\mathrm{d}G}{\mathrm{d}z^\pm}\right|_{z=0} \approx \pm(E^{\mathrm{min}}_{\mathrm{A_{N\pm1}M}} - E^{\mathrm{min}}_{\mathrm{A_NM}})$. Here, we neglect the pV term, entropic contributions, and thermal contributions to the internal energy, which is well justified if an error of $\pm 0.1\,\mathrm{V}$ is acceptable on the calculated stability potential window. SSE materials contain both occupied and unoccupied A-sites. Every distribution i of the A-atoms over the available A-sites has a distinct energy. We take the minimum over all configurations, i.e. the configurational ground-state energies $E^{\mathrm{min}}_{\mathrm{A_NM}} = \min(\{E^{i}_{\mathrm{A_NM}} \mid i \in \mathrm{conf}_{\mathrm{A_NM}}\})$ and analogously $E^{\mathrm{min}}_{\mathrm{A_{N\pm1}M}}$. Again, the contribution of thermally activated configurations can be neglected if an error of $\pm 0.1\,\mathrm{V}$ is acceptable. Then the potential limits read

$$\Phi^{\mathrm{stoi}}_{\mathrm{red}} = -\frac{1}{e}(E^{\mathrm{min}}_{\mathrm{A_{N+1}M}} - E^{\mathrm{min}}_{\mathrm{A_NM}} - E^{\mathrm{A}}_{\mathrm{A}}) \tag{6.13}$$

$$\Phi^{\mathrm{stoi}}_{\mathrm{ox}} = -\frac{1}{e}(E^{\mathrm{min}}_{\mathrm{A_NM}} - E^{\mathrm{min}}_{\mathrm{A_{N-1}M}} - E^{\mathrm{A}}_{\mathrm{A}}) \tag{6.14}$$

Here, the chemical potential of A-metal $\mu^{\mathrm{A}}_{\mathrm{A}}$, which is equal to the Gibbs free energy per atom, is approximated by the energy per atom of the relaxed A-metal structure, $\mu^{\mathrm{A}}_{\mathrm{A}} \approx E^{\mathrm{A}}_{\mathrm{A}}$.

Monte Carlo sampling. An efficient sampling method is required to find the configurational ground-state energies, because a complete sampling of all configurations is not possible, and because the energies can vary significantly between different configurations. We use a Monte Carlo sampling algorithm based on purely electrostatic Ewald energies to identify a number of candidate configurations for the configurational ground-state. A random initial distribution of A-atoms over the available A-sites is generated according to the occupancies defined in the SSE material .cif-file. Every Monte Carlo step consists of swapping a randomly chosen A-atom to an unoccupied A-site. The swap is accepted according to the Metropolis criterion with a probability $p = \min(1, \exp(-\Delta E/(k_B T)))$, where ΔE is the Ewald energy difference of the swap, k_B is the Boltzmann constant, and T is the temperature chosen. The corresponding Ewald energies are computed from the formal charges of each species given in the .cif-file using the pymatgen Python module [161]. The Monte Carlo process runs until equilibration is reached.

We then use the final configurations of approximately 30 independent Monte Carlo runs to compute their density functional theory (DFT) energies including structural relaxation. Finally, the minimum of the relaxed DFT energies is determined. The entire process is performed separately for the three compositions $\mathrm{A_NM}$, $\mathrm{A_{N+1}M}$, and $\mathrm{A_{N-1}M}$ to determine $E^{\mathrm{min}}_{\mathrm{A_NM}}$, $E^{\mathrm{min}}_{\mathrm{A_{N+1}M}}$, and $E^{\mathrm{min}}_{\mathrm{A_{N-1}M}}$, respectively.

The sampling method is based on the assumption that configurations with minimum DFT energies also have electrostatic Ewald energies close to the minimum, which has also been used by other authors [148]. To further verify this assumption, we plot Ewald energies vs. DFT energies in Supporting Information Figure S2 for the SSE materials LGPS, LIPON, LLZO, LLTO, LATP, LISICON, and NASICON. For each of the compositions $\mathrm{A_{N-1}M}$, $\mathrm{A_NM}$, and $\mathrm{A_{N+1}M}$, we selected 100 random configurations. A linear correlation is observed in most cases. Typical slopes of the order of 10 indicate the dielectric screening properties of the materials, which are neglected in Ewald energies. Based on the slopes and the scattering of the energy–energy plots, we chose a temperature of 5000 K for the Monte Carlo runs.

DFT details. DFT computations were performed using the Quantum ESPRESSO software package [163]. The generalized gradient approximation (GGA) of the exchange-correlation functional in PBE form [164] was used along with pseudopotentials from the SSSP Efficiency library[165, 166]. We chose the double of the cutoff values suggested by SSSP for wavefunctions and density. Because of the usage of supercells, k-point sampling was restricted to the Γ-point. The convergence of the results was confirmed by certain computations using a 2x2x2 k-point mesh. If possible, the magnetization, i.e. the population difference Δn between up- and down-spin, was allowed to relax. In case of failure, it was fixed at $\Delta n = 0$ for $\mathrm{A_NM}$ (closed-shell) and at $\Delta n = 1$ for $\mathrm{A_{N\pm1}M}$ (single unpaired electron). We further used Marzari-Vanderbilt smearing [167] with 0.005 Ry.

We also tested the influence of hybrid functionals using HSE06 [168] with an exact exchange fraction of 0.25 together with SG15 ONCV pseudopotentials [169, 170]. We used a wavefunction cutoff of 100 Ry for LATP and LLTO, and 60 Ry for LLZO (because of its very large cell). The density cutoff was four times the wavefunction cutoff.

6.3.3 Stoichiometry stability window and HOMO–LUMO method

The SSE stoichiometry stability window is determined by the discontinuity in the chemical potential of neutral A at the stable stoichiometry. This discontinuity originates from the electronic HOMO–LUMO gap (or band gap). Therefore, a very close relation exists between the stoichiometry stability method and the HOMO–LUMO method. In fact, the chemical potential of neutral A in the SSE phase, cf. equation (6.10), is equal to the sum of e$^-$ and A$^+$ chemical potentials,

$$\mu_{\mathrm{SSE}}^{\mathrm{A}} = \frac{\mathrm{d}G}{\mathrm{d}z} = \frac{\partial G}{\partial z_{\mathrm{e}^-}} + \frac{\partial G}{\partial z_{\mathrm{A}^+}} = \mu_{\mathrm{SSE}}^{\mathrm{e}^-} + \mu_{\mathrm{SSE}}^{\mathrm{A}^+} \tag{6.15}$$

where z, z_{e^-}, and z_{A^+} are the changes in neutral A, e$^-$, and A$^+$ numbers, respectively. The ionic chemical potential $\mu_{\mathrm{SSE}}^{\mathrm{A}^+}$ essentially contains the interaction between A$^+$ and the SSE crystal field, i.e. the Madelung potential of the A-sites [156]. Therefore, we assume that the ionic chemical potential is continuous at the stable SSE composition, $\lim_{z\to 0^-} \mu_{\mathrm{SSE}}^{\mathrm{A}^+} = \lim_{z\to 0^+} \mu_{\mathrm{SSE}}^{\mathrm{A}^+}$. From equations (6.11) and (6.12), we then obtain for the *width of the stoichiometry stability window*

$$\begin{aligned}\Delta\Phi^{\mathrm{stoi}} = \Phi_{\mathrm{ox}}^{\mathrm{stoi}} - \Phi_{\mathrm{red}}^{\mathrm{stoi}} &= -\frac{1}{e}\left(\lim_{z\to 0^-} \mu_{\mathrm{SSE}}^{\mathrm{A}} - \lim_{z\to 0^+} \mu_{\mathrm{SSE}}^{\mathrm{A}}\right) \\ &= -\frac{1}{e}\left(\lim_{z\to 0^-} \mu_{\mathrm{SSE}}^{\mathrm{e}^-} - \lim_{z\to 0^+} \mu_{\mathrm{SSE}}^{\mathrm{e}^-}\right) \\ &= \frac{1}{e}\left(\mathrm{IP}_{\mathrm{SSE}} - \mathrm{EA}_{\mathrm{SSE}}\right)\end{aligned} \tag{6.16}$$

where we used the definitions of ionization potential $\mathrm{IP} = -\lim_{z\to 0^-} \mu_{\mathrm{SSE}}^{\mathrm{e}^-}$ and electron affinity $\mathrm{EA} = -\lim_{z\to 0^+} \mu_{\mathrm{SSE}}^{\mathrm{e}^-}$ [171]. We see that the width of the stoichiometry stability window is equal to the fundamental gap of the SSE [172]. If the potential limits are computed from finite A number differences as in equations (6.13) and (6.14), relation (6.16) remains approximately valid up to small energetic differences between addition/removal of one A$^+$ ion and interaction terms between the added/removed A$^+$ and e$^-$.

An estimation of the fundamental gap from the HOMO–LUMO gap of Kohn-Sham DFT orbitals is non-trivial. The HOMO–LUMO gap $\Delta E_{\mathrm{HL}}^{\mathrm{N}} = E_{\mathrm{LUMO}}^{\mathrm{N}} - E_{\mathrm{HOMO}}^{\mathrm{N}}$ of the system with stable A-stoichiometry N gives a very poor estimate of the fundamental gap, because of a discontinuity in the DFT exchange-correlation (xc) potential [172, 173, 174]. Long-range corrected DFT xc-functionals are known to approximately fulfil Koopmans' theorem and yield much better estimates of IP and EA from Kohn-Sham HOMO and LUMO energies [174]. We therefore also compute $\Delta E_{\mathrm{HL}}^{\mathrm{N}}$ for a few materials using hybrid functional DFT, cf. details given above for the stoichiometry stability method.

6.4 Phase stability window

The electrochemical stability of an SSE material against major decomposition of the SSE phase is typically assessed by computing its A-grand canonical phase diagram [154, 148, 141]. The electro-active material of the electrode represents an A-reservoir. The corresponding

A-chemical potential μ^{A} is fixed by the electrode potential Φ via the relation $\Phi = -(\mu^{\mathrm{A}} - \mu^{\mathrm{A}}_{\mathrm{A}})/e$, which is analogous to equation (6.9), with the A-metal reference chemical potential $\mu^{\mathrm{A}}_{\mathrm{A}}$.

We compute the phase stability window of an SSE in an equivalent, but slightly different way. For an SSE material with composition $\mathrm{A}_a\mathrm{B}_b\mathrm{C}_c\mathrm{D}_d$, we consider all known compounds that contain one or several of the elements A, B, C, or D, and we construct all possible SSE decomposition reactions of type (6.1). For each decomposition reaction i, we then compute the corresponding equilibrium potential $\Phi_{\mathrm{eq},i}$ from equation (6.4). Tolerating errors of the order of 0.1 V on the equilibrium potentials, we approximate the Gibbs free energies G by the energies E after structural relaxation. The equilibrium potentials are grouped according to the type of reaction, i.e. either SSE reduction if $x_i > 0$, or SSE oxidation if $x_i < 0$. If $x_i = 0$, the decomposition reaction is not electrochemical, because it does not involve electron and ion transfer, cf. Introduction. Then, the potential limits of the phase stability window $[\Phi^{\mathrm{phase}}_{\mathrm{red}}, \Phi^{\mathrm{phase}}_{\mathrm{ox}}]$ are given by $\Phi^{\mathrm{phase}}_{\mathrm{red}} = \max(\{\Phi_{\mathrm{eq},i} \,|\, x_i > 0\})$ and $\Phi^{\mathrm{phase}}_{\mathrm{ox}} = \min(\{\Phi_{\mathrm{eq},j} \,|\, x_j < 0\})$.

The combinatorics of relevant decomposition reactions $\mathrm{SSE} \rightarrow d_1\,\mathrm{D1} + \cdots + d_m\,\mathrm{D}m - x\mathrm{A}$ are restricted, because the maximum number m of decomposition products in a given reaction is equal to the number of distinct elements in the SSE minus one. We represent the SSE and all products by composition vectors with one dimension for each distinct element, e.g. an SSE material $\mathrm{A}_a\mathrm{B}_b\mathrm{C}_c\mathrm{D}_d$ by the vector (a, b, c, d). Then the reaction stoichiometry coefficients d_1, $\ldots$, d_m, and $-x$ are equal to the expansion coefficients of the SSE vector (a, b, c, d) in a basis given by the set of product vectors, including the vector $(1, 0, 0, 0)$ representing A-metal. The total number of basis vectors is equal to the dimension, i.e. the number of distinct elements. Because the vector representing A-metal is always present, the number m of additional basis vectors is equal to the number of distinct elements minus one. Any reaction with more than m decomposition products can be written as a superposition of such “basic” reactions, which proceed independently. Therefore, it is sufficient to consider only basic SSE decomposition reactions. This restriction is analogous to Gibbs’ phase rule that restricts the number of coexisting equilibrium phases. Furthermore, only decomposition reactions with stoichiometry coefficients $d_j \geq 0$ must be taken into account, because the only reactants are the SSE and, in case of SSE reduction, the A-metal reference.

Computational details. We provide our implementation of the phase stability method as an AiiDA [160] plug-in in the ZRL-AiiDA-toolbox repository on GitHub [162]. For every investigated SSE material, we considered all possible decomposition products from the Inorganic Crystal Structure Database (ICSD) [175, 176]. For every product, we created a supercell and computed the DFT energy after structural relaxation. The same DFT parameters were used as given above for the stoichiometry stability method. For products with partial occupancies, we used the Ewald energy-based Monte Carlo algorithm to generate a favourable configuration, cf. implementation of the stoichiometry stability method.

Material	Origin of .cif	Structure	Supercell composition
LGPS	ICSD-188886 Ref. [178]	tetragonal	$Li_{40}Ge_4P_8S_{48}$
LIPON	Ref. [177]	orthorhombic	$Li_{45}P_{24}O_{51}N_{21}$
LLZO	ICSD-422259 Ref. [179]	cubic	$Li_{56}La_{24}Zr_{16}O_{96}$
LLTO	ICSD-82671 Ref. [180]	tetragonal	$Li_6La_{10}Ti_{18}O_{54}$
LATP	ICSD-253240 Ref. [181]	hexagonal	$Li_{16}Al_4Ti_{20}P_{36}O_{144}$
LISICON	ICSD-100169 Ref. [182]	orthorhombic	$Li_{82}Zn_7Ge_{24}O_{96}$
NASICON	ICSD-473 Ref. [183]	monoclinic	$Na_{24}Zr_{16}Si_{16}P_8O_{96}$

Table 6.1 – Input .cif-files, structures, and supercells for the investigated SSE materials.

6.5 Results and Discussion

Comparison of stoichiometry stability and phase stability windows. We compare our computed stoichiometry stability windows with published [141] phase stability windows for a set of important Li-SSE materials: $Li_{10}GeP_2S_{12}$ (LGPS), O-doped Li_2PO_2N (LIPON), $Li_7La_3Zr_2O_{12}$ (LLZO), $Li_{0.33}La_{0.56}TiO_3$ (LLTO), $Li_{1.33}Al_{0.33}Ti_{1.67}(PO_4)_3$ (LATP), and $Li_{3.42}Zn_{0.29}GeO_4$ (LISICON). Because the precise LIPON composition Li_2PO_2N does not contain accessible Li-vacancies [177], we generated Li-vacancies by slightly changing the composition to $Li_{1.875}PO_{2.125}N_{0.875}$. In addition, we investigated the Na-SSE material $Na_3Zr_2Si_2PO_{12}$ (NASICON), for which we computed also the phase stability window using our own implementation. Table 6.1 summarizes the origin of .cif-files, the corresponding crystal structures, and the supercell compositions used in our computations.

To validate our implementation of the phase stability method, we also computed the phase stability windows of LGPS and LLZO and compared the results with the published ones [141]. For LGPS, we obtained a phase decomposition reduction potential of $\Phi^{\text{phase}}_{\text{red, LGPS}} = (1.97 \pm 0.15)\,\text{V}_{\text{vs. Li}}$ and an oxidation potential of $\Phi^{\text{phase}}_{\text{ox, LGPS}} = (1.87 \pm 0.23)\,\text{V}_{\text{vs. Li}}$. Our values for both potentials agree well with the respective values of 1.71 and 2.14 $\text{V}_{\text{vs. Li}}$ previously reported [141]. Within error margins, both potential limits are equal meaning that the phase stability window of LGPS is essentially zero. Errors on the potentials were propagated from an estimated general error of 1.0 eV on the total DFT energy of the supercells. Decomposition reactions with errors $> 1.0\,\text{V}$ on the corresponding equilibrium potentials were excluded. Such large errors are encountered for very small x in equation (6.4), i.e. for decomposition reactions with very little Li-exchange that are close to the 'non-electrochemical' limit.

For LLZO, we obtained a phase decomposition reduction potential of $\Phi^{\text{phase}}_{\text{red, LLZO}} = (0.02 \pm 0.03)\,\text{V}_{\text{vs. Li}}$ and an oxidation potential of $\Phi^{\text{phase}}_{\text{ox, LLZO}} = (2.16 \pm 0.37)\,\text{V}_{\text{vs. Li}}$. Our value for the reduction potential agrees very well with the value of 0.05 $\text{V}_{\text{vs. Li}}$ previously reported [141]. The previously reported value of 2.91 $\text{V}_{\text{vs. Li}}$ for the oxidation potential is slightly larger than our value, but, given the larger error margin, we still regard it as reasonable agreement.

Table 6.2 summarizes the computed stoichiometry stability windows for the investigated SSE materials. Our values of the Li-insertion and extraction potentials of LGPS agree well with

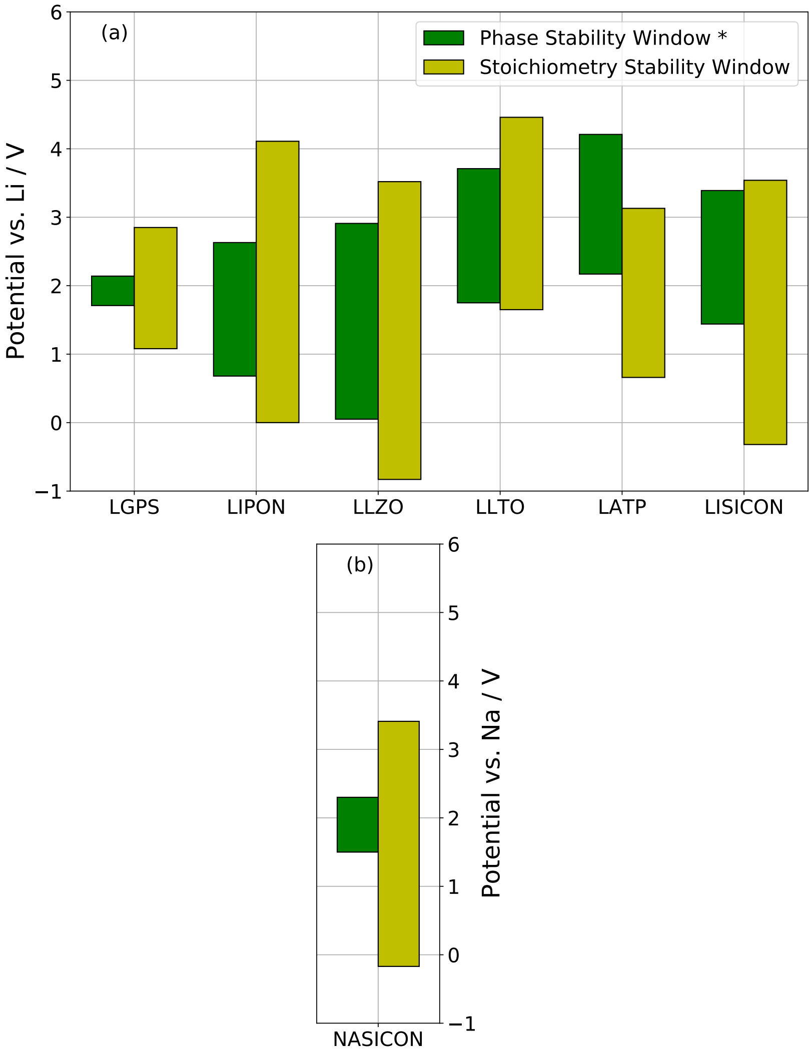

Figure 6.3 – Stoichiometry stability windows and phase stability windows for various Li-SSE materials (a) and NASICON (b). *For Li-SSE materials (a), published phase stability windows from Ref [141] are plotted. For NASICON (b) the phase stability window was computed with our own implementation.

Material	$\Phi^{\text{stoi}}_{\text{red}}$ / $V_{\text{vs. A}}$	$\Phi^{\text{stoi}}_{\text{ox}}$ / $V_{\text{vs. A}}$	$\Delta\Phi^{\text{stoi}}$ / V	$\Delta E^{\text{N}}_{\text{HL}}$ / eV
LGPS	1.08	2.85	1.77	2.21
LIPON	0.00	4.11	4.11	5.13
LLZO	−0.83	3.52	4.35	4.34
LLTO	1.65	4.46	2.81	2.56
LATP	0.66	3.13	2.47	2.48
LISICON	−0.32	3.54	3.86	3.63
NASICON	−0.17	3.41	3.58	4.34

Table 6.2 – Results from DFT computations with PBE functional and SSSP Efficiency pseudopotentials: Lower and upper limits $\Phi^{\text{stoi}}_{\text{red / ox}}$ and corresponding width $\Delta\Phi^{\text{stoi}}$ of the stoichiometry stability windows for the investigated SSE materials. Potential limits are given vs. the reference potential of A-metal oxidation (A=Li for Li-SSE materials, A=Na for NASICON). Also given are the electronic HOMO–LUMO gaps $\Delta E^{\text{N}}_{\text{HL}}$ of the systems with stable A-stoichiometry N.

previously published values [150] of 0.78 and 2.97 $V_{\text{vs. Li}}$, respectively. Figure 6.3a presents a comparison for the Li-SSE materials with the corresponding phase stability windows published in Ref. [141], which were also computed from DFT energies with PBE xc-functional. The phase stability window of NASICON shown in Figure 6.3b was computed using our own implementation of the method. We obtained a phase decomposition reduction potential of $\Phi^{\text{phase}}_{\text{red, NASICON}} = (1.50 \pm 0.23)\,V_{\text{vs. Na}}$ (with decomposition products ZrO_2, $Na_4P_2O_7$, P, and $Na_2ZrSi_2O_7$), and an oxidation potential of $\Phi^{\text{phase}}_{\text{ox, NASICON}} = (2.30 \pm 0.47)\,V_{\text{vs. Na}}$ (with products ZrO_2, $Na_4P_2O_7$, $Na_2ZrSi_6O_{15}$, and O_2), where we included an entropic contribution $-TS = -0.638$ eV to the free energy of gaseous O_2 at 300 K and 1 bar computed from NIST reference data [184].

In most cases, we find that the phase stability window is more limiting than the stoichiometry stability window, thus supporting the common assumption [151]. However, we find an exception for the upper stability limit of LATP, where our value for the stoichiometry oxidation potential is less than the reported phase decomposition oxidation potential [141]. Also, in many cases the difference between stoichiometry stability limit and phase stability limit is rather small, especially when taking into account realistic error margins of few hundred meV. This is the case for the lower potential limits of LGPS, LIPON, LLZO, and LLTO and for the upper potential limits of LGPS, LLZO, LLTO, and LISICON. We thus find a correlation between stoichiometry stability window and phase stability window.

LGPS was experimentally found stable at least from 0.0 to 5.0 $V_{\text{vs. Li}}$ [185], which is significantly wider than both its phase stability window and its stoichiometry stability window. This wide experimental stability window of native LGPS was confirmed in another study [186]. After mixing LGPS with carbon, the same authors observed redox processes around 0.0–0.5 $V_{\text{vs. Li}}$ and around 1.6–2.7 $V_{\text{vs. Li}}$, respectively. However, we are careful with attributing these potentials either to phase or to stoichiometry stability limits of LGPS, because it appears unclear to us whether the observed redox processes result from LGPS decomposition alone, from carbon, or from an interaction between both.

Experimental studies of LIPON found an electrochemical stability window from 0.0 to about 5.0–5.5 $\mathrm{V}_{\mathrm{vs.\,Li}}$ [187, 188], which agrees quite well with our computed stoichiometry stability window. Other authors, however, report decomposition of amorphous LIPON in contact with metallic Li observed by X-ray photoemission spectroscopy (XPS) [189], which is compatible with the positive lower limit of the phase stability window [141].

Stability of LLZO versus metallic Li was experimentally demonstrated [190, 191] in agreement with the computed lower limits $\lessapprox 0.0\,\mathrm{V}_{\mathrm{vs.\,Li}}$ of both phase and stoichiometry stability windows. In one study, LLZO was observed to be stable against oxidation up to very high potentials [192]. Other authors report an onset of LLZO oxidation at around 4.0 $\mathrm{V}_{\mathrm{vs.\,Li}}$ [193], which is very close to the upper limit of our computed stoichiometry stability window, especially from hybrid functional DFT results, cf. Table 6.3. However, also in this study carbon was mixed with the LLZO so that other oxidation reactions could also be responsible for the experimental result.

LLTO is a very interesting case, because the lower limits of both the phase stability window [141] and the stoichiometry stability window are almost identical at $\approx 1.7\,\mathrm{V}_{\mathrm{vs.\,Li}}$. This perfectly agrees with experimental observations: A careful experimental study demonstrated LLTO reduction below 1.7 $\mathrm{V}_{\mathrm{vs.\,Li}}$ [194]. Because the amount of transferred Li agreed well with the number of available Li vacancies inside the LLTO lattice, insertion of Li into the LLTO host lattice was concluded. At lower potentials, more Li was consumed, which was attributed to the formation of secondary decomposition phases. Thus, this study demonstrated that the stoichiometry stability window defined the lower stability limit of LLTO. A similar LLTO reduction potential was experimentally determined also by other authors [195].

Another interesting case is LATP, where our computed upper limit of the stoichiometry stability window $\Phi_{\mathrm{ox}}^{\mathrm{stoi}}$ is significantly less than the previously reported phase stability limit $\Phi_{\mathrm{ox}}^{\mathrm{phase}}$ [141]. This result even holds for our hybrid functional DFT results, cf. Table 6.3. Unfortunately, to the best of our knowledge, no experimental study on electrochemical LATP oxidation exists to date that could confirm whether the stoichiometry stability window is indeed defining the upper LATP stability limit.

For LISICON, we find almost identical upper limits of our computed stoichiometry stability window and the previously published phase stability window [141]. However, a negative value of the lower limit of the stoichiometry stability window indicates stability against metallic Li, whereas the phase stability window predicts instability. Experimentally, a strong reaction between LISICON and Li metal was observed [196, 197], clearly demonstrating that the lower phase stability limit is critical.

Turning to the results for NASICON, the negative value of $\Phi_{\mathrm{red}}^{\mathrm{stoi}}$ indicates stoichiometric stability of NASICON against a Na metal electrode, whereas our computed phase decomposition reduction potential $\Phi_{\mathrm{red,\,NASICON}}^{\mathrm{phase}} = (1.50\pm0.23)\,\mathrm{V}_{\mathrm{vs.\,Na}}$ predicts NASICON to be unstable against Na metal in agreement with experimental findings [198]. However, other authors reported that no reaction was observed between NASICON and metallic Na [199]. Recently, an experimental study reported a very wide electrochemical stability window for Ca-doped NASICON [200].

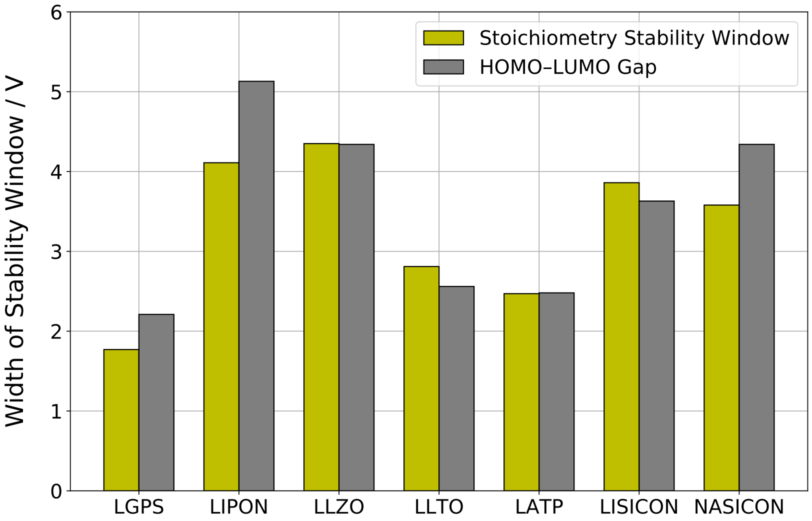

Figure 6.4 – Width $\Delta\Phi^{\mathrm{stoi}}$ of the stoichiometry stability windows in comparison with the HOMO–LUMO gap $\Delta E_{\mathrm{HL}}^{\mathrm{N}}$ for the investigated SSE materials.

The wider experimental stability windows compared to computed phase stability windows observed for many SSE materials were convincingly explained with passivation due to interphase layers of decomposition products between electrode and SSE [141]. A complementary possible explanation is a kinetic sluggishness of phase decomposition reactions [141]. It was proposed that the A-insertion/extraction potentials, i.e. the stoichiometry stability window, provide hard limits for the SSE stability, because the transfer of single A-atoms between electrode and SSE is likely to be fast [151]. Furthermore, the insertion or extraction of single A-atoms into/from the SSE structure might represent the first step in the mechanism of SSE phase decomposition reactions. Therefore, even when strict thermodynamic stability is defined by the phase stability window, the stoichiometry stability window could represent a "kinetic" stability window up to which SSE phase decomposition reactions are kinetically hindered. This interpretation could explain why in many cases better agreement is found between experimental stability windows and the stoichiometry stability window rather than the phase stability window.

Comparison of stoichiometry stability window and HOMO–LUMO gap. The electronic HOMO–LUMO gaps $\Delta E_{\mathrm{HL}}^{\mathrm{N}}$ of the systems with stable A-stoichiometry N are compiled in Table 6.2. Figure 6.4 presents a comparison of the widths $\Delta\Phi^{\mathrm{stoi}}$ of the stoichiometry stability window with the HOMO–LUMO gaps $\Delta E_{\mathrm{HL}}^{\mathrm{N}}$ for the investigated SSE materials. As expected from equation (6.16) and the discussion thereafter, a very good agreement is observed for LGPS, LLZO, LLTO, LATP, and LISICON. Only for LIPON and NASICON, $\Delta E_{\mathrm{HL}}^{\mathrm{N}}$ is significantly larger than $\Delta\Phi^{\mathrm{stoi}}$. The latter discrepancies can result from electronic states of the conduction band that are shifted down into the band gap upon insertion of the additional A^+ ion in the N+1 stoichiometry system.

The HOMO–LUMO method [146, 147, 148] considers only electron transfer between electrode and SSE. Consequently, the electrochemical stability window is assessed from the ionization potential and electron affinity of the SSE. Transfer of A^+ ions is neglected and the electrode is considered to be chemically inert. Therefore, the HOMO–LUMO gap is generally considered to provide only an upper bound for the true stability potential window of an SSE material [148, 142]. However, according to relation (6.16) and supported by our computational results, the HOMO–LUMO gap is essentially identical to the width of the stoichiometry stability window. Therefore, both methods implicitly consider the same physical process, i.e. an infinitesimal exchange of A between electrode and SSE. Consequently, as discussed above, exceptional cases can exist where the limiting stability window of an SSE material is defined by its stoichiometry stability potentials, i.e. its HOMO–LUMO gap. The advantage of the stoichiometry stability method over the HOMO–LUMO method is that the former directly yields the absolute position of the stability window vs. a reference potential.

Influence of hybrid functional DFT. We calculated the phase stability window of LLZO at the hybrid functional DFT level. Using the HSE06 functional, we recomputed only the reaction energies of the limiting reduction and oxidation decomposition reactions that were obtained from our implementation of the phase stability method with PBE functional. The respective decomposition products are Li_2O, La, $Li_6Zr_2O_7$ for the limiting reduction reaction, and Li_2O_2, La_2O_3, $Li_6Zr_2O_7$ for the limiting oxidation reaction. We obtained $\Phi^{\text{phase, HSE06}}_{\text{red, LLZO}} = 0.00\,\text{V}_{\text{vs. Li}}$ and $\Phi^{\text{phase, HSE06}}_{\text{ox, LLZO}} = 2.84\,\text{V}_{\text{vs. Li}}$. Also, we recomputed the stoichiometry stability windows of LLZO, LLTO, and LATP using the HSE06 hybrid functional for the minimum energy configurations obtained from the stoichiometry stability workflow with PBE functional. Results are summarized in Table 6.3 and presented in Figure 6.5a. Note that we had to use different pseudopotentials (SG15 ONCV) for hybrid DFT computations than the SSSP Efficiency pseudopotentials used in the phase stability and stoichiometry stability workflows. For direct comparability, we also recomputed the critical PBE DFT energies with the SG15 ONCV pseudopotentials for the PBE results shown in Figure 6.5a, which, therefore, slightly differ from the results presented in Figure 6.3.

We find that the hybrid functional has only minor influence on the reduction potential limits of the investigated phase stability window and stoichiometry stability windows. In these cases, a reliable prediction of SSE stability against a metallic Li electrode is obtained at PBE level. However, PBE results significantly underestimate the oxidation potential limits of the stoichiometry stability windows compared to HSE06. Also the oxidation potential limit of the LLZO phase stability window is increased using HSE06. Thus, the computation of reliable oxidation potentials appears more demanding than for reduction potentials. This difference might originate from the difference between anionic vs. cationic redox behaviour, because SSE reduction largely corresponds to cationic reduction processes, whereas SSE oxidation can affect both cation and anion valencies.

Figure 6.5b presents a comparison of the widths of stoichiometry stability windows and

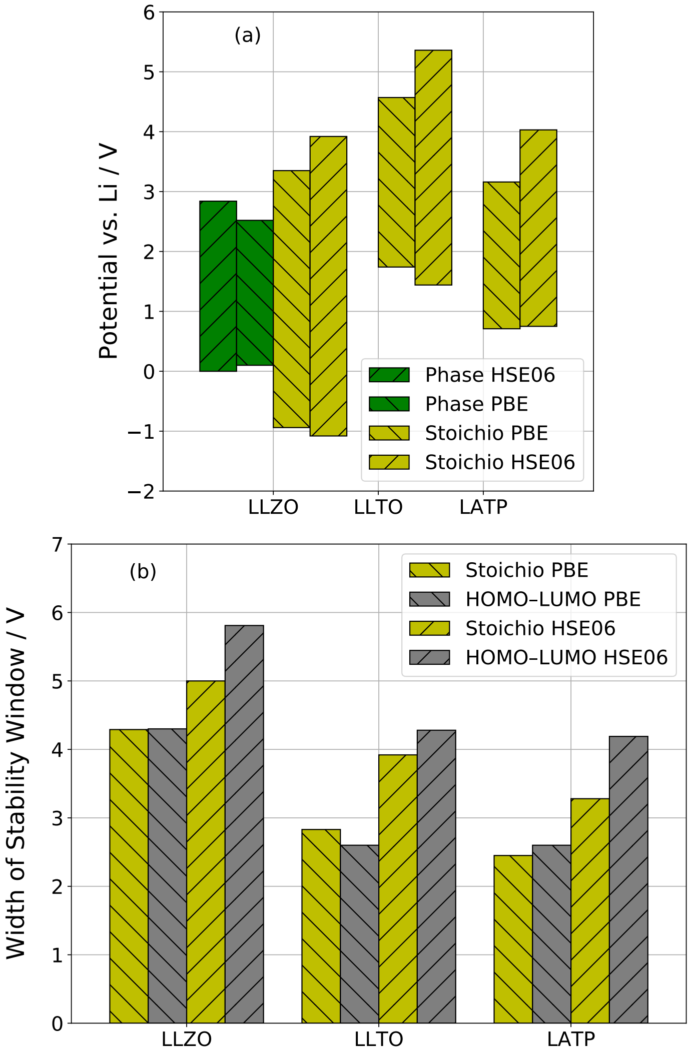

Figure 6.5 – Comparison of stability windows computed with PBE and with HSE06 DFT functionals. (a) Phase stability windows and stoichiometry stability windows. (b) Width $\Delta\Phi^{\mathrm{stoi}}$ of the stoichiometry stability windows and HOMO–LUMO gaps $\Delta E^{\mathrm{N}}_{\mathrm{HL}}$.

Material	$\Phi^{\mathrm{stoi}}_{\mathrm{red}}$ / $\mathrm{V_{vs.\,Li}}$	$\Phi^{\mathrm{stoi}}_{\mathrm{ox}}$ / $\mathrm{V_{vs.\,Li}}$	$\Delta\Phi^{\mathrm{stoi}}$ / V	$\Delta E^{\mathrm{N}}_{\mathrm{HL}}$ / eV
LLZO	−1.08	3.92	5.00	5.81
LLTO	1.44	5.36	3.92	4.28
LATP	0.75	4.03	3.28	4.19

Table 6.3 – Results from hybrid functional DFT computations with HSE06 functional and SG15 ONCV pseudopotentials: Lower and upper limits $\Phi^{\mathrm{stoi}}_{\mathrm{red\,/\,ox}}$ and corresponding width $\Delta\Phi^{\mathrm{stoi}}$ of the stoichiometry stability windows, and the electronic HOMO–LUMO gaps $\Delta E^{\mathrm{N}}_{\mathrm{HL}}$ of the systems with stable A-stoichiometry N.

HOMO–LUMO gaps obtained with PBE and HSE06 functionals for LLZO, LLTO, and LATP. In all cases, both the width of the stoichiometry stability window and the HOMO–LUMO gap increase going from PBE to HSE06, which is expected because GGA functionals are known to underestimate band gaps whereas hybrid functionals yield better estimates [201]. Surprisingly, however, the agreement between the widths of stoichiometry stability windows and the HOMO–LUMO gaps is significantly reduced at HSE06 level.

6.6 Conclusion

We analysed the relation between three different methods to compute the electrochemical stability window of solid-state electrolytes, namely the HOMO–LUMO method, the phase stability method, and the stoichiometry stability method. We found that the latter represents a link between the former two methods. Whereas the phase stability method takes into account the equilibrium potentials of SSE phase decomposition reactions, the stoichiometry stability method considers the insertion and extraction of single A-atoms (A = Li, Na) into/from the intact SSE structure. Because these sets of instability reactions are disjoint, the corresponding phase and stoichiometry stability windows are complementary. We further provided computational implementations of the methods and we compared the results for the relevant Li- and Na-SSE materials LGPS, LIPON, LLZO, LLTO, LATP, LISICON, and NASICON. In most cases, the phase stability window is stricter than the stoichiometry stability window. However, we also found exceptions to that rule. Comparison with reported experimental stability windows revealed an ambiguous picture: Whereas for some SSE materials the experimental observations agree with computational phase stability windows, for other SSE materials experimental stability windows are wider and in better agreement with the computational stoichiometry stability windows.

Acknowledgement

This research was supported by the NCCR MARVEL, funded by the Swiss National Science Foundation. This work was supported by a grant from the Swiss National Supercomputing Centre (CSCS) under project IDs mr0, mr18 and mr28. We thank Leonid Kahle from EPFL, Lausanne, for help with the computational implementation.

Supplementary information

Derivation of Nernst equation; Simple model for stoichiometry stability window; Extended model for stoichiometry stability window.

7 Conclusion

Summary

This thesis focused on the description of solid-state electrolytes using polarizable force-fields and the facilitation of their use through a novel procedure for the training of such force-fields.

The value of polarizable force-fields for the study of solid-state electrolytes was demonstrated using LLZO as a case study showing that valuable insights that can be obtained both for static and dynamic properties. In particular, the effects of the adition of tungsten as a dopant on the structural and dynamic properties of LLZO were investigated. To reach a better understanding of the origin of the changes resulting of the introduction of dopants, two models were compared. An implicit doping model, where the additional positive charges is introduced as a background effect and an explicit one where the tungsten centers are explicitly considered. The importance of an ensemble averaging of the properties over distributions of the possible tungsten arrangement was demonstrated. Two competing effects of the doping on the ionic conductivity of LLZO were identified. The first one is thermodynamic and relates to the stabilization of the conducting phase by the depletion of the lithium. The second one affects the dynamics of the lithium ions around the doping centers by creating barriers that limits the diffusion of the ions. Overall, the results reveal a complex interplay of effects and behaviors acting on the ionic conductivity of LLZO as a function of its doping.

The training of polarizable force-fields is a more complex problem than the one of their non-polarizable counterparts. The increased complexity mostly resides in the need to adjust the position of the shells used to model the polarizability as the training progresses. This constant update of the shell position is probably the highest barrier in the use of global optimization schemes for polarizable force-fields. In this thesis, a method using an optimal placement of the shells to minimize the error on their associated cores is used to avoid the need for a relaxation of the shells for each new set of parameters. These methods allows the use of global algorithms such as Differential Evolution and Self-Adaptive Differential Evolution to be used. A set of force-fields was generated for lithium tantalate from first-principles trajectories. The resulting parameter sets are able to reproduce well the reference first-principle forces. Further attempts to optimize these sets through gradient based method showed little to no improvements. The use of analytical gradients was also demonstrated resulting in smoother gradients to no avail. The most problematic component of the force-field remained the O – O Buckingham potential due to its small value and gradient. The methodology was implemented in the AiiDA framework through several workchains allowing the full automation of the training process starting from individual *cif* files.

Global optimization provides a mean to generate force-fields without the input of approximate solutions. The generation of training sets however still relies either on expensive first-principles trajectories or the use of approximated sets of parameters. To remove this initial dependency on expensive methods or parameters, a methodology was developed to generate training structures from a generic crystal structures. The methodology leverages Monte-Carlo sampling to resolve partially occupied structures. An approximate force-field based solely on Coulombic interactions is used throughout this procedure. The method allows the generation of Boltzmann distributed set of structures to be used in the training. Random displacements are used to mimic thermal displacements in the generated training sets. The method is successful at reproducing well enough the radial pair distributions observed in molecular dynamics trajectories. Force-fields are generated for lithium tantalate using the procedure. The force-fields obtained using the methodology are able to effectively reproduce the structural parameter of rhombohedral lithium tantalates and its dynamic properties with conductivity values and activation energies similar to those found in previous studies using force-fields and first-principles. The difficulty to fully optimize the parameters is most likely still related to the difficulty to optimize the potential of the O – O pair.

Although conductivity is one of the key properties that needs to progress for solid-states electrolytes to be able to fully replace current technologies, the electrochemical stability of these materials remains another key barrier to their development. Three methodologies available for the computation of the electrochemical stability windows of materials are presented and reviewed: the HOMO-LUMO method, the stoichiometry stability method and the phase stability method. All three methods were implemented within the AiiDA framework as workflows. Comparison of the predicted stability windows are presented for several relevant Li- and Na-based solid-state electrolytes. Further comparison with available experimental values was done when such data was available. This showed an ambiguous picture with experimental observations agreeing for some materials with the narrower phase stability method and for others with the wider stoichiometry stability one.

Future work

The work described in this thesis demonstrate the value of using polarizable force-fields to describe thermodynamic and kinetic properties of solid-state electrolytes. Although the computed properties do not reach a quantitative accuracy, their contribution to a better understanding of the systems is invaluable.

However insightful the information presented concerning about the effects of doping on LLZO is, investigation of more dopants and systems is necessary to build a more comprehensive picture of the field. A better understanding of these various effects is critical for a more efficient knowledge driven design of new solid-state electrolytes through doping. This will allow to better focus the effort of experimental teams. To this goal the work achieved here stands as a stepping stones as it provides a mean of preparing the force-fields necessary for those studies in an unsupervised fashion allowing for the evaluation of libraries of structures and dopants. Improvements to the procedures have already been mentioned in the Chap. 5 and would most likely prove to be valuable upgrades to the described methodology.

A Supporting Information

A.1 Comparison of computational methods for the electrochemical stability window of solid-state electrolyte materials

Derivation of Nernst equation

We derive the Nernst equation for the cell reaction

$$\mathrm{SSE} + x\mathrm{A} \longleftrightarrow \mathrm{D1} + \mathrm{D2} + \cdots \tag{A.1}$$

The corresponding half-cell reactions are the SSE reaction at the working electrode (WE) interface

$$\mathrm{SSE} + x\mathrm{A}^{+} + x\mathrm{e}^{-} \longleftrightarrow \mathrm{D1} + \mathrm{D2} + \cdots \tag{A.2}$$

and the A-metal counter electrode (CE) reaction

$$x\mathrm{A} \longleftrightarrow x\mathrm{A}^{+} + x\mathrm{e}^{-} \tag{A.3}$$

For electrochemical equilibrium of reactions (A.2) and (A.3), the conditions must be fulfilled that the stoichiometric sums of the chemical potentials of reactants and of products are equal,

$$\mu_{\mathrm{SSE}} + x\mu_{\mathrm{A}^+} + x\mu_{\mathrm{e}^-}^{\mathrm{WE}} = \mu_{\mathrm{D1}} + \mu_{\mathrm{D2}} + \cdots \tag{A.4}$$

$$x\mu_{\mathrm{A}} = x\mu_{\mathrm{A}^+} + x\mu_{\mathrm{e}^-}^{\mathrm{CE}} \tag{A.5}$$

In equilibrium, the chemical potential μ_{A^+} of A^+ is constant throughout the electrolyte and therefore identical at CE and WE. The equilibrium potential of reaction (6.2) vs. the reference potential defined by reaction (6.3) is given by the difference of the electron chemical potentials of WE and CE divided by the electron charge,

$$\begin{aligned}\Phi_{\text{eq}} &= \frac{1}{-e}\,(\mu^{\text{WE}}_{\text{e}^-} - \mu^{\text{CE}}_{\text{e}^-}) \\ &= \frac{1}{-e\,x}\,(\mu_{\text{D1}} + \mu_{\text{D2}} + \cdots - \mu_{\text{SSE}} - x\,\mu_{\text{A}}) \\ &= -\frac{\Delta G}{e\,x}\end{aligned} \tag{A.6}$$

In the first step, we resolved and inserted equations (A.4) and (A.5) for the electron chemical potentials of WE and CE, respectively. In the second step, we used the fact that the chemical potential of a compound is equal to its Gibbs free energy per unit.

Equation (A.6) is not the Nernst equation in its typical form, which expresses the equilibrium potential as a function of the activities a_i of reactants and products. The typical form of the Nernst equation is simply obtained from equation (A.6) by inserting the definitions of the reactant and product activities $\mu_i = \mu_i^0 + k_B T \log(a_i/a^0)$, with Boltzmann constant k_B, temperature T, standard activity a^0, and standard chemical potential μ_i^0.

Stoichiometry stability window: Simplest model

We develop a simple model for the dependence of the SSE stoichiometry A_{n+z}M (where A = Li, Na, ...) as a function of the electrode potential Φ that the SSE is in contact with. Very similar models were derived for the Li-insertion into electro-active materials [158]. We first derive a simplified expression of the Gibbs free energy $G(z) := G_{\text{A}_{n+z}\text{M}}$ for $|z| \ll n$, i.e. for small deviations from the stable composition. For this purpose, the Gibbs free energy (per unit cell) $G = U + pV - TS$ is first approximated by $G = E_0 - TS_{\text{conf}}$, in which only the energy E_0 at $T = 0\,\text{K}$ and the configurational entropy S_{conf} of A-site occupation are taken into account. The configurational entropy carries the dominant part of the dependence of the Gibbs free energy on the A-stoichiometry. It therefore cannot be neglected for deriving z as a function of Φ. Other contributions like the pV term, the vibrational zero-point energy, the vibrational internal energy, and the vibrational entropy are neglected, which is well justified if an error of $\pm 0.1\,\text{V}$ is acceptable on the calculated stability potential window.

For $|z| \ll n$, the energy of adding one A to the general composition A_{n+z}M is approximately constant, i.e. $E_0 \approx E_0^0 + \Delta E_0^{+/-}\,z$, for $z \gtrless 0$, respectively. Here, as explained in detail in the main article, it is taken into account that the energy $\Delta E_0^{+/-}$ of adding A is discontinuous at $z = 0$, resulting in two different constant values $\Delta E_0^+ > \Delta E_0^-$ for $z \gtrless 0$, respectively.

Within this simplified 1-type A-site model, it is assumed that all A-sites are energetically equivalent. In the next section, a more general 2-type A-site model is derived. Assuming a total number $n + m$ of A-sites, either occupied or unoccupied, per unit cell of the material A_{n+z}M, the configurational entropy S_{conf} results from the combinatorics of filling $n + z$ out of a total of $n+m$ sites:

$$S_{\text{conf}} = \frac{1}{N_c}\, k_B \log\begin{pmatrix} N_c\,(n+m) \\ N_c\,(n+z) \end{pmatrix} \tag{A.7}$$

$$\approx k_B\,((n+m)\log(n+m) - (n+z)\log(n+z) - (m-z)\log(m-z)) \tag{A.8}$$

where k_B is the Boltzmann constant and where Stirling's approximation was applied, because the total number N_c of unit cells in the entire crystal is very large.

According to the equations derived in the main article, we obtain for the A-chemical potential in the SSE

$$\mu^{\text{A}}_{\text{SSE}}(z) = \frac{\mathrm{d}G}{\mathrm{d}z} = \Delta E_0^{+/-} - k_B T \log\left(\frac{n+m}{n+z} - 1\right) \tag{A.9}$$

where the $+/-$ refer to $z > 0$ and $z < 0$, respectively, and for the corresponding equilibrium potential

$$\Phi_{\text{eq}} = -\frac{1}{e}\left(\mu^{\text{A}}_{\text{SSE}}(z) - \mu^{\text{A}}_{\text{A}}\right) \tag{A.10}$$

$$= \Phi_{\text{I/II}} + \frac{k_B T}{e} \log\left(\frac{n+m}{n+z} - 1\right) \tag{A.11}$$

where

$$\Phi_{\text{I/II}} := -(\Delta E_0^{+/-} - \mu^{\text{A}}_{\text{A}})/e \tag{A.12}$$

again for $z > 0$ and $z < 0$, respectively, and with $\Phi_{\text{I}} < \Phi_{\text{II}}$ because $\Delta E_0^{+} > \Delta E_0^{-}$.

Vice versa, for a given electrode potential Φ, the equilibrium stoichiometry deviation z of the SSE in contact with the respective electrode is obtained by resolving Equation (A.11) with $\Phi_{\text{eq}} = \Phi$:

$$z = \begin{cases} \frac{(n+m)}{1+\exp\left((\Phi-\Phi_{\text{I}})/\gamma\right)} - n & ,\Phi < \Phi_{\text{I}} + \delta \\ 0 & ,\Phi_{\text{I}} + \delta \le \Phi \le \Phi_{\text{II}} + \delta \\ \frac{(n+m)}{1+\exp\left((\Phi-\Phi_{\text{II}})/\gamma\right)} - n & ,\Phi_{\text{II}} + \delta < \Phi \end{cases} \tag{A.13}$$

where $\gamma = \frac{k_B T}{e}$ and $\delta = \gamma \log(m/n)$. Thus, the limits of the stoichiometry stability window are given by $\Phi^{\text{stoi}}_{\text{red}} = \Phi_{\text{I}} + \delta$ and $\Phi^{\text{stoi}}_{\text{ox}} = \Phi_{\text{II}} + \delta$. For an acceptable error of $\pm 0.1\,\text{V}$ on the stability limits, the shift δ can be neglected: For a practical SSE material, the number of occupied and unoccupied A-sites will be of the same order of magnitude. Even for $m/n = 10^{\pm 1}$, it follows $|\delta| \approx 2\gamma$ with $\gamma = 0.025\,\text{V}$ for $T \approx 300\,\text{K}$.

Figure A.1 plots the deviation z as a function of the electrode potential Φ as described by

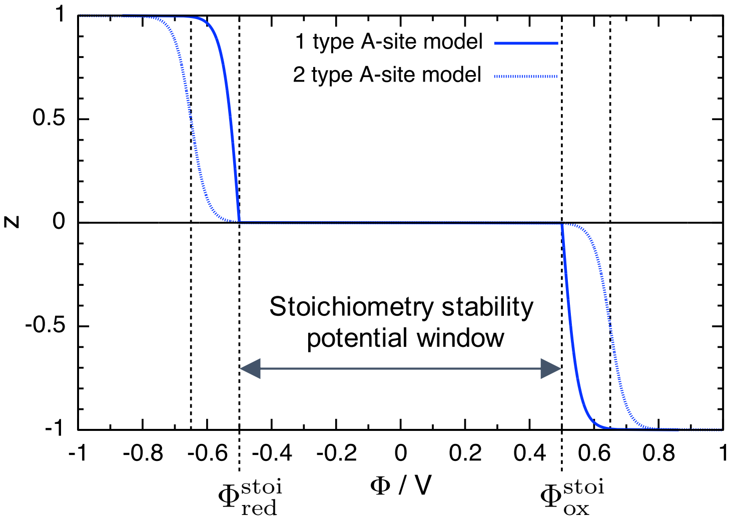

Figure A.1 – The stoichiometry deviation z in the general SSE material $A_{n+z}M$ as a function of the potential Φ as derived from the two models in the limit $|z| \ll n$: The '1 type A-site model' considers all A-sites energetically equivalent, whereas the '2 type A-site model' takes into account two energetically different types of A-sites. The values of the model parameters used for the plotted curves are given in the text.

Equation (A.13) for an arbitrary choice of $n = 1$, $m = 1$, $\Phi_{\mathrm{red}}^{\mathrm{stoi}} = -0.5\,\mathrm{V}$, $\Phi_{\mathrm{ox}}^{\mathrm{stoi}} = +0.5\,\mathrm{V}$, and for $\gamma = 0.025\,\mathrm{V}$ corresponding to $T \approx 300\,\mathrm{K}$. The stoichiometry dramatically changes in two steep steps below and above $\Phi_{\mathrm{red}}^{\mathrm{stoi}}$ and $\Phi_{\mathrm{ox}}^{\mathrm{stoi}}$, respectively, the width of each step being defined by the scale γ. The step below $\Phi_{\mathrm{red}}^{\mathrm{stoi}}$ corresponds to SSE reduction, whereas the step above $\Phi_{\mathrm{ox}}^{\mathrm{stoi}}$ corresponds to SSE oxidation. Within the stoichiometry stability window, i.e. for potentials $\Phi_{\mathrm{red}}^{\mathrm{stoi}} \leq \Phi \leq \Phi_{\mathrm{ox}}^{\mathrm{stoi}}$, the stoichiometry deviation is equal to zero, $z = 0$, and the SSE is stable in the composition A_nM.

Within the present model we assume that all $n + m$ A-sites within the SSE material A_nM are energetically equivalent, i.e. every distribution of the n A over the $n + m$ sites has the same energy. However, in general, there will be energetic variations between different distributions. In the following section, we present an extended model which takes into account two different classes of A-sites in the material A_nM: one class of n occupied ground-state sites, and another class of m vacant excited-state sites.

Stoichiometry stability window: Model with two classes of A-sites

We consider a general solid-state electrolyte (SSE) material with n occupied and m unoccupied A-sites per unit cell, the latter unoccupied sites referred to as vacancies V, in its stable stoichiometry. Further, it is assumed that the occupied and unoccupied A-sites are separated by a non-zero energy gap, which is plausible if the vacancies correspond to interstitial sites or if they are generated by a dopant. In order to distinguish these two classes of A-sites, the

m unoccupied 'excited' state sites are denoted on the left-hand side, whereas the n occupied 'ground' state sites are denoted on the right-hand side of the composition formula $\mathrm{V}_m\mathrm{MA}_n$.

If more A is added to the stable configuration $\mathrm{V}_m\mathrm{MA}_n$, it has to occupy vacant sites of the class of 'excited' state sites. Consequently, the additional A is added on the left-hand side to yield $\mathrm{A}_\delta\mathrm{V}_{\mathrm{m}-\delta}\mathrm{MA}_n$. Vice versa, if A is extracted from the stable configuration $\mathrm{V}_m\mathrm{MA}_n$, vacancies are generated among the previously occupied 'ground' state sites denoted on the right-hand side to yield $\mathrm{V}_m\mathrm{MA}_{\mathrm{n}-\epsilon}\mathrm{V}_\epsilon$. Of course, also combinations of both processes are possible, such that the general state of the SSE material can be described by the formula $\mathrm{A}_x\mathrm{V}_{m-x}\mathrm{MA}_{n+y}\mathrm{V}_{-y}$, where $0 \leq x \leq m$ and $-n \leq y \leq 0$. Furthermore, as discussed for the simpler model in the main article, the total stoichiometry $n+x+y$ of A must be compared against the stable stoichiometry n, since the latter separates two distinct energetic manifolds for compositions with A-excess, i.e. $x+y>0$, and A-deficiency, i.e. $x+y<0$, respectively.

According to the equations derived in the main article, the equilibrium potential of the A-exchange reactions with a general electrode material is given by

$$\Phi_{\mathrm{eq}} = -\frac{1}{e}\left(\mu^{\mathrm{A}}_{\mathrm{SSE}}(z) - \mu^{\mathrm{A}}_{\mathrm{A}}\right) \tag{A.14}$$

where $\mu^{\mathrm{A}}_{\mathrm{A}}$ is the chemical potential of A-metal defining the reference potential $\Phi_{\mathrm{ref}} = -\mu^{\mathrm{A}}_{\mathrm{A}}/e$. The chemical potential $\mu^{\mathrm{A}}_{\mathrm{SSE}}$ of species A for the general SSE composition $\mathrm{A}_x\mathrm{V}_{m-x}\mathrm{MA}_{n+y}\mathrm{V}_{-y}$ is given by the derivative of the Gibbs free energy $G(x,y) := G_{\mathrm{A}_x\mathrm{V}_{m-x}\mathrm{MA}_{n+y}\mathrm{V}_{-y}}$ w.r.t. the *total* A-stoichiometry deviation $z = x+y$,

$$\mu^{\mathrm{A}}_{\mathrm{SSE}}(z) = \frac{\mathrm{d}G}{\mathrm{d}z} \tag{A.15}$$

$$= p_x(z)\left.\frac{\partial G}{\partial x}\right|_{(x(z),y(z))} + p_y(z)\left.\frac{\partial G}{\partial y}\right|_{(x(z),y(z))} \tag{A.16}$$

where $p_x = \mathrm{d}x/\mathrm{d}z$ and $p_y = \mathrm{d}y/\mathrm{d}z = 1 - p_x$ are the thermodynamic weights of the excited state sites and ground state sites, respectively. For given $z = x+y$, the values of $x(z)$, $y(z)$, $p_x(z)$, and $p_y(z)$ are fixed by the thermodynamic equilibrium requirement of minimum $G(x,y)$, as calculated below.

In the following, an expression for the Gibbs free energy $G(x,y)$ is derived for $|x|,|y| \ll n$, i.e. for small deviations from the stable composition. As for the simpler model presented in the previous section, the total Gibbs free energy $G = U + pV - TS$ is first approximated by $G = E_0 - TS_{\mathrm{conf}}$, i.e. only the energy E_0 at $T = 0\,\mathrm{K}$ and the configuration entropy S_{conf} of the combinatorics of A-site occupation are taken into account. For $|x|,|y| \ll n$, the energies ΔE^e_0 and ΔE^g_0 of adding one A either to the excited state or to the ground state class of A-sites in $\mathrm{A}_x\mathrm{V}_{m-x}\mathrm{MA}_{n+y}\mathrm{V}_{-y}$, respectively, are approximately constant. Furthermore, in the same way as for the simpler model, the energy discontinuity between $x+y<0$ and $x+y>0$ must be taken into account by a term $\Delta E^{+/-}_0\,(x+y)$, resulting in an expression for the total energy in the limit

$|x|, |y| \ll n$,

$$E_0 \approx E_0^0 + \Delta E_0^e\, x + \Delta E_0^g\, y + \Delta E_0^{+/-}\,(x+y) \tag{A.17}$$

for $x + y \gtrless 0$, respectively.

The configuration entropy has two contributions, $S_{\text{conf}} = S_e + S_g$, resulting from the combinatorics of filling excited state or ground state A-sites, respectively:

$$S_e = \frac{1}{N_c}\, k_B \log \binom{N_c\, m}{N_c\, x} \tag{A.18}$$

$$\approx k_B\,(m \log(m) - x \log(x) - (m-x)\log(m-x)) \tag{A.19}$$

where Stirling's approximation has been applied, $0 \leq x \leq m$, and k_B is the Boltzmann constant. Likewise,

$$S_g \approx k_B\,(n \log(n) - (n+y)\log(n+y) - (-y)\log(-y)) \tag{A.20}$$

where $-n \leq y \leq 0$.

In order to find the thermodynamic weights $p_{x/y}$, first the thermodynamic equilibrium value of x for a fixed value of the total stoichiometry deviation $z = x + y$ must be derived that is defined by the minimum of the function $G(x, y = z - x)$, i.e. by the condition $\mathrm{d}G(x, y = z - x)/\mathrm{d}x = 0$, which is equivalent to the condition $\partial G/\partial x = \partial G/\partial y$ or

$$y = \frac{-n(m-x)}{x \exp(\Delta E/k_B T) + (m-x)} \tag{A.21}$$

where $\Delta E = \Delta E_0^e - \Delta E_0^g$ is the energy difference between excited and ground state sites. Inserting $y = z - x$ and resolving for x, we obtain

$$\begin{aligned} x \;=\; & \frac{z\,(e^{\Delta E/k_B T} - 1) - n - m}{2(e^{\Delta E/k_B T} - 1)} + \\ & + \frac{\sqrt{(z\,(e^{\Delta E/k_B T} - 1) - n - m)^2 + 4m(n+z)(e^{\Delta E/k_B T} - 1)}}{2(e^{\Delta E/k_B T} - 1)} \end{aligned} \tag{A.22}$$

where the positive solution of the quadratic equation has been used according to the requirement $0 \leq x$. Thus, the following expression is obtained for $p_x = \mathrm{d}x/\mathrm{d}z$,

$$p_x = \frac{1}{2} + \frac{1}{2}\, \frac{m - n + z\,(e^{\Delta E/k_B T} - 1)}{\sqrt{(z\,(e^{\Delta E/k_B T} - 1) - n - m)^2 + 4m(n+z)(e^{\Delta E/k_B T} - 1)}} \tag{A.23}$$

The chemical potential as a function of z follows from Equation (A.16),

$$\begin{aligned}\mu^{\mathrm{A}}_{\mathrm{SSE},+/-} = \quad & \Delta E_0^{+/-} + p_x\,\Delta E_0^e + p_y\,\Delta E_0^g - p_x\,k_B T\,\log\left(\frac{m}{x}-1\right)\\ & - p_y\,k_B T\,\log\left(\frac{n}{n+y}-1\right)\end{aligned} \tag{A.24}$$

for $z > 0$ and $z < 0$, respectively, where x as a function of z is given by Equation (A.22), $y = z - x$, p_x is given by Equation (A.23), and $p_y = 1 - p_x$. The corresponding equilibrium potential Φ_{eq} as a function of z is obtained from Equation (6.4),

$$\begin{aligned}\Phi_{\mathrm{eq}} = \quad & \Phi_{\mathrm{I/II}} + p_x\,\Delta\Phi_e + p_y\,\Delta\Phi_g + p_x\,\frac{k_B T}{e}\,\log\left(\frac{m}{x}-1\right)\\ & + p_y\,\frac{k_B T}{e}\,\log\left(\frac{n}{n+y}-1\right)\end{aligned} \tag{A.25}$$

where $\Phi_{\mathrm{I/II}} = -(\Delta E_0^{+/-} - \mu^{\mathrm{A}}_{\mathrm{A}})/e$ for $z > 0$ and $z < 0$, respectively, and $\Delta\Phi_{e/g} = -\Delta E_0^{e/g}/e$.

Unlike for the simpler model presented in the main article, expression (A.25) cannot be analytically resolved to obtain the equilibrium stoichiometry deviation z as a function of an applied potential Φ. Nevertheless, the latter can be plotted as shown in Figure A.1 for an arbitrary choice of $m = n = 1$, $\Phi_{\mathrm{I/II}} = \mp 0.5\,\mathrm{V}$, $\Delta\Phi_{e/g} = \mp 0.15\,\mathrm{V}$, and for $k_B T = 0.025\,\mathrm{eV}$. The main qualitative features of the simpler model are preserved, i.e. the stoichiometry changes in two steep steps starting at approximately $\Phi_{\mathrm{I/II}}$, the width of each step being defined by the scale $k_B T/e$. However, the energetic splitting between excited and ground state sites results in a smoother shape of the steps around $\Phi_{\mathrm{I/II}}$ and the turning points of the steps are shifted to approximately $\Phi_{\mathrm{I/II}} + \Delta\Phi_{e/g}$.

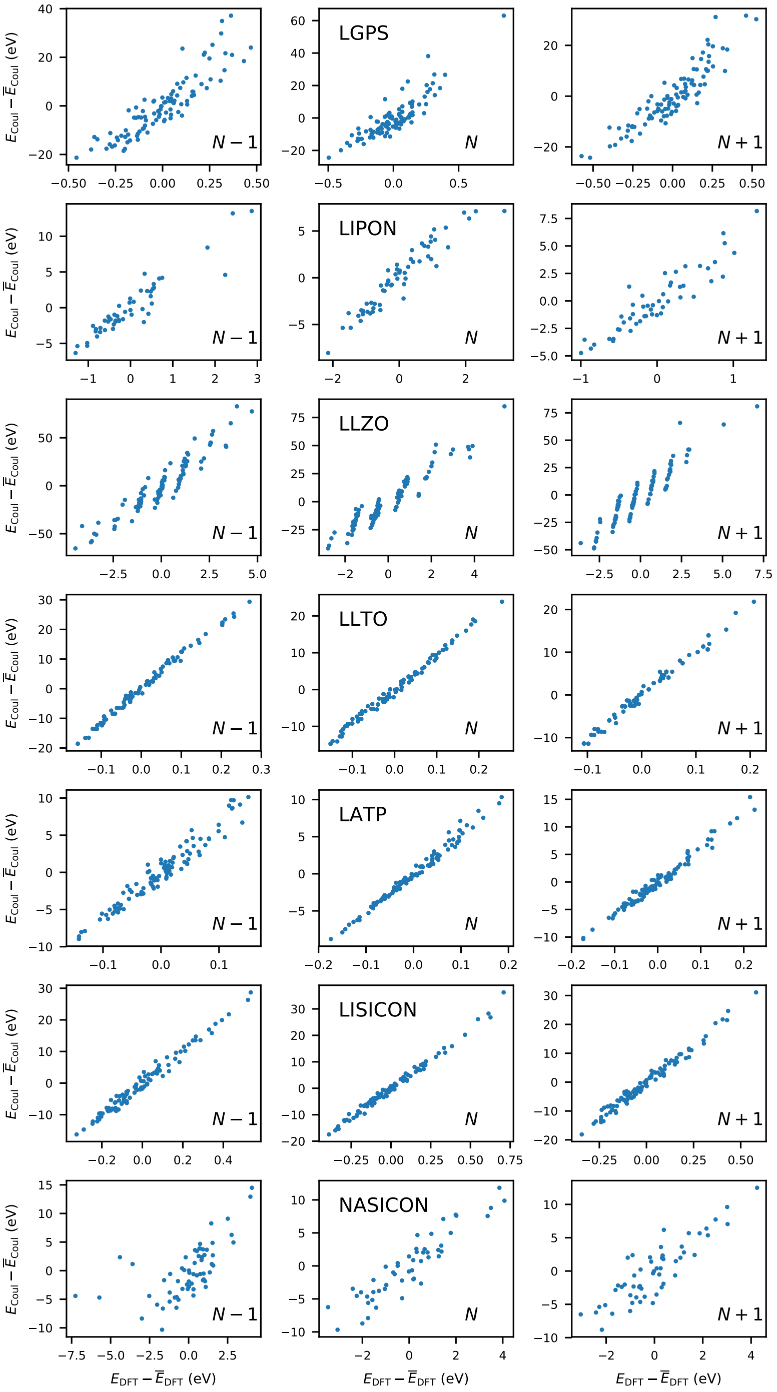

Figure A.2 – Ewald (Coulomb) energies vs. DFT energies for selected SSE materials.

Bibliography

[1] Christophe Pillot. The Rechargeable Battery Market and Main Trends 2016-2025, 2017.

[2] Koichi Momma, Fujio Izumi, and IUCr. VESTA 3 for three-dimensional visualization of crystal, volumetric and morphology data. *J. Appl. Crystallogr.*, 44(6):1272–1276, dec 2011.

[3] Ming Xu, Min Sik Park, Jae Myung Lee, Tae Young Kim, Young Sin Park, and Evan Ma. Mechanisms of Li + transport in garnet-type cubic Li 3 + x La 3 M 2 O 12 (M = Te, Nb, Zr). *Phys. Rev. B*, 85(5):052301, feb 2012.

[4] Michael M. Thackeray, Christopher Wolverton, and Eric D. Isaacs. Electrical energy storage for transportation—approaching the limits of, and going beyond, lithium-ion batteries. *Energy Environ. Sci.*, 5(7):7854, jun 2012.

[5] Erik J. Berg, Claire Villevieille, Daniel Streich, Sigita Trabesinger, and Petr Novák. Rechargeable Batteries: Grasping for the Limits of Chemistry. *J. Electrochem. Soc.*, 162(14):A2468–A2475, jan 2015.

[6] M. Stanley Whittingham. Ultimate Limits to Intercalation Reactions for Lithium Batteries. *Chem. Rev.*, 114(23):11414–11443, dec 2014.

[7] Gilbert N. Lewis and Frederick G. Keyes. THE POTENTIAL OF THE LITHIUM ELECTRODE. *J. Am. Chem. Soc.*, 35(4):340–344, apr 1913.

[8] William Sidney Harris. ELECTROCHEMICAL STUDIES IN CYCLIC ESTERS. Technical report, Lawrence Livermore National Laboratory (LLNL), Livermore, CA (United States), jul 1958.

[9] M. B. Armand, M. S. Whittingham, and R. A. Huggins. The iron cyanide bronzes. *Mater. Res. Bull.*, 7(2):101–107, feb 1972.

[10] D. Fouchard and L. Lechner. Analysis of safety and reliability in secondary lithium batteries. *Electrochim. Acta*, 38(9):1193–1198, jun 1993.

[11] K. Brandt. Historical development of secondary lithium batteries. *Solid State Ionics*, 69(3-4):173–183, aug 1994.

[12] Yuyan Shao, Fei Ding, Jie Xiao, Jian Zhang, Wu Xu, Sehkyu Park, Ji-Guang Zhang, Yong Wang, and Jun Liu. Making Li-Air Batteries Rechargeable: Material Challenges. *Adv. Funct. Mater.*, 23(8):987–1004, feb 2013.

[13] Sheng S. Zhang. Liquid electrolyte lithium/sulfur battery: Fundamental chemistry, problems, and solutions. *J. Power Sources*, 231:153–162, jun 2013.

[14] Arumugam Manthiram, Yongzhu Fu, Sheng-Heng Chung, Chenxi Zu, and Yu-Sheng Su. Rechargeable Lithium–Sulfur Batteries. *Chem. Rev.*, 114(23):11751–11787, dec 2014.

[15] Lin Chen and Leon L. Shaw. Recent advances in lithium–sulfur batteries. *J. Power Sources*, 267:770–783, dec 2014.

[16] Markus Hagen, Dominik Hanselmann, Katharina Ahlbrecht, Rudi Maça, Daniel Gerber, and Jens Tübke. Lithium-Sulfur Cells: The Gap between the State-of-the-Art and the Requirements for High Energy Battery Cells. *Adv. Energy Mater.*, 5(16):1401986, aug 2015.

[17] Lorenzo Grande, Elie Paillard, Jusef Hassoun, Jin-Bum Park, Yung-Jung Lee, Yang-Kook Sun, Stefano Passerini, and Bruno Scrosati. The Lithium/Air Battery: Still an Emerging System or a Practical Reality? *Adv. Mater.*, 27(5):784–800, feb 2015.

[18] Eliana Quartarone and Piercarlo Mustarelli. Electrolytes for solid-state lithium rechargeable batteries: recent advances and perspectives. *Chem. Soc. Rev.*, 40(5):2525, apr 2011.

[19] Michel Armand. Polymer solid electrolytes - an overview. *Solid State Ionics*, 9-10:745–754, dec 1983.

[20] João C. Barbosa, José P. Dias, Senentxu Lanceros-Méndez, and Carlos M. Costa. Recent advances in poly(Vinylidene fluoride) and its copolymers for lithium-ion battery separators, jul 2018.

[21] Kurt Lehovec. Solid state battery, jul 1954.

[22] Joseph L Weininger. Solid electrolyte cell, aug 1961.

[23] Kurt Lehovec and Donald M Smyth. Solid barrier electrolyte incorporating additive, apr 1962.

[24] Harry C Lieb and John A De Rosa. Solid-state battery, oct 1963.

[25] H.Y-P. Hong. Crystal structures and crystal chemistry in the system Na1+xZr2SixP3-xO12. *Mater. Res. Bull.*, 11(2):173–182, feb 1976.

[26] J.B. Goodenough, H.Y-P. Hong, and J.A. Kafalas. Fast Na+-ion transport in skeleton structures. *Mater. Res. Bull.*, 11(2):203–220, feb 1976.

[27] Xiaoxiong Xu, Zhaoyin Wen, Xuelin Yang, Jingchao Zhang, and Zhonghua Gu. High lithium ion conductivity glass-ceramics in Li2O-Al2O3-TiO2-P2O5from nanoscaled glassy powders by mechanical milling. *Solid State Ionics*, 177(26-32 SPEC. ISS.):2611–2615, oct 2006.

[28] B. Kumar, D. Thomas, and J. Kumar. Space-Charge-Mediated Superionic Transport in Lithium Ion Conducting Glass–Ceramics. *J. Electrochem. Soc.*, 156(7):A506, jul 2009.

[29] H.Y-P. Y P Hong. Crystal structure and ionic conductivity of Li14Zn(GeO4)4 and other new Li+ superionic conductors. *Mater. Res. Bull.*, 13(2):117–124, feb 1978.

[30] Ryoji Kanno, Takayuki Hata, Yoji Kawamoto, and Michihiko Irie. Synthesis of a new lithium ionic conductor, thio-LISICON–lithium germanium sulfide system. *Solid State Ionics*, 130(1-2):97–104, may 2000.

[31] Ryoji Kanno and Masahiro Murayama. Lithium Ionic Conductor Thio-LISICON: The Li[sub 2]S-GeS[sub 2]-P[sub 2]S[sub 5] System. *J. Electrochem. Soc.*, 148(7):A742, jul 2001.

[32] Yuki Kato, Satoshi Hori, Toshiya Saito, Kota Suzuki, Masaaki Hirayama, Akio Mitsui, Masao Yonemura, Hideki Iba, and Ryoji Kanno. High-power all-solid-state batteries using sulfide superionic conductors. *Nat. Energy*, 1(4):16030, mar 2016.

[33] T Takahashi and H Iwahara. Ionic conduction in perovskite-type oxide solid solution and its application to the solid electrolyte fuel cell. *Energy Convers.*, 11(3):105–111, sep 1971.

[34] Yoshiyuki Inaguma, Chen Liquan, Mitsuru Itoh, Tetsurō Nakamura, Takashi Uchida, Hiromasa Ikuta, and Masataka Wakihara. High ionic conductivity in lithium lanthanum titanate. *Solid State Commun.*, 86(10):689–693, jun 1993.

[35] R. Scholder. Über Orthosalze und maximale Sauerstoff-Koordination. *Angew. Chemie*, 70(19):583–594, oct 1958.

[36] C. Delmas, A. Maazaz, F. Guillen, C. Fouassier, J.M. Réau, and P. Hagenmuller. Des conducteurs ioniques pseudo-bidimensionnels: Li8MO6 (M = Zr, Sn), Li7LO6 (L = Nb, Ta) et Li6In2O6. *Mater. Res. Bull.*, 14(5):619–625, may 1979.

[37] Claus Mühle, Robert E. Dinnebier, Leo van Wüllen, Georg Schwering, and Jansen* Martin. New Insights into the Structural and Dynamical Features of Lithium Hexaoxometalates Li7MO6 (M = Nb, Ta, Sb, Bi). 2004.

[38] F. Abbattista, M. Vallino, and D. Mazza. Remarks on the binary systems Li2O-Me2O5 (Me=Nb, Ta). *Mater. Res. Bull.*, 22(8):1019–1027, aug 1987.

[39] H. Hyooma and K. Hayashi. Crystal structures of La3Li5M2O12 (M=Nb, Ta). *Mater. Res. Bull.*, 23(10):1399–1407, oct 1988.

[40] D. Mazza. Remarks on a ternary phase in the La2O3-Me2O5-Li2O system (Me=Nb, Ta). *Mater. Lett.*, 7(5-6):205–207, nov 1988.

[41] Venkataraman Thangadurai, Heiko Kaack, and Werner J. F. Weppner. Novel Fast Lithium Ion Conduction in Garnet-Type Li5La3M2O12 (M= Nb, Ta). *J. Am. Ceram. Soc.*, 86(3):437–440, mar 2003.

[42] Ramaswamy Murugan, Venkataraman Thangadurai, and Werner Weppner. Fast Lithium Ion Conduction in Garnet-Type Li7La3Zr2O12. *Ang. Chem. Int. Ed.*, 46(41):7778–7781, oct 2007.

[43] Junji Awaka, Norihito Kijima, Hiroshi Hayakawa, and Junji Akimoto. Synthesis and structure analysis of tetragonal Li7La3Zr2O12 with the garnet-related type structure. *J. Solid State Chem.*, 182(8):2046–2052, aug 2009.

[44] Charles A. Geiger, Evgeny Alekseev, Biljana Lazic, Martin Fisch, Thomas Armbruster, Ramona Langner, Michael Fechtelkord, Namjun Kim, Thomas Pettke, and Werner Weppner. Crystal Chemistry and Stability of "Li 7 La 3 Zr 2 O 12 " Garnet: A Fast Lithium-Ion Conductor. *Inorg. Chem.*, 50(3):1089–1097, feb 2011.

[45] A. Rahman. Particle motions in superionic conductors. *J. Chem. Phys.*, 65(11):4845–4848, dec 1976.

[46] Yung Sik Kim and Roy G. Gordon. Ion-ion interaction potentials and their application to the theory of alkali halide and alkaline earth dihalide molecules. *J. Chem. Phys.*, 60(11):4332–4344, jun 1974.

[47] M Dixon and M J Gillan. Computer simulation of superionic CaF 2. *J. Phys. C Solid State Phys.*, 11(5):L165–L169, mar 1978.

[48] M. Dixon and M. J. Gillan. Computer simulation of fast ion transport in fluorites. *Le J. Phys. Colloq.*, 41(C6):C6–24–C6–27, jul 1980.

[49] M J Gillan and M Dixon. Molecular dynamics simulation of fast-ion conduction in SrCl 2 . I. Self-diffusion. *J. Phys. C Solid State Phys.*, 13(10):1901–1917, apr 1980.

[50] Yasuaki Hiwatari and Akira Ueda. Monte Carlo Study of the Soft-Core Model for α-AgI. *J. Phys. Soc. Japan*, 48(3):766–772, mar 1980.

[51] Atsuo Fukumoto, Akira Ueda, and Yasuaki Hiwatari. Molecular Dynamics Studies of Superionic Conductors. Interionic Potential and Ion-Conducting Phase. *J. Phys. Soc. Japan*, 51(12):3966–3973, dec 1982.

[52] M.J. Gillan. The simulation of superionic materials. *Phys. B+C*, 131(1-3):157–174, aug 1985.

[53] J. R. Walker and C. R. A. Catlow. Defect structure and ionic conductivity in lithium nitride. *Philos. Mag. A*, 43(2):265–272, feb 1981.

[54] C. R. A. Catlow, R. James, W. C. Mackrodt, and R. F. Stewart. Defect energetics in α-Al2O3 and rutile TiO2. *Phys. Rev. B*, 25(2):1006–1026, jan 1982.

[55] M.L. Wolf, J.R. Walker, and C.R.A. Catlow. Structural and transport properties of β"-Al2O3. *Solid State Ionics*, 13(1):33–38, apr 1984.

[56] C. Lane, G.C. Farrington, J.O. Thomas, and M.A. Zendejas. Molecular dynamics simulation of ion transport in Na+-Ba2+-β"-alumina. *Solid State Ionics*, 40-41:53–58, aug 1990.

[57] Osamu Ito, Masaaki Mukaide, and Masanori Yoshikawa. Molecular dynamics analysis of impurity ions behavior in β"-Al2O3. *Solid State Ionics*, 80(3-4):181–187, sep 1995.

[58] Brandon C. Wood and Nicola Marzari. Dynamical Structure, Bonding, and Thermodynamics of the Superionic Sublattice in α-AgI. *Phys. Rev. Lett.*, 97(16):166401, oct 2006.

[59] N Bernstein, M D Johannes, and Khang Hoang. Origin of the structural phase transition in Li7La3Zr2O12. *Phys. Rev. Lett.*, 109(20):205702, nov 2012.

[60] Randy Jalem, Yoshihiro Yamamoto, Hiromasa Shiiba, Masanobu Nakayama, Hirokazu Munakata, Toshihiro Kasuga, and Kiyoshi Kanamura. Concerted Migration Mechanism in the Li Ion Dynamics of Garnet-Type Li 7 La 3 Zr 2 O 12. *Chem. Mater.*, 25(3):425–430, feb 2013.

[61] Lincoln J Miara, Shyue Ping Ong, Yifei Mo, William Davidson Richards, Youngsin Park, Jae-Myung Lee, Hyo Sug Lee, and Gerbrand Ceder. Effect of Rb and Ta Doping on the Ionic Conductivity and Stability of the Garnet Li 7+2 x – y (La 3– x Rb x)(Zr 2– y Ta y)O 12 (0<x<0.375, 0<y<1) Superionic Conductor: A First Principles Investigation. *Chem. Mater.*, 25(15):3048–3055, aug 2013.

[62] Katharina Meier, Teodoro Laino, and Alessandro Curioni. Solid-State Electrolytes: Revealing the Mechanisms of Li-Ion Conduction in Tetragonal and Cubic LLZO by First-Principles Calculations. *J. Phys. Chem. C*, 118(13):6668–6679, apr 2014.

[63] Daniel Rettenwander, Peter Blaha, Robert Laskowski, Karlheinz Schwarz, Patrick Bottke, Martin Wilkening, Charles A. Geiger, and Georg Amthauer. DFT Study of the Role of Al 3+ in the Fast Ion-Conductor Li 7–3 x Al 3+ x La 3 Zr 2 O 12 Garnet. *Chem. Mater.*, 26(8):2617–2623, apr 2014.

[64] Yutao Li, Jian-Tao Han, Chang-An Wang, Sven C. Vogel, Hui Xie, Maowen Xu, and John B. Goodenough. Ionic distribution and conductivity in lithium garnet Li7La3Zr2O12. *J. Power Sources*, 209:278–281, jul 2012.

[65] Daniel Rettenwander, Günther Redhammer, Florian Preishuber-Pflügl, Lei Cheng, Lincoln Miara, Reinhard Wagner, Andreas Welzl, Emmanuelle Suard, Marca M. Doeff, Martin Wilkening, Jürgen Fleig, and Georg Amthauer. Structural and Electrochemical

Consequences of Al and Ga Cosubstitution in Li 7 La 3 Zr 2 O 12 Solid Electrolytes. *Chem. Mater.*, 28(7):2384–2392, apr 2016.

[66] Saikat Mukhopadhyay, Travis Thompson, Jeff Sakamoto, Ashfia Huq, Jeff Wolfenstine, Jan L. Allen, Noam Bernstein, Derek A. Stewart, and M. D. Johannes. Structure and Stoichiometry in Supervalent Doped Li 7 La 3 Zr 2 O 12. *Chem. Mater.*, 27(10):3658–3665, may 2015.

[67] Matthew J. Klenk and Wei Lai. Effect of exchange-correlation functionals on the density functional theory simulation of phase transformation of fast-ion conductors: A case study in the Li garnet oxide Li7La3Zr2O12. *Comput. Mater. Sci.*, 134:132–136, jun 2017.

[68] Stefan Adams and Rayavarapu Prasada Rao. Ion transport and phase transition in Li 7-xLa 3(Zr 2-xM x)O 12 (M = Ta 5+, Nb 5+, x = 0, 0.25). *J. Mater. Chem.*, 22(4):1426–1434, dec 2012.

[69] G. Larraz, A. Orera, M. L. Sanjuán, H. Hayakawa, K. I. Ohshima, J. Akimoto, M. L. Saboungi, N. Kim, T. Pettke, W. Weppner, V. Duppel, L. Kienle, and J. Janek. Cubic phases of garnet-type Li7La3Zr2O12: the role of hydration. *J. Mater. Chem. A*, 1(37):11419, 2013.

[70] M. Matsui, K. Takahashi, K. Sakamoto, A. Hirano, Y. Takeda, O. Yamamoto, and N. Imanishi. Phase stability of a garnet-type lithium ion conductor Li 7 La 3 Zr 2 O 12. *Dalt. Trans.*, 43(3):1019–1024, dec 2014.

[71] Yuxing Wang, Ashfia Huq, and Wei Lai. Insight into lithium distribution in lithium-stuffed garnet oxides through neutron diffraction and atomistic simulation: Li7-xLa3Zr2-xTaxO12 (x=0–2) series. *Solid State Ionics*, 255:39–49, feb 2014.

[72] Michael P. O'Callaghan and Edmund J. Cussen. Lithium dimer formation in the Li-conducting garnets Li 5+x Ba x La 3-x Ta 2 O 12 (0 < x < 1.6). *Chem. Commun.*, 0(20):2048–2050, may 2007.

[73] Hui Xie, Jose A. Alonso, Yutao Li, Maria T. Fernandez-Diaz, and John B. Goodenough. Lithium Distribution in Aluminum-Free Cubic Li 7 La 3 Zr 2 O 12. *Chem. Mater.*, 23(16):3587–3589, aug 2011.

[74] Randy Jalem, M.J.D. J D Rushton, William Manalastas, Masanobu Nakayama, Toshihiro Kasuga, John A. Kilner, and Robin W. Grimes. Effects of gallium doping in garnet-type Li<inf>7</inf>La<inf>3</inf>Zr<inf>2</inf>O<inf>12</inf> solid electrolytes. *Chem. Mater.*, 27(8):2821–2831, apr 2015.

[75] Matthew Klenk and Wei Lai. Local structure and dynamics of lithium garnet ionic conductors: tetragonal and cubic Li 7 La 3 Zr 2 O 7. *Phys. Chem. Chem. Phys.*, 17(14):8758–8768, apr 2015.

[76] Matthew J. Klenk and Wei Lai. Finite-size effects on the molecular dynamics simulation of fast-ion conductors: A case study of lithium garnet oxide Li7La3Zr2O12. *Solid State Ionics*, 289, 2016.

[77] Mario Burbano, Dany Carlier, Florent Boucher, Benjamin J. Morgan, and Mathieu Salanne. Sparse Cyclic Excitations Explain the Low Ionic Conductivity of Stoichiometric Li 7 La 3 Zr 2 O 12. *Phys. Rev. Lett.*, 116(13):135901, mar 2016.

[78] Fei Chen, Junyang Li, Zhifeng Huang, Ying Yang, Qiang Shen, and Lianmeng Zhang. Origin of the Phase Transition in Lithium Garnets. *J. Phys. Chem. C*, 122(4):1963–1972, feb 2018.

[79] Giovanni Pizzi, Andrea Cepellotti, Riccardo Sabatini, Nicola Marzari, and Boris Kozinsky. AiiDA: automated interactive infrastructure and database for computational science. *Comput. Mater. Sci.*, 111:218–230, jan 2016.

[80] Hans C. Andersen. Molecular dynamics simulations at constant pressure and/or temperature. *J. Chem. Phys.*, 72(4):2384–2393, feb 1980.

[81] Shuichi Nosé. A unified formulation of the constant temperature molecular dynamics methods. *J. Chem. Phys.*, 81(1):511–519, jul 1984.

[82] William G. Hoover. Canonical dynamics: Equilibrium phase-space distributions. *Phys. Rev. A*, 31(3):1695–1697, mar 1985.

[83] Glenn J. Martyna, Michael L. Klein, and Mark Tuckerman. Nosé–Hoover chains: The canonical ensemble via continuous dynamics. *J. Chem. Phys.*, 97(4):2635–2643, aug 1992.

[84] H. J. C. Berendsen, J. P. M. Postma, W. F. van Gunsteren, A. DiNola, and J. R. Haak. Molecular dynamics with coupling to an external bath. *J. Chem. Phys.*, 81(8):3684–3690, oct 1984.

[85] Giovanni Bussi, Davide Donadio, and Michele Parrinello. Canonical sampling through velocity rescaling. *J. Chem. Phys.*, 126(1):014101, jan 2007.

[86] Michele Ceriotti, Giovanni Bussi, and Michele Parrinello. Langevin Equation with Colored Noise for Constant-Temperature Molecular Dynamics Simulations. *Phys. Rev. Lett.*, 102(2):020601, jan 2009.

[87] Michele Ceriotti, Giovanni Bussi, and Michele Parrinello. Colored-Noise Thermostats à la Carte. *J. Chem. Theory Comput.*, 6(4):1170–1180, apr 2010.

[88] E. Schrödinger. An Undulatory Theory of the Mechanics of Atoms and Molecules. *Phys. Rev.*, 28(6):1049–1070, dec 1926.

[89] R. Car and M. Parrinello. Unified Approach for Molecular Dynamics and Density-Functional Theory. *Phys. Rev. Lett.*, 55(22):2471–2474, nov 1985.

[90] Jürg Hutter, Hans Peter Lüthi, and Michele Parrinello. Electronic structure optimization in plane-wave-based density functional calculations by direct inversion in the iterative subspace. *Comput. Mater. Sci.*, 2(2):244–248, mar 1994.

[91] B. J. Alder and T. E. Wainwright. Phase Transition for a Hard Sphere System. *J. Chem. Phys.*, 27(5):1208, aug 1957.

[92] J. E. Jones. On the Determination of Molecular Fields. II. From the Equation of State of a Gas. *Proc. R. Soc. A Math. Phys. Eng. Sci.*, 106(738):463–477, oct 1924.

[93] R. A. Buckingham. The Classical Equation of State of Gaseous Helium, Neon and Argon. *Proc. R. Soc. A Math. Phys. Eng. Sci.*, 168(933):264–283, oct 1938.

[94] B. G. Dick and A. W. Overhauser. Theory of the Dielectric Constants of Alkali Halide Crystals. *Phys. Rev.*, 112(1):90–103, oct 1958.

[95] R. A. McKee. A generalization of the nernst-Einstein equation for self-diffusion in high defect concentration solids. *Solid State Ionics*, 5(C):133–136, 1981.

[96] Yiqiu Li, Zheng Wang, Yang Cao, Fuming Du, Cheng Chen, Zhonghui Cui, and Xiangxin Guo. 24,W-Doped Li7La3Zr2O12 Ceramic Electrolytes for Solid State Li-ion Batteries. *Electrochim. Acta*, 180, 2015.

[97] Matthieu Mottet, Aris Marcolongo, Teodoro Laino, and Ivano Tavernelli. Doping in garnet-type electrolytes: Kinetic and thermodynamic effects from molecular dynamics simulations. *Phys. Rev. Mater.*, 3(3), mar 2019.

[98] S. Plimpton. Fast Parallel Algorithms for Short-Range Molecular Dynamics. *J. Comput. Phys.*, 117(1):1–19, 1995.

[99] Dominik Marx and Juerg Hutter. Ab-initio Molecular Dynamics: Theory and Implementation. In J Grotendorst, editor, *Mod. Methods Algorithms Quantum Chem.*, NIC, pages 301–449, Julich, 2000. Forschungszentrum Jülich.

[100] Wanda Andreoni and Alessandro Curioni. New Advances in Chemistry and Material Science with CPMD and Parallel Computing. *Parallel Comput.*, 26:819–842, 2000.

[101] S. Goedecker and M. Teter. Separable dual-space Gaussian pseudopotentials. *Phys. Rev. B - Condens. Matter Mater. Phys.*, 54(3):1703–1710, jul 1996.

[102] Reese E. Jones and Kranthi K. Mandadapu. Adaptive Green-Kubo estimates of transport coefficients from molecular dynamics based on robust error analysis. *J. Chem. Phys.*, 136(15):154102, apr 2012.

[103] S F Edwards and P W Anderson. Theory of spin glasses. *J. Phys. F Met. Phys.*, 5(5):965–974, may 1975.

[104] Babak Sadigh, Paul Erhart, Alexander Stukowski, Alfredo Caro, Enrique Martinez, and Luis Zepeda-Ruiz. Scalable parallel Monte Carlo algorithm for atomistic simulations of precipitation in alloys. *Phys. Rev. B - Condens. Matter Mater. Phys.*, 85(18):184203, 2012.

[105] M I Barker and T Gaskell. Velocity autocorrelation function and diffusion coefficient in a liquid. II. *J. Phys. C Solid State Phys.*, 5(4):353–365, feb 1972.

[106] Aris Marcolongo and Nicola Marzari. Ionic correlations and failure of Nernst-Einstein relation in solid-state electrolytes. *Phys. Rev. Mater.*, 1(2):025402, jul 2017.

[107] R Chitra and S Yashonath. Estimation of Error in the Diffusion-Coefficient from Molecular-Dynamics Simulations. *J. Phys. Chem. B*, 101(27):5437–5445, 1997.

[108] Xingfeng He, Yizhou Zhu, Alexander Epstein, and Yifei Mo. Statistical variances of diffusional properties from ab initio molecular dynamics simulations. *npj Comput. Mater.*, 4(1):18, dec 2018.

[109] J.L. L. Allen, Jeffrey Wolfenstine, Ezhiylmurugan Rangasamy, and Jeff Sakamoto. Effect of substitution (Ta, Al, Ga) on the conductivity of Li7La3Zr2O12. *J. Power Sources*, 206:315–319, may 2012.

[110] G. E. Murch. The Nernst-Einstein equation in high-defect-content solids. *Philos. Mag. A*, 45(4):685–692, apr 1982.

[111] Benjamin J. Morgan and Paul A. Madden. Relationships between Atomic Diffusion Mechanisms and Ensemble Transport Coefficients in Crystalline Polymorphs. *Phys. Rev. Lett.*, 112(14):145901, apr 2014.

[112] Xingfeng He, Yizhou Zhu, and Yifei Mo. Origin of fast ion diffusion in super-ionic conductors. *Nat. Commun.*, 8(May):15893, jun 2017.

[113] F. Caltagirone, G. Parisi, and T. Rizzo. Dynamical critical exponents for the mean-field Potts glass. *Phys. Rev. E - Stat. Nonlinear, Soft Matter Phys.*, 85(5):051504, may 2012.

[114] L. Dhivya, N. Janani, B. Palanivel, and Ramaswamy Murugan. Li+ transport properties of W substituted Li7La 3Zr2O12 cubic lithium garnets. *AIP Adv.*, 3(8), 2013.

[115] Yoshihiro Yamazaki, Frédéric Blanc, Yuji Okuyama, Lucienne Buannic, Juan C. Lucio-Vega, Clare P. Grey, and Sossina M. Haile. Proton trapping in yttrium-doped barium zirconate. *Nat. Mater.*, 12(7):647–651, jul 2013.

[116] Aline Fluri, Aris Marcolongo, Vladimir Roddatis, Alexander Wokaun, Daniele Pergolesi, Nicola Marzari, and Thomas Lippert. Enhanced Proton Conductivity in Y-Doped BaZrO3 via Strain Engineering, 2017.

[117] Norman L. Allinger. Conformational analysis. 130. MM2. A hydrocarbon force field utilizing V1 and V2 torsional terms. *J. Am. Chem. Soc.*, 99(25):8127–8134, dec 1977.

[118] Norman L. Allinger, Young H. Yuh, and Jenn Huei Lii. Molecular mechanics. The MM3 force field for hydrocarbons. 1. *J. Am. Chem. Soc.*, 111(23):8551–8566, nov 1989.

[119] F Ercolessi and J. B Adams. Interatomic Potentials from First-Principles Calculations: The Force-Matching Method. *Europhys. Lett.*, 26(8):583–588, jun 1994.

[120] Federico Zipoli and Alessandro Curioni. Reactive potential for the study of phase-change materials: GeTe. *New J. Phys.*, 15(12):123006, dec 2013.

[121] Julian D. Gale. GULP: A computer program for the symmetry-adapted simulation of solids. *J. Chem. Soc. Faraday Trans.*, 93(4):629–637, jan 1997.

[122] Julian D. Gale and Andrew L. Rohl. The General Utility Lattice Program (GULP). *Mol. Simul.*, 29(5):291–341, may 2003.

[123] Julian D. Gale. GULP: Capabilities and prospects. *Zeitschrift für Krist. - Cryst. Mater.*, 220(5/6):552–554, jan 2005.

[124] Steven G. Johnson. The NLopt nonlinear-optimization package.

[125] Francesco Biscani, Dario Izzo, Wenzel Jakob, Marcus Märtens, Alessio Mereta, Cord Kaldemeyer, Sergey Lyskov, Sylvain Corlay, Benjamin Pritchard, Kishan Manani, Johan Mabille, Tomasz Miąsko, Axel Huebl, Jakirkham, Hulucc, Polygon, Zihao Fu, The Gitter Badger, Merlin Nimier-David, Luka Čehovin Zajc, Jonas Adler, John Travers, Jeongseok Lee, Jakob Jordan, Ivan Smirnov, Huu Nguyen, Felipe Lema, Erik O'Leary, and Andrea Mambrini. esa/pagmo2: pagmo 2.10, jan 2019.

[126] Peter J. M. van Laarhoven and Emile H. L. Aarts. Simulated annealing. In *Simulated Annealing Theory Appl.*, pages 7–15. Springer Netherlands, Dordrecht, 1987.

[127] Rainer Storn and Kenneth Price. Differential Evolution - a simple and efficient adaptive scheme for global optimization over continuous spaces. International Computer Science Institute, Berkeley. Technical report, CA, 1995, Tech. Rep. TR-95–012, 1995.

[128] V. Feoktistov and S. Janaqi. Generalization of the strategies in differential evolution. In *18th Int. Parallel Distrib. Process. Symp. 2004. Proceedings.*, pages 165–170. IEEE.

[129] S. Paterlini and T. Krink. High performance clustering with differential evolution. In *Proc. 2004 Congr. Evol. Comput. (IEEE Cat. No.04TH8753)*, pages 2004–2011. IEEE.

[130] DERVİŞ KARABOĞA and SELÇUK ÖKDEM. *Elektrik : Turkish journal of electrical engineering & computer sciences.*, volume 12. Scientific and Technical Research Council of Turkey (TUBITAK) and Chamber of Electrical Engineers (EMO-TMMOB), jun 2004.

[131] Mahamed G. H. Omran, Ayed Salman, and Andries P. Engelbrecht. Self-adaptive Differential Evolution. pages 192–199. Springer, Berlin, Heidelberg, dec 2005.

[132] Johannes P. Dürholt, Guillaume Fraux, François-Xavier Coudert, and Rochus Schmid. Ab Initio Derived Force Fields for Zeolitic Imidazolate Frameworks: MOF-FF for ZIFs. *J. Chem. Theory Comput.*, 15(4):2420–2432, apr 2019.

[133] Lee-Ping Wang, Jiahao Chen, and Troy Van Voorhis. Systematic Parametrization of Polarizable Force Fields from Quantum Chemistry Data. *J. Chem. Theory Comput.*, 9(1):452–460, jan 2013.

[134] Francesco Fracchia, Gianluca Del Frate, Giordano Mancini, Walter Rocchia, and Vincenzo Barone. Force Field Parametrization of Metal Ions from Statistical Learning Techniques. *J. Chem. Theory Comput.*, 14(1):255–273, jan 2018.

[135] Omololu Akin-Ojo, Yang Song, and Feng Wang. Developing ab initio quality force fields from condensed phase quantum-mechanics/molecular-mechanics calculations through the adaptive force matching method. *J. Chem. Phys.*, 129(6):064108, aug 2008.

[136] Paolo Giannozzi, Stefano Baroni, Nicola Bonini, Matteo Calandra, Roberto Car, Carlo Cavazzoni, Davide Ceresoli, Guido L. Chiarotti, Matteo Cococcioni, Ismaila Dabo, Andrea Dal Corso, Stefano De Gironcoli, Stefano Fabris, Guido Fratesi, Ralph Gebauer, Uwe Gerstmann, Christos Gougoussis, Anton Kokalj, Michele Lazzeri, Layla Martin-Samos, Nicola Marzari, Francesco Mauri, Riccardo Mazzarello, Stefano Paolini, Alfredo Pasquarello, Lorenzo Paulatto, Carlo Sbraccia, Sandro Scandolo, Gabriele Sclauzero, Ari P. Seitsonen, Alexander Smogunov, Paolo Umari, and Renata M. Wentzcovitch. QUANTUM ESPRESSO: A modular and open-source software project for quantum simulations of materials. *J. Phys. Condens. Matter*, 2009.

[137] G. Wehrum and R. Hoppe. Zur Kenntnis 'Kationen-reicher' Tantalate Über Li7[TaO6]. *Zeitschrift für Anorg. und Allg. Chemie*, 620(4):659–664, apr 1994.

[138] Tobias Binninger, Aris Marcolongo, Matthieu Mottet, Valéry Weber, and Teodoro Laino. Comparison of computational methods for the electrochemical stability window of solid-state electrolyte materials. *J. Mater. Chem. A*, 2020.

[139] E. Peled. The electrochemical behavior of alkali and alkaline earth metals in nonaqueous battery systems—the solid electrolyte interphase model. *J. Electrochem. Soc.*, 126(12):2047–2051, 1979.

[140] E. Peled. Film forming reaction at the lithium/electrolyte interface. *Journal of Power Sources*, 9(3):253–266, 1983.

[141] Yizhou Zhu, Xingfeng He, and Yifei Mo. Origin of outstanding stability in the lithium solid electrolyte materials: Insights from thermodynamic analyses based on first-principles calculations. *ACS Applied Materials & Interfaces*, 7(42):23685–23693, 2015.

[142] Ziheng Lu and Francesco Ciucci. Metal borohydrides as electrolytes for solid-state li, na, mg, and ca batteries: A first-principles study. *Chemistry of Materials*, 29(21):9308–9319, 2017.

[143] William D. Richards, Lincoln J. Miara, Yan Wang, Jae Chul Kim, and Gerbrand Ceder. Interface stability in solid-state batteries. *Chemistry of Materials*, 28(1):266–273, 2016.

[144] Yutao Li, Weidong Zhou, Xi Chen, Xujie Lü, Zhiming Cui, Sen Xin, Leigang Xue, Quanxi Jia, and John B. Goodenough. Mastering the interface for advanced all-solid-state lithium rechargeable batteries. *Proceedings of the National Academy of Sciences*, 2016.

[145] R.D. Armstrong. The metal-solid electrolyte interphase. *Journal of Electroanalytical Chemistry and Interfacial Electrochemistry*, 52(3):413–419, 1974.

[146] John B. Goodenough and Youngsik Kim. Challenges for rechargeable li batteries. *Chemistry of Materials*, 22(3):587–603, 2010.

[147] Shyue Ping Ong, Oliviero Andreussi, Yabi Wu, Nicola Marzari, and Gerbrand Ceder. Electrochemical windows of room-temperature ionic liquids from molecular dynamics and density functional theory calculations. *Chemistry of Materials*, 23(11):2979–2986, 2011.

[148] Yifei Mo, Shyue Ping Ong, and Gerbrand Ceder. First principles study of the $Li_{10}GeP_2S_{12}$ lithium super ionic conductor material. *Chemistry of Materials*, 24(1):15–17, 2012.

[149] M. Nakayama, M. Kotobuki, H. Munakata, M. Nogami, and K. Kanamura. First-principles density functional calculation of electrochemical stability of fast li ion conducting garnet-type oxides. *Phys. Chem. Chem. Phys.*, 14:10008–10014, 2012.

[150] J. Bhattacharya and C. M. Wolverton. Influence of $Li_{10}GeP_2S_{12}$-type solid electrolyte on cell thermodynamics. *Carbon - Science and Technology*, 8:92–101, 2016.

[151] Y. Tian, T. Shi, W. D. Richards, J. Li, J. C. Kim, S.-H. Bo, and G. Ceder. Compatibility issues between electrodes and electrolytes in solid-state batteries. *Energy Environ. Sci.*, 10:1150–1166, 2017.

[152] Marcel Sadowski, Sabrina Sicolo, and Karsten Albe. Defect thermodynamics and interfacial instability of crystalline $li_4p_2s_6$. *Solid State Ionics*, 319:53–60, 2018.

[153] J. B. Clarke, J. W. Hastie, L. H. E. Kihlborg, R. Metselaar, and M. M. Thackeray. Definitions of terms relating to phase transitions of the solid state (iupac recommendations 1994). *Pure & Appl. Chem.*, 66:577–594, 1994.

[154] Shyue Ping Ong, Lei Wang, Byoungwoo Kang, and Gerbrand Ceder. $Li-Fe-P-O_2$ phase diagram from first principles calculations. *Chemistry of Materials*, 20(5):1798–1807, 2008.

[155] V. L. Chevrier, S. P. Ong, R. Armiento, M. K. Y. Chan, and G. Ceder. Hybrid density functional calculations of redox potentials and formation energies of transition metal compounds. *Phys. Rev. B*, 82:075122, 2010.

[156] M. Saubanère, M. B. Yahia, S. Lebègue, and M.-L. Doublet. An intuitive and efficient method for cell voltage prediction of lithium and sodium-ion batteries. *Nature Communications*, 5:5559, 2014.

[157] Alexander Urban, Dong-Hwa Seo, and Gerbrand Ceder. Computational understanding of li-ion batteries. *npj Computational Materials*, 2:16002, 2016.

[158] I. D. Raistrick, A. J. Mark, and R. A. Huggins. Thermodynamics and kinetics of the electrochemical insertion of lithium into tungsten bronzes. *Solid State Ionics*, 5:351 – 354, 1981.

[159] Joachim Maier. Mass transport in the presence of internal defect reactions—concept of conservative ensembles: I, chemical diffusion in pure compounds. *Journal of the American Ceramic Society*, 76(5):1212–1217, 1993.

[160] G. Pizzi, A. Cepellotti, R. Sabatini, N. Marzari, and B. Kozinsky. Aiida: automated interactive infrastructure and database for computational science. *Computational Materials Science*, 111:218 – 230, 2016.

[161] Shyue Ping Ong, William Davidson Richards, Anubhav Jain, Geoffroy Hautier, Michael Kocher, Shreyas Cholia, Dan Gunter, Vincent L. Chevrier, Kristin A. Persson, and Gerbrand Ceder. Python materials genomics (pymatgen): A robust, open-source python library for materials analysis. *Computational Materials Science*, 68:314 – 319, 2013.

[162] Zrl-aiida-toolbox. https://github.com/zrl-aiida-toolbox/zrl-aiida-toolbox.

[163] Paolo Giannozzi, Stefano Baroni, Nicola Bonini, Matteo Calandra, Roberto Car, Carlo Cavazzoni, Davide Ceresoli, Guido L Chiarotti, Matteo Cococcioni, Ismaila Dabo, Andrea Dal Corso, Stefano de Gironcoli, Stefano Fabris, Guido Fratesi, Ralph Gebauer, Uwe Gerstmann, Christos Gougoussis, Anton Kokalj, Michele Lazzeri, Layla Martin-Samos, Nicola Marzari, Francesco Mauri, Riccardo Mazzarello, Stefano Paolini, Alfredo Pasquarello, Lorenzo Paulatto, Carlo Sbraccia, Sandro Scandolo, Gabriele Sclauzero, Ari P Seitsonen, Alexander Smogunov, Paolo Umari, and Renata M Wentzcovitch. Quantum espresso: a modular and open-source software project for quantum simulations of materials. *Journal of Physics: Condensed Matter*, 21:395502, 2009.

[164] John P. Perdew, Kieron Burke, and Matthias Ernzerhof. Generalized gradient approximation made simple. *Phys. Rev. Lett.*, 77:3865–3868, Oct 1996.

[165] Gianluca Prandini, Antimo Marrazzo, Ivano E. Castelli, Nicolas Mounet, and Nicola Marzari. Precision and efficiency in solid-state pseudopotential calculations. *npj Computational Materials*, 4:72, 2018.

[166] Kurt Lejaeghere, Gustav Bihlmayer, Torbjörn Björkman, Peter Blaha, Stefan Blügel, Volker Blum, Damien Caliste, Ivano E. Castelli, Stewart J. Clark, Andrea Dal Corso, Stefano de Gironcoli, Thierry Deutsch, John Kay Dewhurst, Igor Di Marco, Claudia Draxl, Marcin Dułak, Olle Eriksson, José A. Flores-Livas, Kevin F. Garrity, Luigi Genovese, Paolo Giannozzi, Matteo Giantomassi, Stefan Goedecker, Xavier Gonze, Oscar Grånäs, E. K. U. Gross, Andris Gulans, François Gygi, D. R. Hamann, Phil J. Hasnip, N. A. W. Holzwarth, Diana Iuşan, Dominik B. Jochym, François Jollet, Daniel Jones,

Georg Kresse, Klaus Koepernik, Emine Küçükbenli, Yaroslav O. Kvashnin, Inka L. M. Locht, Sven Lubeck, Martijn Marsman, Nicola Marzari, Ulrike Nitzsche, Lars Nordström, Taisuke Ozaki, Lorenzo Paulatto, Chris J. Pickard, Ward Poelmans, Matt I. J. Probert, Keith Refson, Manuel Richter, Gian-Marco Rignanese, Santanu Saha, Matthias Scheffler, Martin Schlipf, Karlheinz Schwarz, Sangeeta Sharma, Francesca Tavazza, Patrik Thunström, Alexandre Tkatchenko, Marc Torrent, David Vanderbilt, Michiel J. van Setten, Veronique Van Speybroeck, John M. Wills, Jonathan R. Yates, Guo-Xu Zhang, and Stefaan Cottenier. Reproducibility in density functional theory calculations of solids. *Science*, 351(6280), 2016.

[167] Nicola Marzari, David Vanderbilt, Alessandro De Vita, and M. C. Payne. Thermal contraction and disordering of the al(110) surface. *Phys. Rev. Lett.*, 82:3296–3299, Apr 1999.

[168] Jochen Heyd, Gustavo E. Scuseria, and Matthias Ernzerhof. Erratum: “hybrid functionals based on a screened coulomb potential” [j. chem. phys. 118, 8207 (2003)]. *The Journal of Chemical Physics*, 124(21):219906, 2006.

[169] D. R. Hamann. Optimized norm-conserving vanderbilt pseudopotentials. *Phys. Rev. B*, 88:085117, Aug 2013.

[170] Martin Schlipf and François Gygi. Optimization algorithm for the generation of oncv pseudopotentials. *Computer Physics Communications*, 196:36 – 44, 2015.

[171] John P. Perdew, Robert G. Parr, Mel Levy, and Jose L. Balduz. Density-functional theory for fractional particle number: Derivative discontinuities of the energy. *Phys. Rev. Lett.*, 49:1691–1694, 1982.

[172] John P. Perdew and Mel Levy. Physical content of the exact kohn-sham orbital energies: Band gaps and derivative discontinuities. *Phys. Rev. Lett.*, 51:1884–1887, 1983.

[173] L. J. Sham and M. Schlüter. Density-functional theory of the band gap. *Phys. Rev. B*, 32:3883–3889, 1985.

[174] Takao Tsuneda, Jong-Won Song, Satoshi Suzuki, and Kimihiko Hirao. On koopmans' theorem in density functional theory. *J. Chem. Phys.*, 133(17):174101, 2010.

[175] G. Bergerhoff, R. Hundt, R. Sievers, and I. D. Brown. The inorganic crystal structure data base. *J. Chem. Inf. Comput. Sci.*, 23(2):66–69, 1983.

[176] Alec Belsky, Mariette Hellenbrandt, Vicky Lynn Karen, and Peter Luksch. New developments in the inorganic crystal structure database (icsd): accessibility in support of materials research and design. *Acta Crystallographica Section B*, 58(3-1):364–369, 2002.

[177] Keerthi Senevirathne, Cynthia S. Day, Michael D. Gross, Abdessadek Lachgar, and N.A.W. Holzwarth. A new crystalline lipon electrolyte: Synthesis, properties, and electronic structure. *Solid State Ionics*, 233:95–101, 2013.

[178] Alexander Kuhn, Jürgen Köhler, and Bettina V. Lotsch. Single-crystal x-ray structure analysis of the superionic conductor $Li_{10}GeP_2S_{12}$. *Phys. Chem. Chem. Phys.*, 15:11620–11622, 2013.

[179] J. Awaka, A. Takashima, K. Kataoka, N. Kijima, Y. Idemoto, and J. Akimoto. Crystal structure of fast lithium-ion-conducting cubic $Li_7La_3Zr_2O_{12}$. *Chemistry Letters*, 40:60–62, 2011.

[180] J.L. Fourquet, H. Duroy, and M.P. Crosnier-Lopez. Structural and microstructural studies of the series $La_{2/3-x}Li_{3x1/3-2x}TiO_3$. *Journal of Solid State Chemistry*, 127(2):283 – 294, 1996.

[181] Dharmesh H. Kothari and D.K. Kanchan. Effect of doping of trivalent cations Ga^{3+}, Sc^{3+}, Y^{3+} in $Li_{1.3}Al_{0.3}Ti_{1.7}(PO_4)_3$ (latp) system on Li^+ ion conductivity. *Physica B: Condensed Matter*, 501:90 – 94, 2016.

[182] H.Y-P. Hong. Crystal structure and ionic conductivity of $Li_{14}Zn(GeO_4)_4$ and other new Li^+ superionic conductors. *Materials Research Bulletin*, 13(2):117 – 124, 1978.

[183] H.Y-P. Hong. Crystal structures and crystal chemistry in the system $Na_{1+x}Zr_2Si_xP_{3-x}O_{12}$. *Materials Research Bulletin*, 11(2):173 – 182, 1976.

[184] Nist chemistry webbook. https://webbook.nist.gov/. Accessed: 2019-06-05.

[185] Noriaki Kamaya, Kenji Homma, Yuichiro Yamakawa, Masaaki Hirayama, Ryoji Kanno, Masao Yonemura, Takashi Kamiyama, Yuki Kato, Shigenori Hama, Koji Kawamoto, and Akio Mitsui. A lithium superionic conductor. *Nature Materials*, 10:682–686, 2011.

[186] Fudong Han, Tao Gao, Yujie Zhu, Karen J. Gaskell, and Chunsheng Wang. A battery made from a single material. *Advanced Materials*, 27(23):3473–3483, 2015.

[187] Xiaohua Yu, J. B. Bates, G. E. Jellison Jr., and F. X. Hart. A stable thin-film lithium electrolyte: Lithium phosphorus oxynitride. *J. Electrochem. Soc.*, 144:524–532, 1997.

[188] W. C. West, J. F. Whitacre, and J. R. Lim. Chemical stability enhancement of lithium conducting solid electrolyte plates using sputtered lipon thin films. *Journal of Power Sources*, 126(1):134 – 138, 2004.

[189] André Schwöbel, René Hausbrand, and Wolfram Jaegermann. Interface reactions between lipon and lithium studied by in-situ x-ray photoemission. *Solid State Ionics*, 273:51 – 54, 2015.

[190] Ramaswamy Murugan, Venkataraman Thangadurai, and Werner Weppner. Fast lithium ion conduction in garnet-type $Li_7La_3Zr_2O_{12}$. *Angewandte Chemie International Edition*, 46(41):7778–7781, 2007.

[191] Masashi Kotobuki, Hirokazu Munakata, Kiyoshi Kanamura, Yosuke Sato, and Toshihiro Yoshida. Compatibility of $Li_7La_3Zr_2O_{12}$ solid electrolyte to all-solid-state battery using li metal anode. *J. Electrochem. Soc.*, 157:A1076–A1079, 2010.

[192] Shingo Ohta, Tetsuro Kobayashi, and Takahiko Asaoka. High lithium ionic conductivity in the garnet-type oxide $Li_{7-X}La_3(Zr_{2-X}, Nb_X)O_{12}$ (x=0–2). *Journal of Power Sources*, 196(6):3342 – 3345, 2011.

[193] Fudong Han, Yizhou Zhu, Xingfeng He, Yifei Mo, and Chunsheng Wang. Electrochemical stability of $Li_{10}GeP_2S_{12}$ and $Li_7La_3Zr_2O_{12}$ solid electrolytes. *Advanced Energy Materials*, 6(8):1501590, 2016.

[194] M. Klingler, W. F. Chu, and W. Weppner. Coulometric titration of substituted $Li_xLa_{(2-x)/3}TiO_3$. *Ionics*, 3(3):289–291, 1997.

[195] C. H. Chen and K. Amine. Ionic conductivity, lithium insertion and extraction of lanthanum lithium titanate. *Solid State Ionics*, 144(1):51 – 57, 2001.

[196] U. v. Alpen, M. F. Bell, W. Wichelhaus, K. Y. Cheung, and G. J. Dudley. Ionic conductivity of $Li_{14}Zn(GeO_4)_4$ (lisicon). *Electrochimica Acta*, 23(12):1395 – 1397, 1978.

[197] Philippe Knauth. Inorganic solid li ion conductors: An overview. *Solid State Ionics*, 180(14):911 – 916, 2009.

[198] U. Warhus, J. Maier, and A. Rabenau. Thermodynamics of nasicon ($Na_{1+x}Zr_2Si_xP_{3-x}O_{12}$). *Journal of Solid State Chemistry*, 72(1):113 – 125, 1988.

[199] Yoshinori Noguchi, Eiji Kobayashi, Larisa S. Plashnitsa, Shigeto Okada, and Jun-ichi Yamaki. Fabrication and performances of all solid-state symmetric sodium battery based on nasicon-related compounds. *Electrochimica Acta*, 101:59–65, 2013.

[200] Yao Lu, Jose A. Alonso, Qiang Yi, Liang Lu, Zhong Lin Wang, and Chunwen Sun. A high-performance monolithic solid-state sodium battery with Ca^{2+} doped $Na_3Zr_2Si_2PO_{12}$ electrolyte. *Advanced Energy Materials*, 9(28):1901205, 2019.

[201] John P. Perdew, Weitao Yang, Kieron Burke, Zenghui Yang, Eberhard K. U. Gross, Matthias Scheffler, Gustavo E. Scuseria, Thomas M. Henderson, Igor Ying Zhang, Adrienn Ruzsinszky, Haowei Peng, Jianwei Sun, Egor Trushin, and Andreas Görling. Understanding band gaps of solids in generalized kohn-sham theory. *Proceedings of the National Academy of Sciences*, 114(11):2801–2806, 2017.

Matthieu G. MOTTET

Swiss Citizen – Born on August 3rd 1988

☎ 0041 79 587 63 23

✉ matthieu.mottet@outlook.com

Education

06.2015 – Present	École Polytechnique Fédérale de Lausanne (EPFL) – PhD in Material Science
09.2012 – 09.2014	Eidgenössische Technische Hochschule (ETH) Zürich, Switzerland — MSc in Chemistry.
10.2010 – 06.2011	University of Bristol – BSc exchange student.
09.2008 – 07.2011	École Polytechnique Fédérale de Lausanne (EPFL) – BSc in Chemistry and Chemical Engineering.

Awards

2014	Silver Medal of the ETH Zurich for outstanding Master Thesis

Work Experience

09.2019 – Present	Software Engineer II at Cimpress Technology, Winterthur
06.2015 – 06.2019	PhD student at IBM Research, Zurich – *Modelling of solid state systems.*
12.2014 – 02.2015	Intern at IBM Research, Zurich – *Ab-initio molecular dynamics of solid state systems.*

Publications

2014	Matthieu Mottet, Pawel Tecmer, Katharina Boguslawski, Örs Legeza and Markus Reiher, *Dissecting carbon–carbon, carbon–phosphorus and silicon–silicon bonds using quantum entanglement*, ***Chem. Phys. Phys. Chem***., 2014, **16**, 8872-8880
2019	Matthieu Mottet, Aris Marcolongo, Teodoro Laino, and Ivano Tavernelli, *Doping in garnet-type electrolytes: kinetic and thermodynamic effects from molecular dynamics simulations*, ***Phys. Rev. Materials,*** 2019, **3**, 035403
2020	Tobias Binninger, Aris Marcolongo, Matthieu Mottet, Valéry Webera and Teodoro Laino, *Comparison of computational methods for the electrochemical stability window of solid-state electrolyte materials,* ***J. Mater. Chem. A****, 2020*

Academic Experience

05.2014 – 10.2014	Continuation of the Master Thesis research project in the group of Prof. Nicola Spaldin at ETH, Switzerland
10.2013 – 04.2014	Master Thesis in the group of Prof. Nicola Spaldin at ETH, Switzerland – *Calculation of the electronic structure of molecular graphene*
04.2013 – 08.2013	Semester Project in the group of Prof. Markus Reiher at ETH, Switzerland – *Dissecting carbon–carbon, carbon–phosphorus and silicon–silicon bonds using quantum entanglement*
02.2013 – 04.2013	Semester Project in the group of Prof. Peter Chen at ETH, Switzerland – *Synthesis of rhenium carbine complexes for metathesis reactions*
06.2013 – 09.2013	Research Project in the group of Prof. Clémence Corminboeuf at EPFL, Switzerland – *Parametrization of a force-field for polythiophenes stacks.*

Presentations

06.2017	Invited talk at the Fall meeting for the Material Research Society in Boston, USA – *Accelerating Material Discovery, A Cognitive Approach Based on Molecular Simulations and Large Scale Data Analytics*
07.2018	Symposium at the Platform for Advanced Scientific Computing 2018 conference in Basel, Switzerland – *Doping Solid-State Electrolytes: Classical Modelling and Insights*

Extracurricular Activities

07.2019	Head Mentor at the 51th International Chemistry Olympiads in Paris, France
10.2017 – Present	Board member of the Swiss Science Olympiads Association
07.2017	Mentor at the 49th International Chemistry Olympiads in Bangkok, Thailand
07.2015	Mentor at the 47th International Chemistry Olympiads in Baku, Azerbaidjan
09.2014 – Present	Board member of the Swiss Chemistry Olympiads
07.2012 – 04.2013	Military Service in the Swiss Army as Soldier

Languages

French	Native language
English	Excellent knowledge
German	Good knowledge

Skills

General	Linux operating system, Matlab, Mathematica, MS Office, Docker, git
Simulation	Molecular dynamics (Amber, CPMD, LAMMPS), Ab-initio computations (Gaussian, ADF, Molpro, VASP, CPMD)
Programming	Bash scripting, Python, Javascript/Typescript, C/C++, SQL and NoSQL databases, Web technologies (HTML, CSS, GraphQL, Angular, React, REST)